Search for Signatures of Extra Dimensions in the Diphoton Mass Spectrum with the CMS Detector

Thesis by

Yousi Ma

In Partial Fulfillment of the Requirements

for the Degree of

Doctor of Philosophy

California Institute of Technology

Pasadena, California

2012

(Defended 7 May 2012)

Acknowledgements

Thank you to Harvey Newman, my advisor, for being my model of a brilliant, meticulous scientist. Thank you for the passion you bring to your work every day of the week, and for mentoring me for all of these years.

Thank you to my parents, Yamin Ma and Ying Xue, for overcoming many obstacles to bring me to the US, and raise me here. It has been a much better match for my personality and sensitivities, and I am appreciative of the opportunity.

Thank you to Vladimir Litvin for helping me at the start of my time at Caltech, from our very first Higgs analysis and onward.

Thank you to Toyoko Orimoto for taking me under your wing since you first came to our group as a Milliken Fellow, and for our continued collaboration on many analyses.

Thank you to my group members at Caltech: Jan Veverka, Chris Rogan, Yong Yang, Vladlen Timciuc, Adi Bornheim, and Marat Gataullin, for our work together, discussions, and the times shared in the St. Genis house.

Thank you to my students, Josh, Katie, Vishnu, Upa, Jonathan, Jacqueline, and Nicole, for choosing me as your teacher, and rewarding my efforts with your hard work.

Abstract

A search for signatures of extra dimensions in the diphoton invariant-mass spectrum has been performed with the Compact Muon Solenoid detector at the Large Hadron Collider. No excess of events above the standard model expectation is observed using a data sample collected in proton-proton collisions at $\sqrt{s} = 7$ TeV corresponding to an integrated luminosity of 2.2 fb^{-1}. In the context of the Randall–Sundrum model, lower limits are set on the mass of the first graviton excitation in the range of 0.86–1.84 TeV, for values of the associated coupling parameter $\tilde{k}$ between 0.01 and 0.10. Additionally, in the context of the large-extra-dimensions model, lower limits are set on the effective Planck scale in the range of 2.3–3.8 TeV at the 95% confidence level. These are the most restrictive bounds to date.

Contents

List of Figures

List of Tables

Chapter 1

Introduction

1.1 Introduction

The Standard Model (SM), which is the basis for most particle physics since the 1970s,[1] has withstood four decades of precision tests. However, it is not without limitations, such as the following:

- The number of generations of fermions is arbitrary
- The Higgs boson, the corresponding scalar of the mechanism for electroweak symmetry breaking, has not yet been found
- The gravitational force is not addressed
- The lack of candidates for dark matter
- The lack of an explanation for dark energy

In this dissertation, I will discuss an extension of the SM to include extra dimensions, which provide a theory for gravitation, as well as implications on electroweak symmetry breaking (EWSB).

[1] With the notable exception of neutrino masses and oscillations, for example.

	Leptons			quarks		
Generation	Flavor	Charge (e)	Mass (MeV)	Flavor	Charge (e)	Mass (MeV)
1	e	-1	0.511	u	$+2/3$	~ 3
	ν_e	0	$< 3 \times 10^{-6}$	d	$-1/3$	~ 5
2	μ	-1	105.7	c	$+2/3$	$\sim 1.2 \times 10^3$
	ν_μ	0	< 0.19	s	$-1/3$	~ 100
3	τ	-1	1777	t	$+2/3$	$\sim 178 \times 10^3$
	ν_τ	0	< 18.2	b	$-1/3$	$\sim 4.5 \times 10^3$

Table 1.1: Table of Fermions. Antipartners have the same properties except opposite charge [1]

1.2 Standard Model

The SM is a theory of elementary particles and their interactions under the electromagnetic, weak, and strong forces. In the SM, particles are divided in to two categories, fermions and bosons. Fermions have half-integer spin, compose the visible matter in the universe, and are further divided into leptons and quarks. Both leptons and quarks carry electromagnetic charge, while only the quarks carry color charge. The fermions are summarized in Table 1.1.

Bosons have integer spin, and mediate the interactions among the fermions. This is accomplished in the SM by introducting symmetry groups to represent each interaction. The electromagnetic force corresponds to $U(1)$ symmetry, the weak forces to $SU(2)$, and strong forces to $SU(3)$. Each such gauge group has a number of associated gauge bosons, 1 for $U(1)$, 3 for $SU(2)$, and 8 for $SU(3)$.

Taken independently, each of these gauge bosons should be massless, and indeed the 8 gluons of $SU(3)$ are. The massless generators of $SU(2)$, $W^i_\mu, i = 1, 2, 3$, and the single generator for $U(1)$, B_μ, are not what is observed in nature. Instead, there are 3 massive bosons ($W^\pm, Z$) for the weak force, and a single massless boson (γ) for the EM force (Table 1.2). This is achieved through the spontaneous symmetry breaking of the $SU(2) \bigotimes U(1)$ via the Higgs mechanism [2].

A simple example of spontaneous symmetry breaking is scalar ϕ^4 theory with an

Force	Gauge Boson	Charge	Spin	Mass (GeV)	Range
Strong	Gluon (g)	0	1	0	$10^{-15}m$
Electromagnetic	Photon (γ)	0	1	0	∞
Weak	$W^{\pm}$	± 1	1	80.4	10^{-18}
	Z^0	0	1	91.2	
Gravitational	Graviton (G)	0	2	?	∞

Table 1.2: Table of Bosons and forces. Graviton is not yet observed [1]

extra term in the potential:

$$L = \frac{1}{2}(\partial^{\mu}\phi)(\partial_{\mu}\phi) - \frac{1}{2}\mu\phi^2 - \frac{\lambda}{4}\phi^4. \tag{1.1}$$

Here the Lagrangian is symmetric under $\phi \rightarrow -\phi$, but the minimum of potential, $\phi_{min} = \pm\sqrt{\frac{-\mu^2}{\lambda}}$ is not.

This nonsymmetry of the ground state is called spontaneous symmetry breaking. In the case of electroweak symmetry breaking (EWSB), the Higgs scalar field plays this role, with the introduction of its potential leading to a nonzero vacuum expectation value, which breaks the $SU(2)\bigotimes U(1)$ to leave only $U(1)_{EM}$ symmetry. As a consequence, the 4 bosons of $SU(2)\bigotimes U(1)$ are reformulated into 3 massive bosons, and one massless boson, corresponding to the unbroken symmetry.

The unification of electromagnetic and weak theories was proposed by Glashow in 1961 [3], while the Higgs mechanism was incorporated into the SM by Weinberg and Salam in 1967 [4]. The renormalizability of gauge groups was demonstrated by 't Hooft in 1971 [5], and the QCD was completed with the discovery of assymptotic freedom by Gross, Wilczek, and Politzer in 1973 [6, 7].

1.3 QCD and Direct Photons

The LHC is a proton-proton collider, and the collision energy is so high that virtual partons form a significant fraction of all hard interactions. Protons are composed of valence quarks, uud, along with radiated gluons and quark-antiquark pairs (sea quarks). All of these constituents are called partons, and each parton carries a mo-

mentum fraction, x, of the total proton momentum with a probability given by the parton distribution function (PDF). A schematic for a generic hard interaction is given in Figure 1.1.

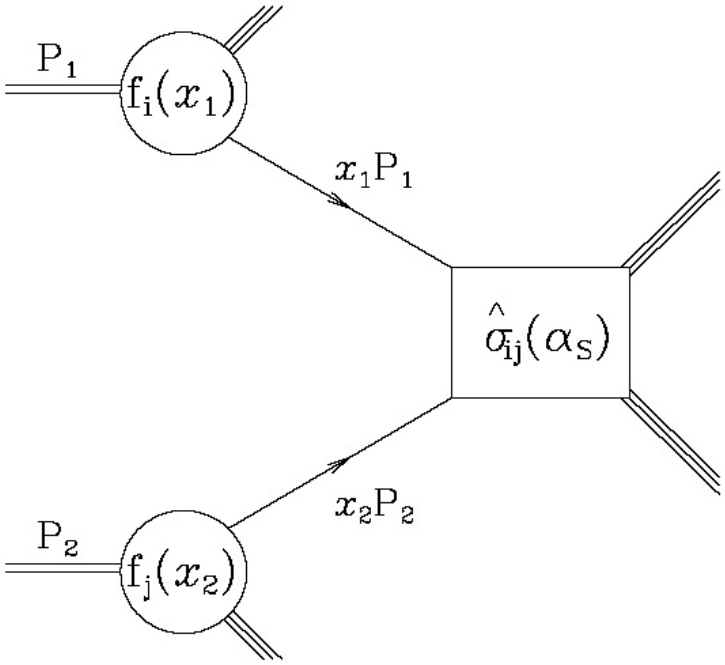

Figure 1.1: Hard interaction in proton proton collisions. [8]

In a hard scattering process, the cross section can be rewritten based on the factorization theorem of QCD:

$$\sigma(P_1, P_2) = \sum_{ij} \int dx_1 dx_2 f_i(x_1, \mu_F^2) f_j(x_2, \mu_F^2) \hat{\sigma_{ij}}(p_1, p_2, \alpha_s(\mu_R^2), Q^2/\mu_F^2), \qquad (1.2)$$

where P_1,P_2 are the four-momenta of the incoming hadrons, $p_1 = x_1 P_1$, $p_2 = x_2 P_2$ are the four-momenta of the partons participating in the hard interaction, $f_{i,j}$ are the parton distribution function (PDF) defined at a factorization scale μ_F, and $\hat{\sigma}$ is the short distance cross section for scattering of the two partons.

Direct production refers to photons that are produced in the parton-parton collision, as opposed to hadronization into neutral mesons (such as π_0) and subsequent decay to $\gamma\gamma$. Further discussion of these processes will be found in Section 6.1

1.4 Hierarchy Problem and Extra Dimensions

In addition to not yet being observed, the Higgs boson brings another problem into play, the so-called hierarchy problem. Because of its coupling to mass, the Higgs boson mass has corrections due to loops of massive particles (Figure 1.2). For example, the correction due to fermion loop is

$$\Delta M_H^2 = \frac{\lambda_f^2}{4\pi}(\Lambda^2 + M_H^2). \tag{1.3}$$

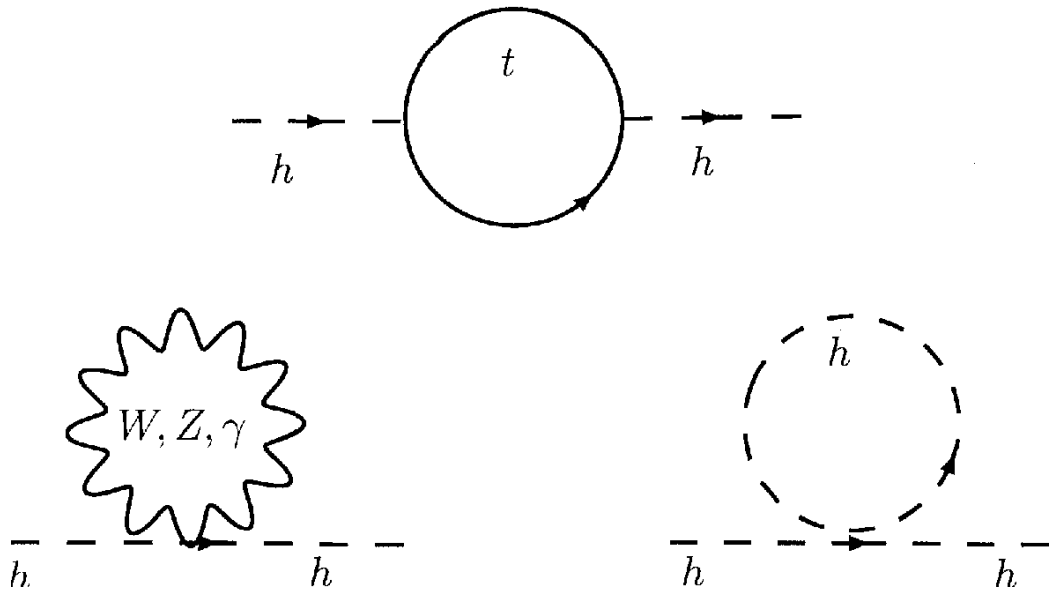

Figure 1.2: Virtual corrections to Higgs mass.

So that if we introduced a cutoff $\Lambda \sim M_{Pl} \sim 10^{19} GeV$, and $M_H \sim 100 GeV$, then the cancellations would need a precision of $\sim (M_H/\Lambda)^2 \sim 10^{-34}$. Since such precise cancellation of free parameters would seem to be very unsatisfactory for a unified theory, several extensions have been suggested. One class of extensions, supersymmetry [9], addresses the naturalness of the cancellations by introducing superpartner particles, which would give term-by-term cancellations of the virtual corrections due to each known particle with an opposite sign term from its superpartner. Another class of theories introduce additional spatial dimensions, which would then dilute the scale difference down to the same order of magnitude. Next, we will examine the details and implications of such extra-dimensional theories.

1.5 RS Theory and Phenomenology

One class of extensions to the SM addresses the hierarchy problem through the use of extra dimensions. Here we appeal to the multidimensional Gauss's law to explain the apparent weakness of gravity in the SM world. If gravitons are the only mediator that lives in the full higher-dimension space, then its fundamental scale is indeed the Planck scale, but is diluted to the EW scale levels when it is acting on the SM brane.

For instance, Arkani-Hamed, Dimopoulus, and Dvali (ADD) [10] proposed large extra dimensions to solve the hierarchy problem. Here, SM particles are constrained to the usual 3+1 dimensions of the SM "brane," while gravitons can propagate in all of the dimensions in the "bulk" [11]. If we assume the extra dimensions to be of a similar size, with radius R, then the multidimensional Gauss's Law gives

$$V(r) \sim \frac{m_1 m_2}{M_D^{n+2}} \frac{1}{r^{n+1}} (r << R), \tag{1.4}$$

and outside of the size of the extra dimensions, we have

$$V(r) \sim \frac{m_1 m_2}{M_D^{n+2} R^n} \frac{1}{r} (r >> R). \tag{1.5}$$

Thus we can identify the effective M_{pl} as

$$M_{pl}^2 = M_D^{n+2} R^n. \tag{1.6}$$

If we expect $M_D \sim 1TeV$, then we have a relation between the size and number of EDs:

$$R = 10^{\frac{30}{n_{ED}} - 19} m. \tag{1.7}$$

In a general sense, this extra dimensional dilution can be achieved with any number of additional dimensions of arbitrary size. However, we can already constrain the possibilities by interpreting results of other experiments. The case n = 1 is ruled out because the scale R would be of astrophysical size, while going beyond n = 6, 7 would take the scale R down to Planck or EW scales, and thus no longer "large"

extra dimensions. This leaves a typical search range of 2-7 EDs, for the ADD model.

However, in some sense we have just transformed the "large" hierarchy problem into a "small" hierarchy problem, where the size of the EDs span orders of magnitude. Randall and Sundrum [12] proposed an alternate solution with one extra dimension, where the metric between the 2 branes is not flat, but rather exponential (Figure 1.3), e.g.,

$$ds^2 = e^{-2kr_c y}\eta_{\mu\nu}dx^\mu dx^\nu - r_c^2 dy^2. \tag{1.8}$$

Such a metric preserves Poincare invariance in the usual four dimensions, and gives the following relation between M_{pl} and M_5, the 5D effective planck mass:

$$M_{pl}^2 = \frac{M_5^3}{k}(1 - e^{-2kr_c\pi}), \tag{1.9}$$

so that a reasonable $kr_c \sim 11-12$ yields the observed warp factor between the Planck and EW scales. It has been demonstrated [13] that such a value can be stabilized without fine tuning.

The curvature k is restricted to be small compared to M_5 so that the pertubative predictions can be trusted. Since M_5 is related to M_{pl}, this translates into a restriction on $k/M_{pl} \equiv \tilde{k} < 0.1$. Finally, string theoretic arguments give a natural size of the parameter of 10^{-2}, thus we search over the range $0.01 < \tilde{k} < 0.1$. (Figure 1.4)

1.5.1 Phenomenology

In order to escape detection from small-scale gravity experiments, it is necessary that the extra dimension(s) proposed be restricted to a very small volume and into a periodic coordinate. Such a prescription is referred to as compactification, and the extra compactified dimension leads to a Kaluza-Klein (KK) tower [15, 16], as the energy must be periodic over the size of the extra dimension. The masses of the KK

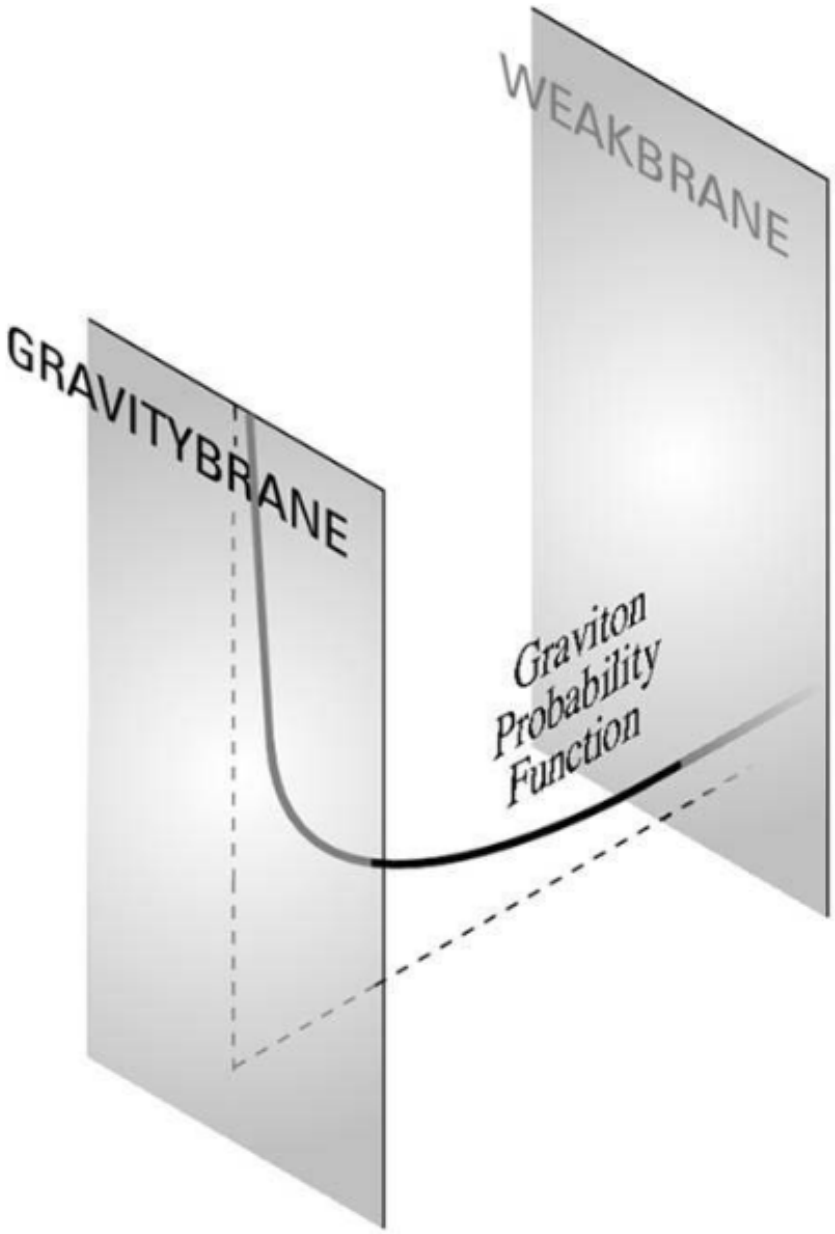

Figure 1.3: Exponential metric between Gravity and SM branes in the Randall-Sundrum model. Gravity propagates freely through the bulk, while known matter is constrained to the Infrared (IR) Brane.

tower obey the following relation:

$$m_n = kx_n e^{-kr_c\pi} \tag{1.10}$$

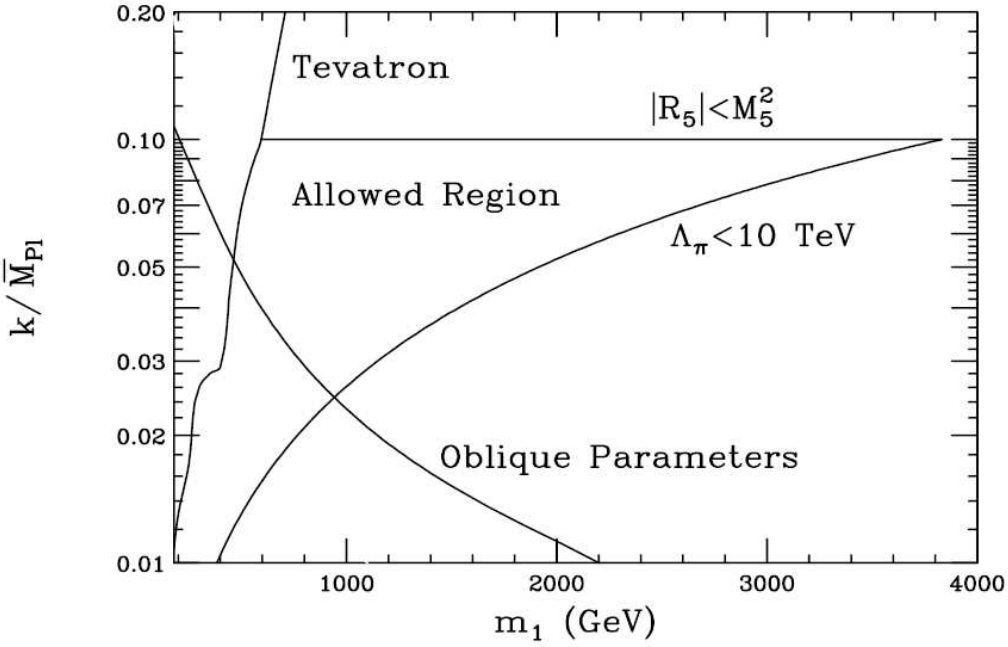

Figure 1.4: Summary of theoretical constraints on RS model [14]

where x_n is the nth root of the Bessel function J_1. The Bessel function arises due to the cylindrical symmetry from having a single periodic extra dimension alongside the usual dimensions of infinite linear extent. Note that the resonances are not equally spaced, but are related to the first excitation m_1. Thus for this search, we can parameterize the entire RS theory into M_1 and $\tilde{k}$, as in Figure 1.5.

Because of the universality of the graviton coupling, many decay modes are possible, including $\gamma\gamma$, e^+e^-, $\mu^+\mu^-$, $\tau^+\tau^-$, ZZ, W^+W^-, etc. The branching fractions are shown on Figure 1.6.

The e^+e^-, $\mu^+\mu^-$, and $\gamma\gamma$ modes have the cleanest signature, with lowest backgrounds, and between these the $\gamma\gamma$ mode has the benefit of a factor 2 in the branching ratio due to the sum over spin states.

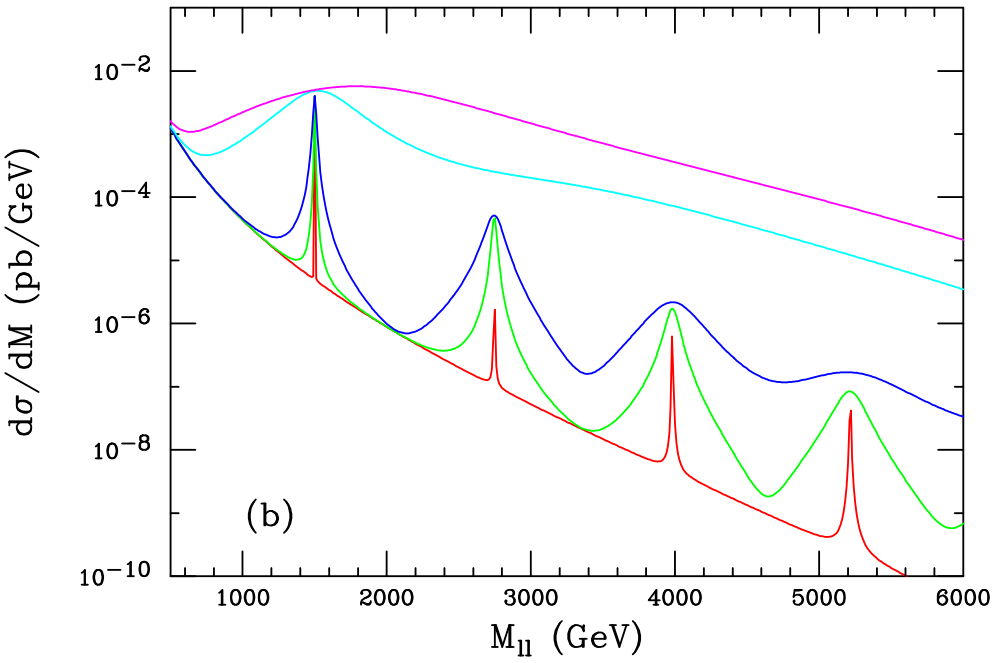

Figure 1.5: The mass distribution for a 1500 GeV graviton along with subsequent tower masses. $\tilde{k} = 1, 0.5, 0.1, 0.05, 0.01$ from top to bottom [17]

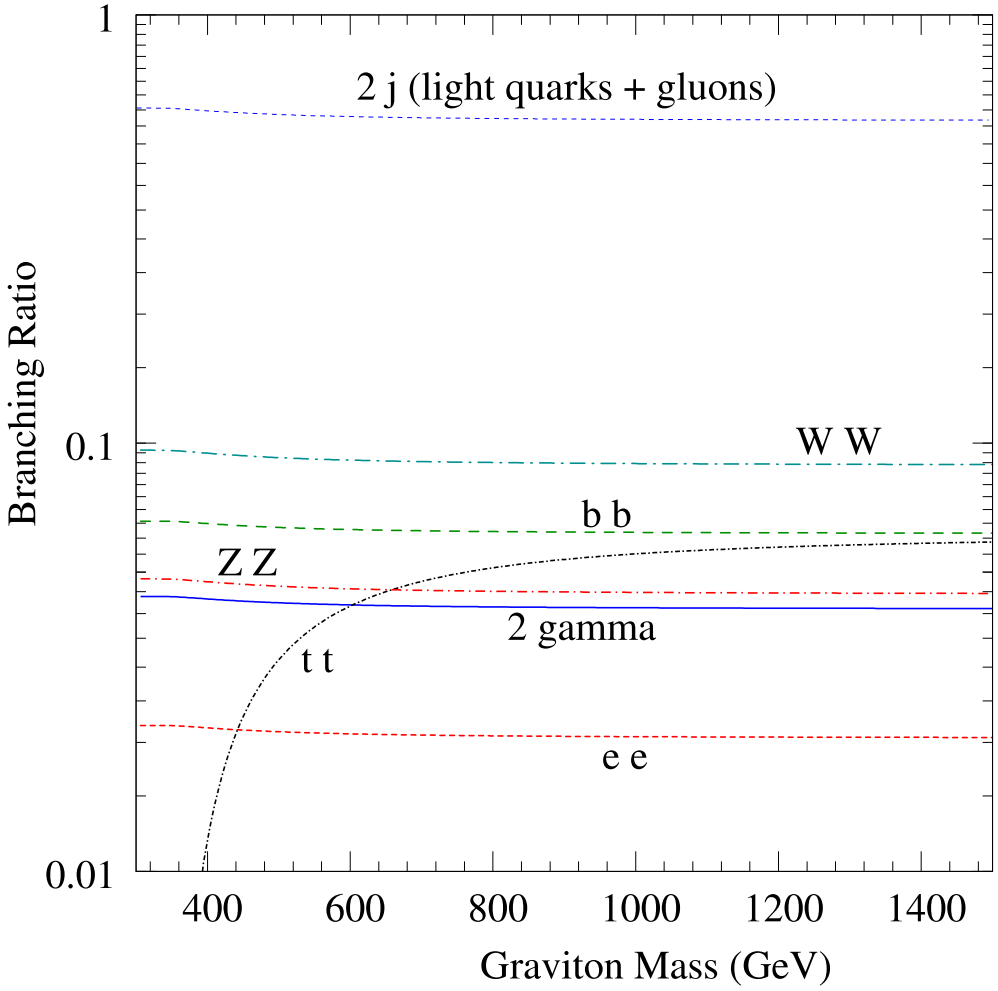

Figure 1.6: Branching ratio of an RS Graviton to different final states as a function of M_1 [17]

Chapter 2

Experimental Apparatus

2.1 LHC Accelerator

The Large Hadron Collider (LHC) is a two ring, superconducting accelerator and collider of hadrons. It is installed in the 27 km circumference cavern that was originally used for the LEP machine at CERN. It is designed to collide protons at a center of mass energy of 14 TeV, with an instantaneous luminosity of $10^{34} cm^{-2} s^{-1}$. It is currently operating at 8 $TeV$with a luminosity of 5x$10^{33} cm^{-2} s^{-1}$ as of this writing. Such a unprecedented high intensity beam precludes the use of antiprotons, as in the Tevatron. This is also the reason for the two rings of superconducting magnets, rather than a shared vacuum and magnet system. The LEP cavern is too small ($\sim 3.7m$) to house two separate rings of magnets, thus the 1,232 dipoles in the LHC are actually twin bore two-in-one magnets in the same cryostats (Figure 2.1).

To reach the full collision energy, LHC protons are first injected into the proton synchrotron (PS) and accelerated to 25 GeV. Next, they are injected to the super proton synchrotron (SPS) and further accelerated to 450 GeV. Finally, beams are injected in the LHC, and circulate in opposite directions while being acclerated to the nominal energy. The beams collide at four interaction points, corresponding to ALICE, ATLAS, CMS, and LHCb. ATLAS and CMS are general purpose experiments located at point 1 and point 5, ALICE is a heavy ion experiment, while LHCb focuses on the study of beauty (bottom) quarks. All of this is diagrammed in Figure 2.2.

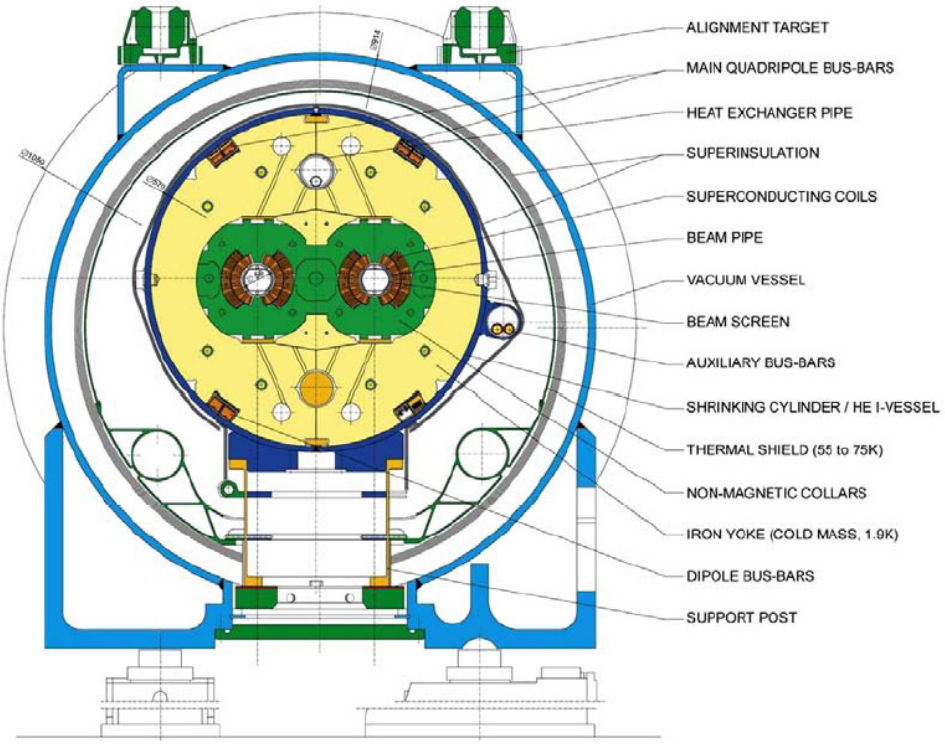

Figure 2.1: Schematic of a twin bore dipole magnet. The counter rotating beams share the cryostat in each dipole

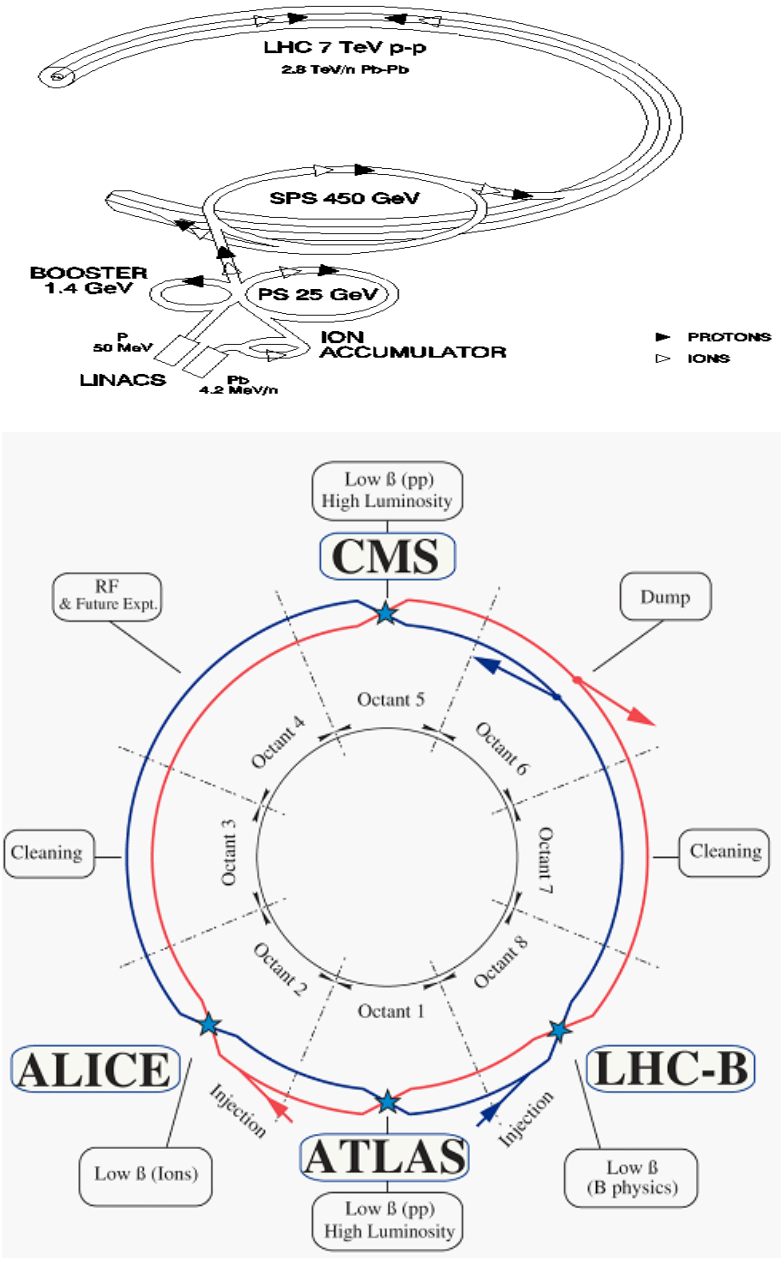

Figure 2.2: LHC injection complex (Top). Diagram of the interaction points and experiments (Bottom)

The length of the straight sections of the LHC is not optimized for the accelerator performance, as it was built for LEP collisions. The main consequence is the existence of multiple parasitic collision points due to the large number of bunches, and 25 ns bunch spacing. This is addressed by introducing a small crossing angle between the beams at the interaction point, avoiding the unwanted collisions at a slight cost in the luminosity. The luminosity thus depends only on beam parameters [18]:

$$L = \frac{N_b^2 n_b f_{rev} \gamma_r}{4\pi \epsilon_n \beta^*} F, \tag{2.1}$$

where N_b is the number of particles per bunch, n_b the number of bunches per beam, f_{rev} the revolution frequency, γ_r the relativistic gamma factor, ϵ_n the normalized transverse emittance, β^* the beta function at the Interaction Point (IP), and F the geometric factor due to the crossing angle of the beams.

Since the number of events produced for a process with cross section σ_{event} is given as

$$N_{events} = L\sigma_{event}, \tag{2.2}$$

and since σ for the processes of interest tends to increase with increasing beam energy (Figure 2.3), the exploration of rare processes benefits greatly from the high energy and luminosity of the LHC.

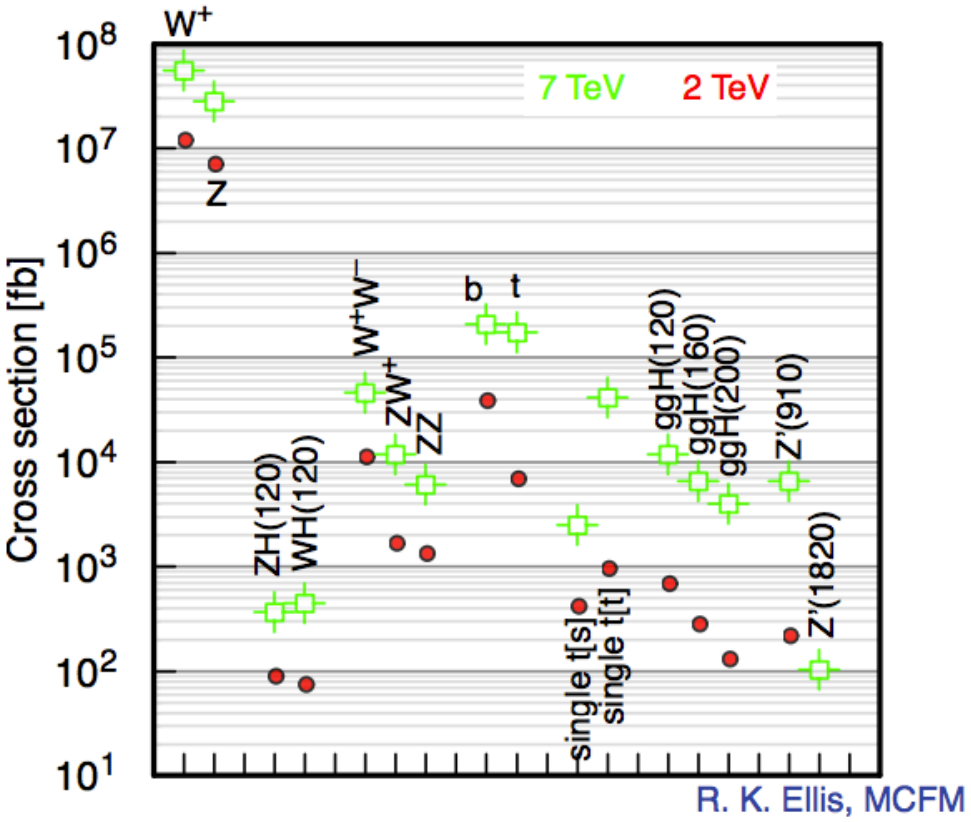

Figure 2.3: Selected absolute rates at 2 TeV (Tevatron) and 7 TeV (LHC, 2011). Note the log scale on the y-axis, and that the increase in cross section is more than linear in most cases.

2.1.1 Outlook for HL-LHC

The LHC baseline programme has the goal of producing first results in the 2010-12 run aimed at an integrated luminosity of at least 1 fb^{-1} by the end of 2011 and 4-8 fb^{-1} by 2012. The goal for 2011 was easily met by the middle of the year, and in fact more than 5 fb^{-1} were recorded during the 2011 run. After reaching the the design energy of 14 TeV, and the design luminosity of $10^{34} cm^{-2} s^{-1}$ sometime in 2014-2015, the LHC will be capable of producing $\sim$ 40 fb^{-1} per year. Under such a scenario, around 2019 the statistical gain from further running will become marginal. The run time needed to halve the statistical error on most measurements will be more than 10 years at this point. Therfore, an ambitious plan to upgrade the luminosity, beam quality, and detects is in place, called the High Luminoisy LHC (HL-LHC). The main improvements will be to the LHC injector chain, replacement of the triplet magnets with magnets of larger aperture, and upgrades to the general purpose detectors. If successful, HL-LHC would deliver $\sim$ 3000 fb^{-1} in about a decade, which is 10 times more than the estimated 200-300 fb^{-1} expected for the LHC, and many orders of magnitude larger than the $\sim$ 10 fb^{-1} collected at all previous hadron collideres.

2.2 CMS Overview

The Compact Muon Solenoid (CMS) detector is a multipurpose detector designed for discovery searches at the LHC [19]. The main motivation of the LHC is to elucidate the nature of electroweak symmetry breaking, presumed to be via the Higgs mechanism. The study of the Higgs mechanism can also test the consistency of the Standard Model above ~ 1 TeV. Additionally, there are hopes for other discoveries that could lead toward a unified theory of physics. These discoveries could manifest themselves as supersymmetry, or modifications to gravity at the TeV scale through extra dimensions. These are a few of the many reasons to investigate the TeV scale.

A hadron collider is well suited to provide the center-of-mass energy and luminosity needed to study these rare processes. However, the 7-fold energy increase and 100-fold luminosity increase over previous hadron colliders leads to experimental challenges as well. At $\sqrt{s} = 14$ TeV the cross section for proton-proton interactions would yield 10^9 interactions/s at design luminosity, which must be reduced by the trigger system down to ~ 500 events/s. The bunch spacing of 25 ns combined with the average superposition of 20 events (pileup) at design luminosity implies on order of 1000 tracks per bunch crossing. The effects of pileup in time and in space are mitigated by constructing a detector with high granularity, and fast response time, both of which lead to lower occupancy in the detector. Finally, the large flux of particles also leads to a high radiation environment, such that both the detectors and front-end electronics need to be radiation hard.

The exceptional features of CMS are a high field solenoid, a large-volume all-silicon strip and pixel tracker, and a homogeneous, crystal, electromagnetic calorimeter. CMS is cylindrical, $21.6m$ in length, $14.6m$ in diameter, and weighs $12,500$ tons. It is compact compared to the ATLAS detector in terms of its density, as it weighs more (ATLAS weighs $7,000$ tons) yet occupies a roughly 1/6th of the volume.

CMS uses a right handed coordinate system, with the x-coordinate radially inward toward the center of the LHC. The y-axis is vertical, and therefore the z-axis is counterclockwise as viewed from above. Transverse quantities, such as p_T and E_T

are thus computed in the xy plane. The origin is taken at the center of the detector, at the nominal interaction point. The polar angle θ and azimuthal angle ϕ are measured from the z-axis and x-axis respectively. The pseudorapidity η is defined as

$$\eta \equiv -ln(tan(\theta/2)) = \frac{1}{2}ln(\frac{|p| + p_L}{|p| - p_L}), \tag{2.3}$$

where p_L is the longitudinal component, along the beam axis. The pseudorapidity thus depends on the polar angle of the trajectory, but not the energy of a particle. Compare this to the definition of rapidity, which is

$$y \equiv \frac{1}{2}ln(\frac{E + p_L}{E - p_L}). \tag{2.4}$$

In the limit that the mass of a particle is negligible compared to its energy, the values for η very closely approximate the values of y. Pseudorapidity is preferred over the polar angle because production cross sections are nearly constant as a function of rapidity, apart from kinematic factors. Additionally, differences in rapidity are invariant under lorentz boosts along the beam axis, a key feature since the exact center of mass is not known a priori in a hadron collider (compared to a lepton collider). The mathematical relation between η and θ transforms the uniform range $(-90°, 90°)$ to $(-\infty, \infty)$, however most of the geometrical range is covered by small values of η.

Starting from the inside of Figure 2.4, CMS consists of a silicon pixel detector, followed by 10 layers of silicon strip detector. Combined, these form a cylindrical tracker 5.8 m in length, and 2.6 m in diameter, and cover $|\eta| < 2.4$. The purpose of the tracker is to measure the position, and determine the momentum of charged particles. The electromagnetic calorimeter (ECAL) covers $|\eta| < 3.0$ and is composed of lead tungstate crystals with face dimensions of roughly 1 Molière radius and a depth of 25 radiation lengths. The hadronic calorimeter is a sampling calorimeter made of alternating layers of absorber and scintillator, and covers $|\eta| < 5.0$, and is the last element inside of the solenoid return yoke. The solenoid was designed to give

the strongest possible magnetic field ($3.8T$) with the constraint that the size could not exceed the maximum transport size on French/Swiss roads of $\sim 7m$. Finally, the muon stations are positioned outside of the solenoid, providing coverage of $|\eta| < 3.0$ and providing both muon identification, and additional measurements of muon track momenta.

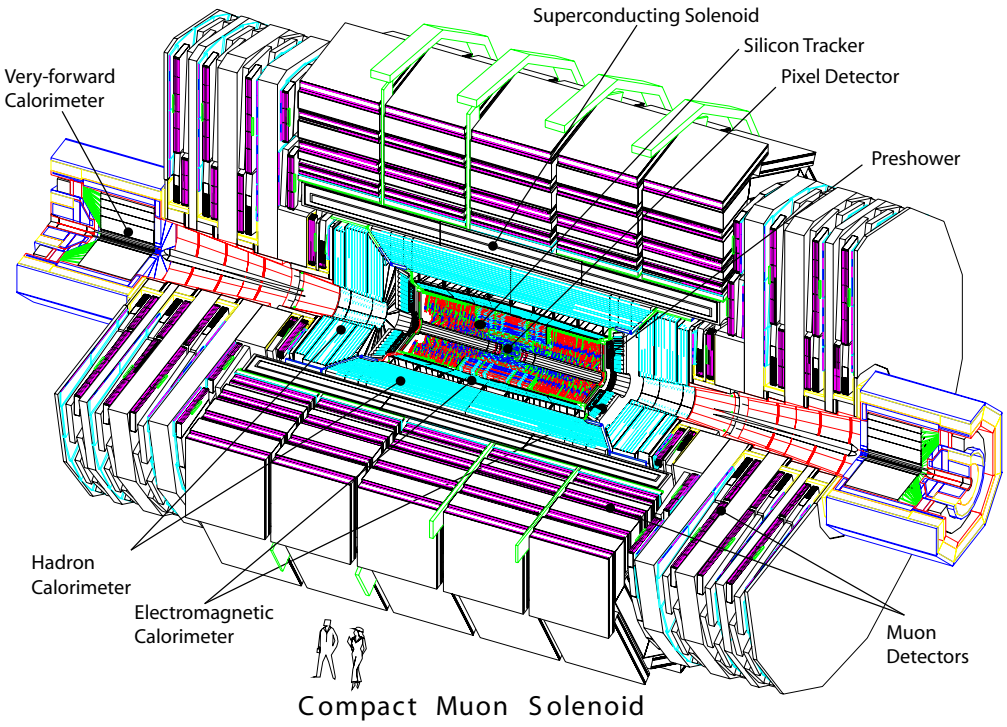

Figure 2.4: Schematic cutaway view of the CMS detector

The combination of detectors allows deductions about the underlying particle types (Figure 2.5). For example, the presence or lack of tracks can distinguish electrons from photons, which has similar profiles in the ECAL, while hadrons will deposit energy in the HCAL, and muons will pass through all systems with only minimal energy deposition.

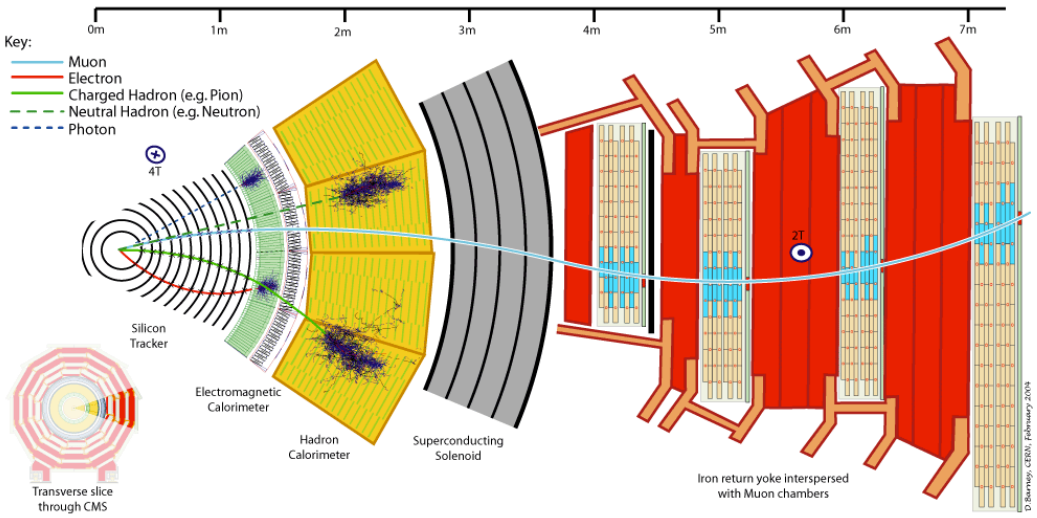

Figure 2.5: Diagram of particle interactions with CMS sub-detectors. Photons leave only deposits in the ECAL, while electrons deposit in the ECAL along with an associated hits in the tracker. Charged hadrons leave hits in the ECAL and HCAL as well as matching tracks, while neutral hadrons will leave deposits in the HCAL without hits in the tracking volume. Muons traverse the entire detector, and are primarily reconstructed from the tracks and muon stations.

2.3 Tracker

Because of the multiplicity of particles produced in each bunch crossing, and the short bunch crossing time (25 ns), the CMS Tracker consists entirely of high granularity silicon with a fast response and readout. The tracker is composed of 1,440 pixel and 15,148 strip modules, with a total active area of more than 200 m^2.

The design choices for the tracker are largely driven by the occupancy as a function of radial distance. The rate of hits falls from $1MHz$ at $4cm$ to about $3kHz$ at $115cm$, with the high rate mandating pixelated detectors below $10cm$. The pixel detector consists of 3 layers in the barrel region, at radii of 4.4, 7.3, and 10.3 cm, each with length 53 cm. The endcap regions consist of 2 disks, with radii 6, and 15 cm, at $|z| = 34.5$ and 46.5 cm. These pixel regions consist of small elements, roughly 100×150 μm, containing a total of approximately 66 million cells, which give a spatial resolution of 10 μm in the $r\phi$ plane and 20 μm in the z dimension.

Outside of the pixel region, the particle flux is reduced and allows the use of strip detectors. This includes the tracker innner barrel (TIB) and outer barrel (TOB) in the barrel, and the tracker endcap (TEC) and tracker inner disks (TID) in the endcap. The TIB consist of 4 layers, and the TOB consists of 10 layers, covering $|z| < 130$ cm and $|z| < 220$ cm. Combined, the TEC and TID extend the coverage from $|z| = 120$ cm up to $|z| = 280$ cm. The corresponding diagram and η ranges are shown on Figure 2.6.

The 15148 strip modules contain 9.3 million strips, which have a pitch between strips varying from 80 to 180 μm. The first 2 layers/rings of each part, and ring 5 of the TEC use a back-to-back configuration of strips, with 100 $mrad$ separation to give a stereo readout. This gives additional information about the z-coordinate in the barrel region, and the r-coordinate in the endcap/disk region. The geometry of the tracker guarantees at least 9 hits in every part of the region up to $|\eta| < 2.4$, while the increasing thickness as a function of r leads to resolutions of 230 and 530 μm in the inner and outer regions, respectively.

Figure 2.7 shows the material budget of the tracker in radiation lengths, increasing

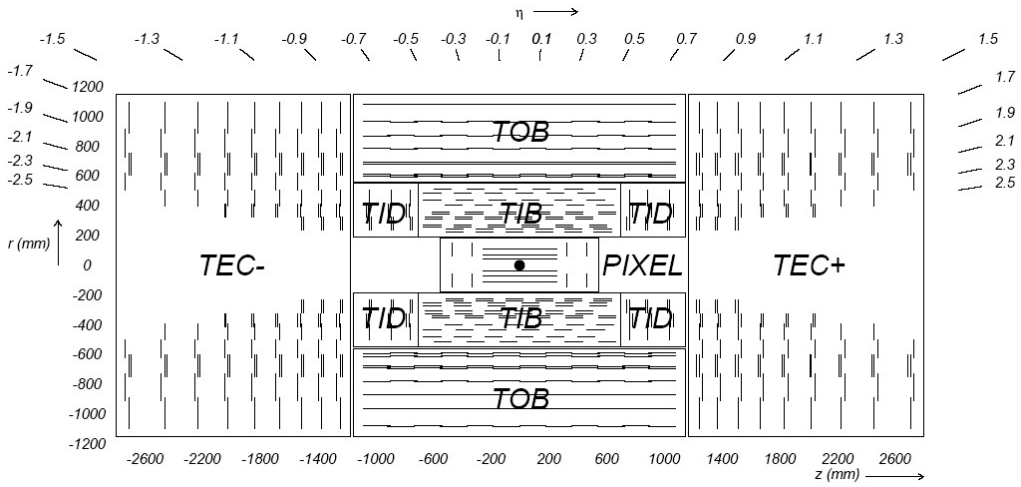

Figure 2.6: Schematic of CMS tracker. Double lines represent back to back strips which give stereo readout

from $0.4X_0$ at $\eta = 0$ to $1.8X_0$ at $\eta = 1.4$ and falling off to $1.0X_0$ at the end of the endcap.

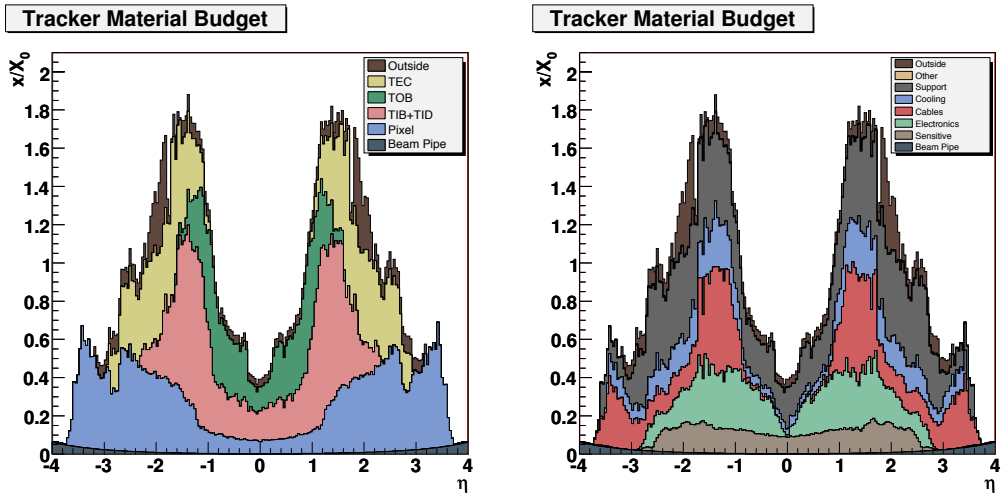

Figure 2.7: Tracker material budget

2.4 ECAL

The ECAL is composed of lead tungstate $PbWO_4$ crystals, and represents the first use of a crystal calorimeter in a hadron collider. It is hermetic and homogeneous, composed of 61200 crystals in the barrel, and 2 disks of 7324 crystals in each endcap. The endcap crystals are preceded by a preshower detector, intended to improve separation of prompt photons from $\pi^0 \rightarrow \gamma\gamma$. Light readout is by avalanche photodiodes (APDs) in the barrel, and vacuum phototriodes (VPTs) in the endcap. The high density crystals satisfy the need for a fast, high granularity detector, with reasonable radiation hardness. The use of a homogeneous crystal calorimeter also yields excellent energy resolution, which is critical for lower-mass searches such as the decay of the Higgs boson to diphotons.

The density ($8.28 g/cm^3$), radiation length (0.89 cm), and Molière radius (2.2 cm) of $PbWO_4$ crystals allow a fine grained and compact calorimeter. Additionally, the scintillation light decay time is fast, with 80% of light emitted in the 25 ns bunch crossing time. The truncated pyramidal shape of crystals in the barrel, coupled with the high index of refraction ($n \sim 2.29$) would lead to non-uniformities in light transmission, thus a single face is depolished in a controlled along the crystal length to restore the uniformity. The endcap crystals are nearly rectangular, and thus do not have this feature, as shown in Figure 2.8

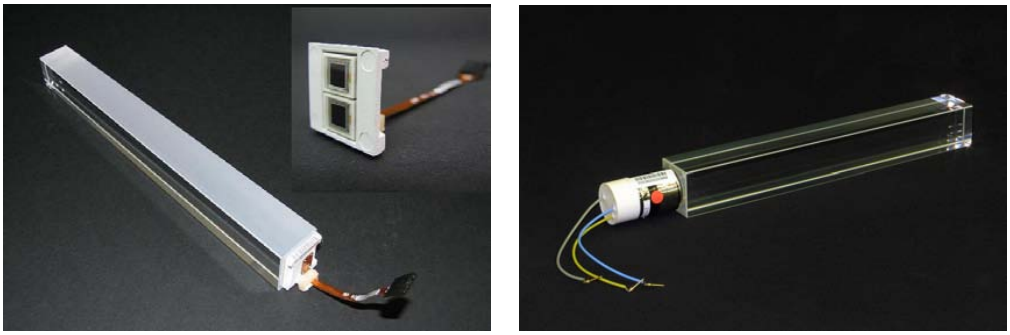

Figure 2.8: Lead tungstate crystals with photodetectors attached. (Left) Barrel crystal with upper face depolished, and capsule with 2 APDs (insert). (Right) Endcap crystal with VPT.

The crystals are subject to a high-radiation environment, which leads to the for-

mation of color centers, which are vacancies/impurities in the crystal lattice. These color centers lead to a loss of light transmission, and this damage is tracked and corrected using injected light from a laser monitoring system developed and operated by the Caltech group (Appendix 4.1).

The ECAL barrel (EB) covers up to $|\eta| < 1.479$, and is split into rings of 360 crystals in the ϕ direction and 85 crystals each along the positive and negative η directions. Each 20x85 crystal assembly is called a Supermodule, which is further broken down into modules, 3 of size 20x20, and one of size 20x25. The crystals have a shape that is slightly dependent on η, and are off-pointing by 3° from the interaction point to avoid loss of hermeticity through the intercrystal gaps. At a radius of 1.29 m, each crystal occupies 0.0174×0.0174 in $\eta - \phi$ or 2.2 cm^2 at the front face and 2.6 cm^2 at the rear. The crystal length of 23 cm corresponds to $25.8X_0$, and results in negligible leakage up to the TeV scale. The ECAL endcap (EE) covers $1.479 < |\eta| < 3.0$, and is composed of identically shaped crystals grouped in 5×5 supercrystals arranged into two halves, or dees. The circular shape is completed with 18 partial SCs along the inner and outer circumference. EE crystals are 2.862 cm^2 at the front and 3 cm^2 at the rear, with a length of 22 cm corresponding to $24.7X_0$, and are also off-pointing by 2 to 8 degrees. The design of the ECAL is shown in Figure 2.9.

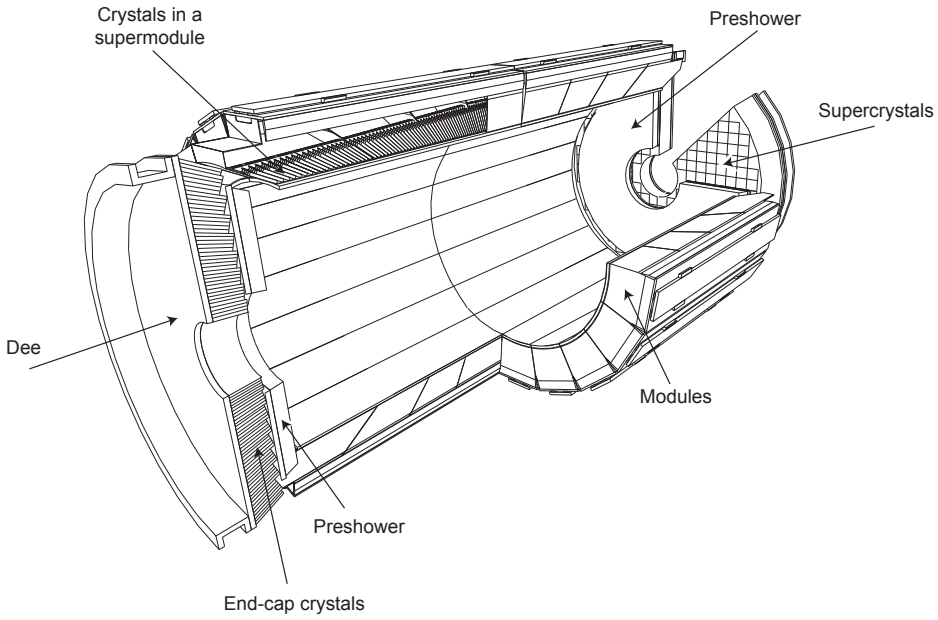

Figure 2.9: Layout of the CMS ECAL, with barrel, endcap and preshower modules

2.5 HCAL

The HCAL consists of 4 parts, the hadron barrel (HB), hadron endcap (HE), hadron forward (HF) and hadron outer (HO) (Figure 2.10).

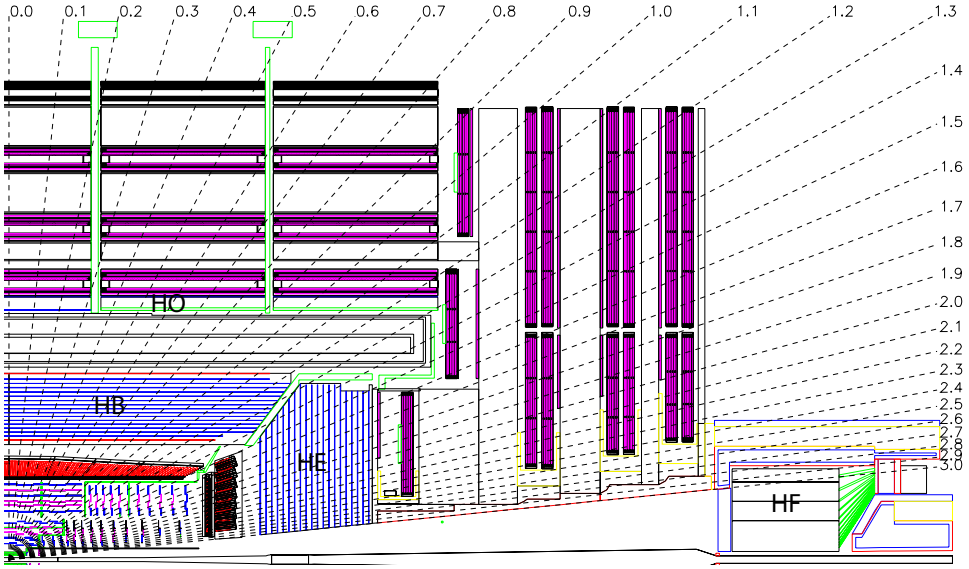

Figure 2.10: Longitudinal view of the CMS HCAL, including the locations of barrel, endcap, outer, and forward calorimeters

HB and HE consist of alternating layers of scintillator and brass absorber, while HO is a single (or double) layer. The forward calorimeter operates based on Cherenkov radiation in long and short fibers designed to provide a means to separate out EM and hadronic energy. The HB is constrained in the radial dimension by the size of the solenoid, extending from the outer of the ECAL region ($r = 1.77$ m) to the inside of the coil ($r = 2.95$ m). Because of the limited depth of HB, the HO is designed as a tailcatcher and placed outside the solenoid. Outside of $|\eta| > 3.0$ the HF extends the coverage up to $|\eta| = 5.2$. The HCAL design is shown in Figure 2.11.

The HB is a sampling calorimeter covering $|\eta| < 1.3$, and consists of 36 ϕ wedges split into two halves of the barrel. Each wedge is segmented 4-fold in the ϕ direction, and 16-fold in η, leading to a granularity of 0.087×0.087 in $\eta - \phi$. The interleaved absorber consists of a 40 mm front steel plate, 8 brass plates of 50.5 mm, 6 brass plates of 56.5 mm, and a 75 mm steel back plate. The total depth of absorber in interaction

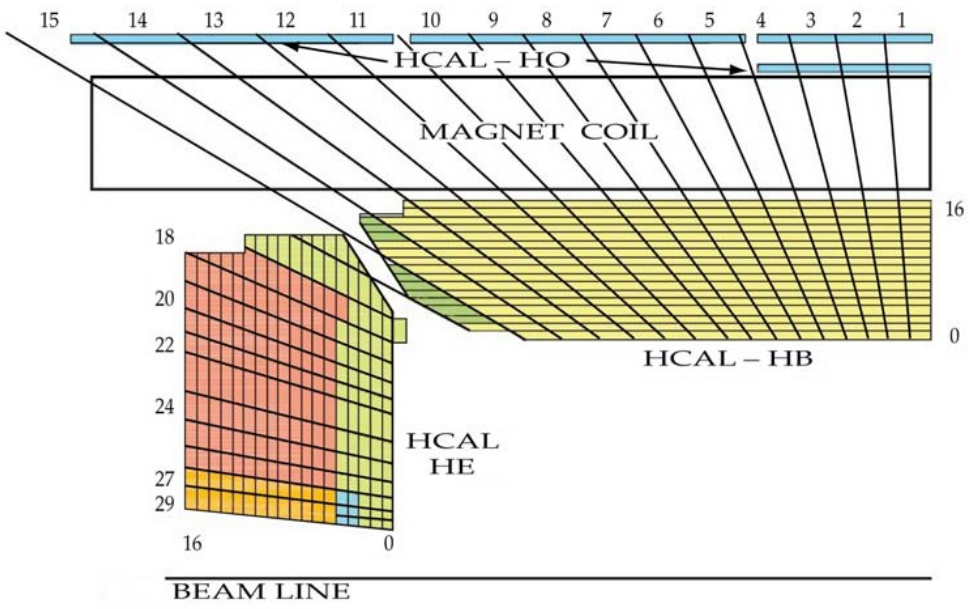

Figure 2.11: Layout of the CMS HCAL. Show are HB, HE, and HO in one quadrant

lengths (λ_I) ranges from $5.82\lambda_I$ at $\eta = 0$ to $10.6\lambda_I$ at $|\eta| = 1.3$, with the ECAL contributing an additional interaction length. Starting in front of the steel plate (layer 0), plastic scintillators sit between each layer of absorber, and the scintillation light is transmitted via wavelength shifting fibers to the Hybrid Photodiodes (HPDs) for readout.

The HE covers the most solid angle of all HCAL subsystems, from $|\eta| = 1.3$ to $|\eta| = 3.0$. The design of the HE is subject to several challenging constraints: high counting rates and radiation hardness due to the luminosity and radiation profile, non-magnetic material due to sitting at the end of the solenoid, and sufficient interaction lengths to fully contain hadronic showers. Further details of the design choices can be found in the JINST paper [20]. The $\eta - \phi$ segmentation matches that of the HB up to $|\eta| < 1.6$, and then increases to 0.17×0.17.

In the central-most region, the combined interaction length of the EB and HB is insufficient to ensure containment of hadronic showers. Thus, the HO is designed as a tail catcher, placed outside of the solenoid to utilize the coil as an additional absorber. The HO geometry is meant to match the HB segmentation as closely as possible, with 2 layers in the very central $\eta = 0$ ring, and a single layer at larger

rapidities. The total size of the HO is constrained by the start of the muon systems, but is sufficient to extend the minimum depth of the HCAL to $11.8\lambda_I$.

The HF is exposed to the highest levels of radiation of all of the HCAL. This led to the design choice of quartz fibers as the most radiation hard active medium. The fibers are split into long and short fibers, with the long fibers running the full length of the HF, while the short fibers start 22 *cm* from the front of the HF. The difference in fiber lengths is meant to separate early-starting EM showers from late-starting hadron showers. The HF also plays the critical role of providing the online luminosity measurement, relying on the linear relationship between the average transverse energy and the luminosity. The final luminosity in 2012 is now provided by the pixels, using a method described in [21].

2.6 Solenoid

The CMS magnet system is designed to provide a 4T field, although in situ it has been limited to 3.8T, to extend its life to cover the foreseen 20+ year physics program of CMS. The magnet is 6 m in diameter, 12.5 m in length, and stores 2.6 GJ at full current (Figure 2.12). The flux is returned through a 10000 ton steel yoke, consisting of 5 barrel wheels, and 2 endcaps, while the 220 ton cold mass is made of 4 winding layers of NbTi.

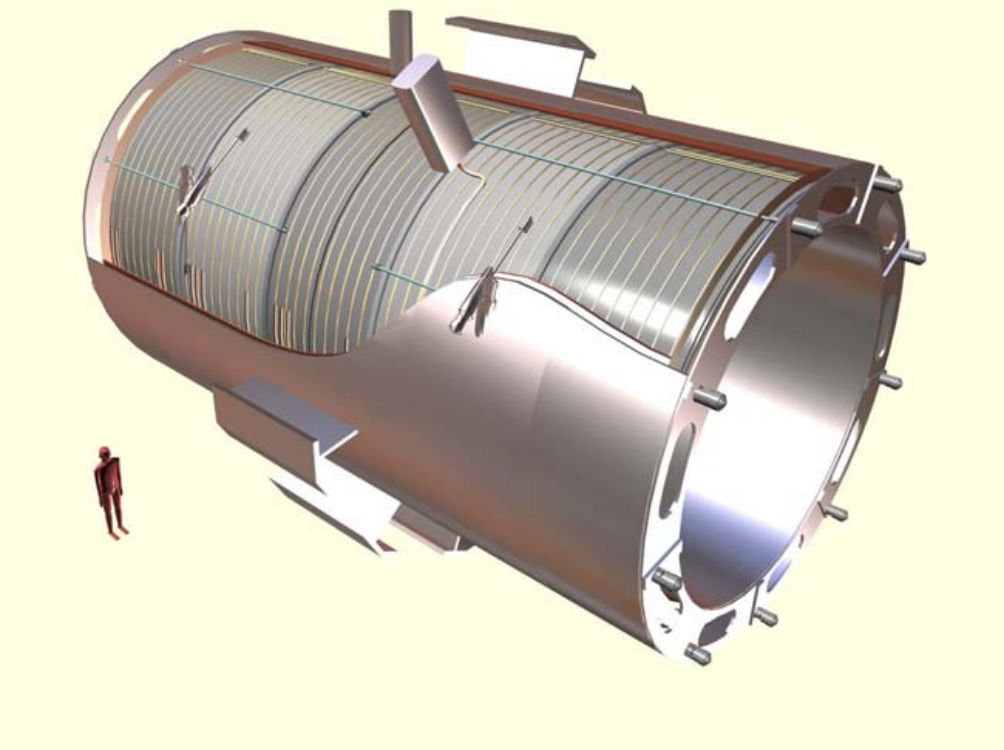

Figure 2.12: Artist's rendition of the cryostat

The solenoid is unique in comparison to previous experiments in several ways. First, the high 4T field necessitates 4 layers of windings rather than a single layer, as 4.2×10^7 amperes/turn are needed. Secondly, the large dimensions of the coil, together with the thin radial extent means that the design is sensitive to mechanical strain from the large stresses resulting from the magnetic pressure. An indicative quantity is the ratio of the stored energy to the mass, which is much higher than any

other magnet system to date (Figure 2.13).

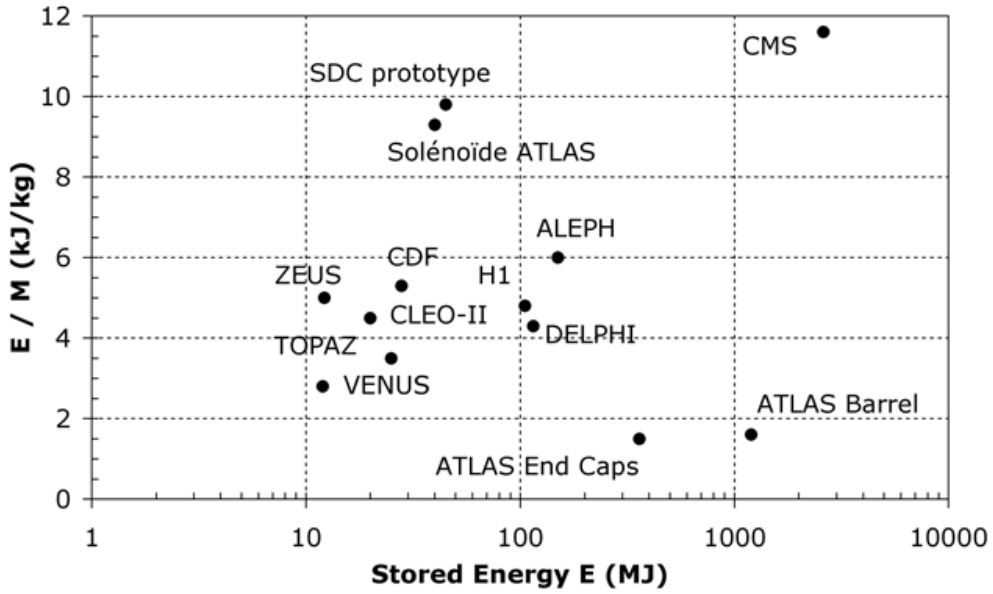

Figure 2.13: Energy/mass ratio for current and previous detector magnets

Finally, the yoke consists of 5 barrel wheels, and 2 endcaps consisting of 3 disks each, for a total of 11 elements (Figure 2.14). The main challenge during assembly was the movement and alignment of these heavy elements, accomplished through the use of air pads and grease pads. The alignment is done through a series of survey points, and has an accuracy of 2 mm with respect to the ideal axis.

Figure 2.14: View of the yoke above ground. The coil is supported by the central barrel shown in the figure

2.7 Muon Systems

The muon system consists of three parts, resistive plate chambers (RPCs), cathode strip chambers (CSCs), and drift tubes (DTs). It is designed to reconstruct the momentum and charge of muons over the entire range of LHC kinematics.

In the barrel region, the muon rate is low, and the background flux is small enough to use drift tubes. DTs cover $|\eta| < 1.2$ and are organized into four stations (Figure 2.15). Each station consist of groups of four chambers, the first two are separated as much as possible for precise $r - \phi$ measurement, and the third group for z-direction measurement. The fourth DT station only has the $r - \phi$ chambers. Each layer of cells is offset from neighboring layers to reduce dead spots, and increase reconstruction efficiency and rejection of background hits.

In the endcaps, the high-rate, high-background, high-radiation environment necessitates the use of CSCs. CSCs are fast, finely segmented, and radiation hard, covering $|\eta| > 0.9$ to $|\eta| < 2.4$ (Figure 2.16). The chambers are placed perpendicular to the beam line, with cathode wires running radially to measure $r - \phi$ and anode wires perpendicular to measure η as well as the muon timing. Combined with the measurements from the tracker, muon identification efficiency is between 95% and 99% except in the transitions between DT wheels, and between DTs and CSCs (Figure 2.17).

Because of the importance of muon triggers, and the uncertainty in the background rates at high luminosity, a complimentary muon trigger system exists, consisting of RPCs, and covering up to $|\eta| < 1.6$. The RPCs are double gap chambers, and provide a fast, independent, and highly-segmented trigger with a sharp p_T threshold. They have a good time resolution but worse position resolution than the DTs and CSCs, and help to resolve ambiguities from multiple hits in a chamber.

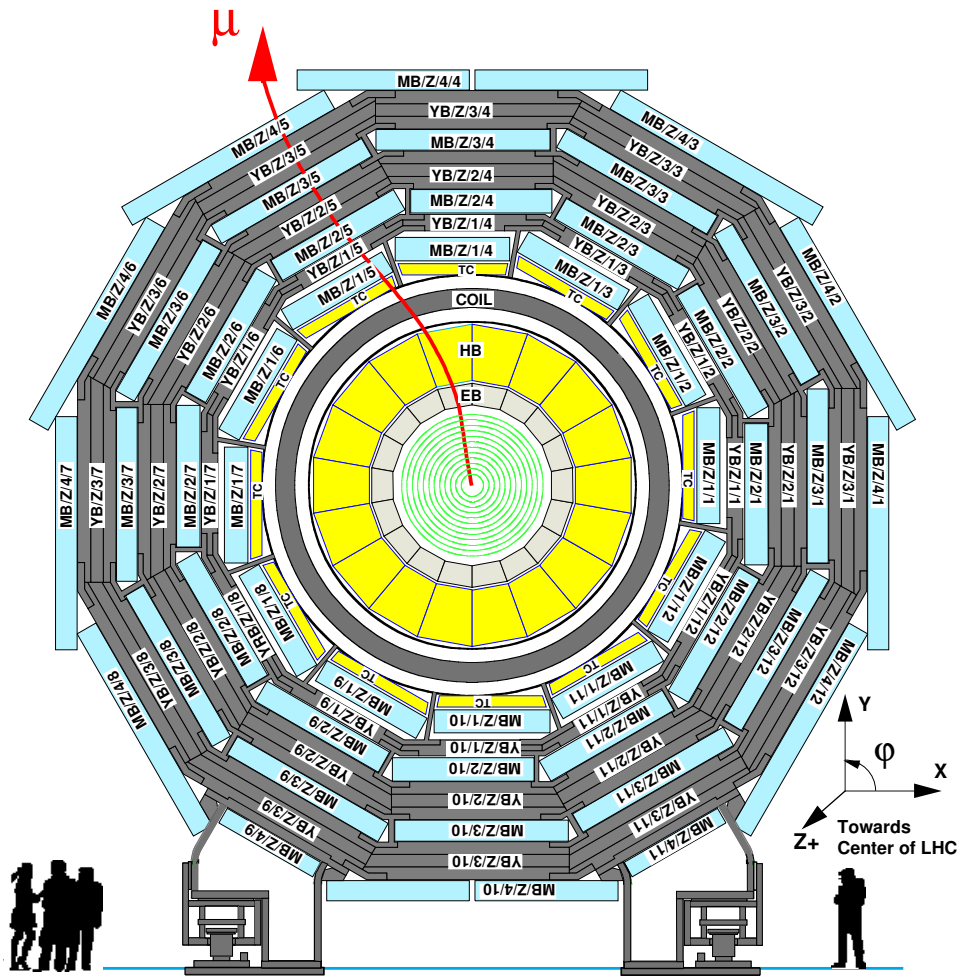

Figure 2.15: Diagram of the muon barrel (MB) drift tube system

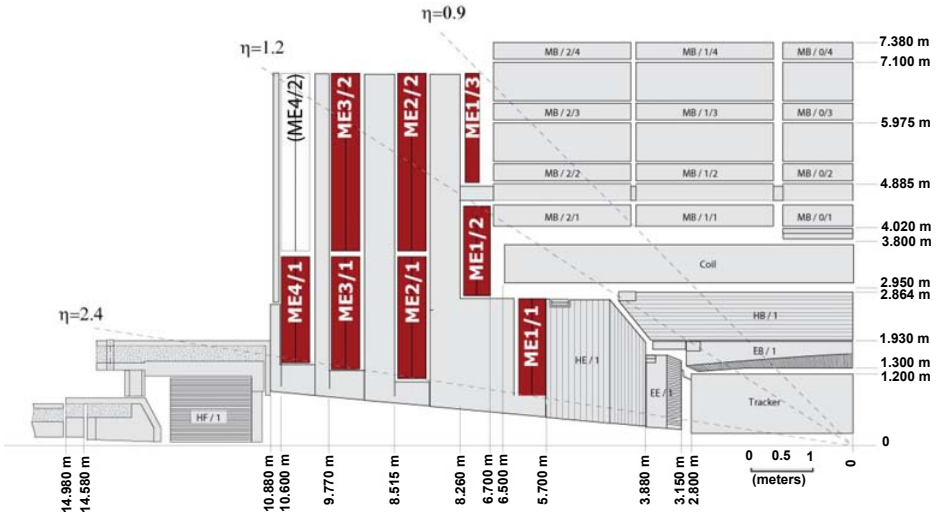

Figure 2.16: View of one quarter of CMS, with the muon endcap (ME) CSCs highlighted

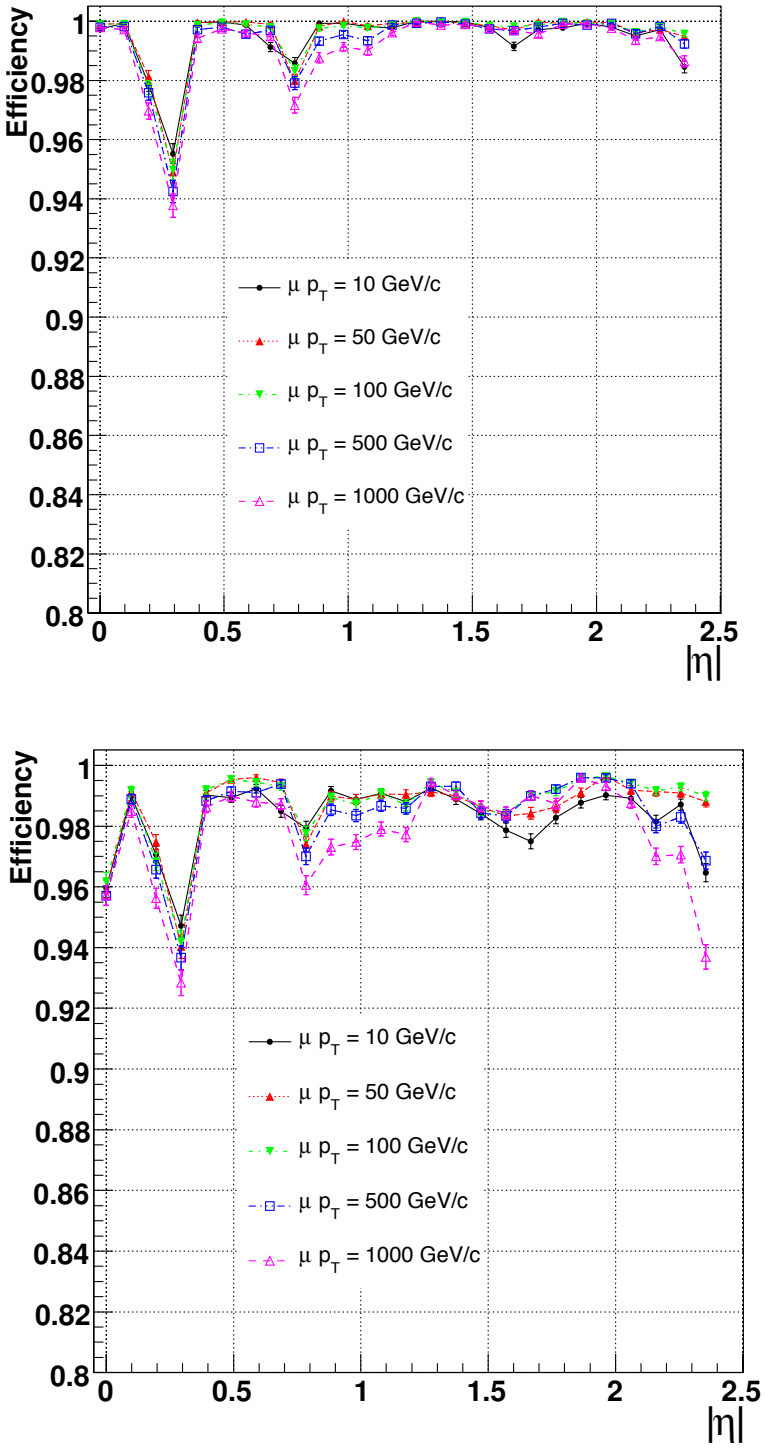

Figure 2.17: Muon reconstruction efficiency as a function of η for standalone muons (top) and muon + tracker (bottom).

Chapter 3

Reconstruction

The translation between theoretical predictions of specific particle final states to measurements made with the CMS detector is not perfect. The first challenge is to reconstruct the four-momentum of each particle, which involves both measurement of the energy deposition and, for charged particles, the measurement of track bending. For the case of photons, there are no tracks to reconstruct, so the energy measurement depends only on the resolution of the detector crystals (and any energy lost in transit), and correctly assigning the crystals to a particular photon. This is discussed in Section 3.1 The second challenge is to determine what type of underlying particle has been reconstructed, whether a photon, electron, muon, or quark/gluon which as hadronized into a jet. Techniques for this classification are addressed in Section 3.4.

3.1 ECAL Clustering

Photons incident on the ECAL deposit $> 95\%$ of energy in a 5x5 matrix of crystals. However, the presence of material in front of the ECAL leads to a significant fraction which convert to e^+e^-. The B field then leads to spreading in the ϕ direction, and thus larger spread of deposits. (Figure 3.1)

The goal of clustering algorithms then, is to collect the deposits due to conversion, and bremsstrahlung as efficiently and accurately as possible. The algorithm must decide which individual crystal deposits should be grouped together, to recover the entire energy of the original photon. The case of bremsstrahlung and conversion

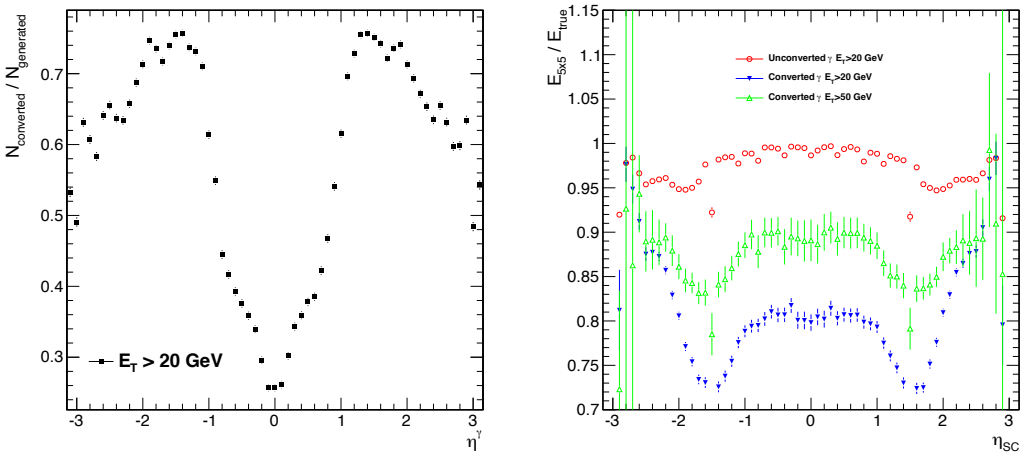

Figure 3.1: (left) Fraction of photons converting as a function of η. (right) Fraction of energy contained in 5x5 vs. η

have enough similarities in fact, that the same clustering algorithm is used for both electrons and photons.

Because of the solenoid geometry, the energy spread is confined to the ϕ direction, and thus the clustering groups crystals which are at the same η but spread in ϕ. There are two algorithms, corresponding to the different geometry of the EB and EE (Figure 3.2). 5x5 clusters are the starting point for EE, while EB uses a hybrid algorithm to match the $\eta - \phi$ geometry.

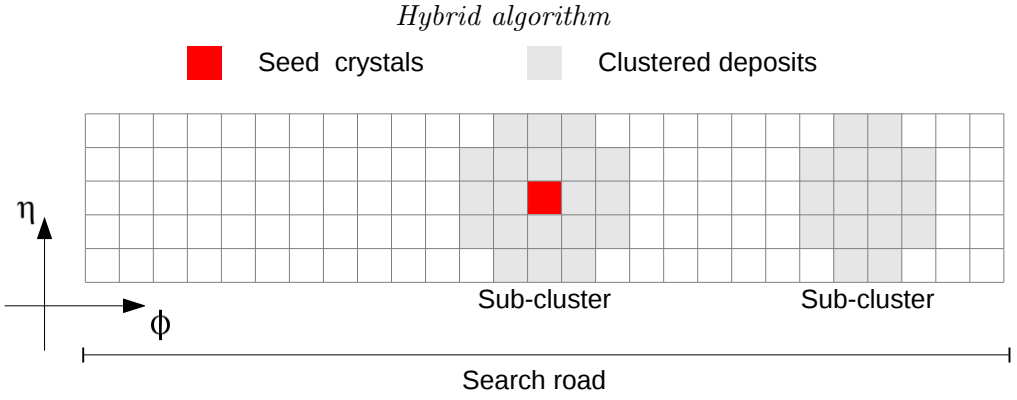

Figure 3.2: Hybrid clustering algorithm for ECAL barrel.

The Hybrid algorithm works as follow:

1. At each iteration, every crystal above threshold, $E_T > E_T^{Threshold} = 20GeV$ is

examined in descending order of energy.

2. A 5x1 domino is formed around the seed crystal in $\eta - \phi$.

3. The domino formation in step 2 is repeated for every crystal at the same η that is within the "phi-road" $|\phi_{crystal} - \phi_{seed}| < \Delta\phi_{road}$. These dominoes are added to the cluster if they are above threshold.

4. Any dominoes which are not included due to threshold are reseeded as a secondary cluster, centered on the maximum energy crystal.

5. Repeat until all crystals above threshold are examined.

The 5x5 algorithm works in a similar way, but groups crystals into 5x5 basic clusters, which are then associated to each other to form super clusters (SCs).

After the clustering algorithm forms SCs and the energy is determined, the position is measured as a weighted average of all crystals in the SC. Each crystal gets a weight $w_i = max(0, 4.7 + log(E_i/E_{SC}))$, and then the SC is promoted to a photon four-vector by using the direction vector from the primary vertex to the SC position.

3.2 Energy Resolution

The ECAL resolution has been measured in test beams, which are absent magnetic field, with minimal material before the crystals, and beams centered on the crystal faces. The resolution measured is

$$\frac{\sigma(E)}{E} = \frac{2.8\%}{\sqrt{E(GeV)}} \oplus \frac{12\%}{E(GeV)} \oplus 0.3\%. \tag{3.1}$$

The three contributions correspond to stochastic, noise, and constant terms respectively. The conditions of the test beams, and hence the result, correspond to the design performance of a perfectly calibrated detector.

As the energy deposits approach $E \sim 100GeV$, the constant term becomes the most significant, and thus the calibration and transparency corrections are very critical to the ECAL resolution. The resolution is especially important in analyses such as $H \rightarrow \gamma\gamma$, where the background rates are high, and thus the sensitivity of the experiment is directly related to the narrowness of the signal resolution. Similar logic applies to the graviton searches, where the photon energies are even higher and thus the resolution is entirely a function of the constant term, although the background rates do not dominate in this case.

3.3 Energy Scale and Linearity

In the search for a high mass resonance, there are no standard candles, such as the $Z \rightarrow ee$ to calibrate the ECAL energies. Therefore, the linearity of the detector response is yet another feature that impacts the resolution and sensitivity to high energy photon signatures.

During the beam test campaigns prior to collisions, the H4 beam line at CERN was equipped to produce a high precision energy measurement, with $dE/E \sim 0.1\%$. Special runs with electrons at fixed beam energies, between $20 - 180GeV$, measure the nonlinearity as a function of beam energy [22]. The beam was collimated to be centered on the central 2x2 mm^2 of each crystal, and the energy reconstructed from the 5x5 cluster around the central crystal.

The differential nonlinearity is shown in Figure 3.3. The maximum deviation occurs around $150GeV$, where the gain switch in the electronics occurs. The linearity of the very front end (VFE) electronics cards is measured in laboratory to be of order 0.1%.

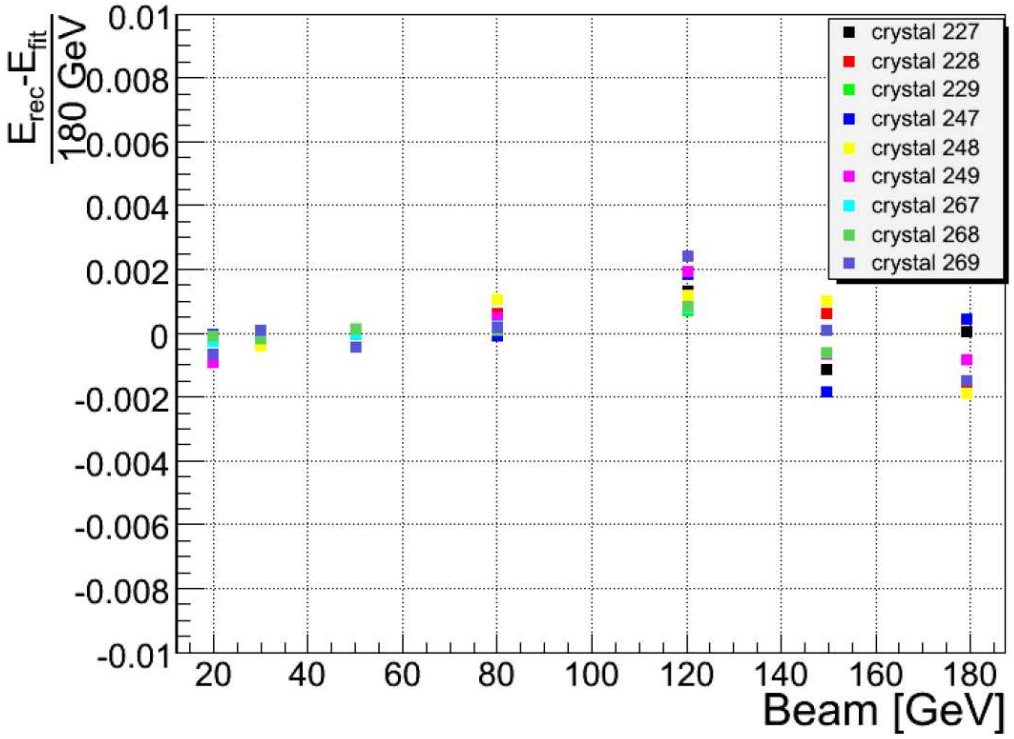

Figure 3.3: Differential linearity of ECAL crystals, measured at H4 test beam

3.4 Particle Identification

Thus far, the photon objects have been defined as SC without associated tracks, which are promoted using the primary vertex information. Prompt photons are not the only physics process that can lead to such deposits, as at high energy $E_T > 20GeV$, the photons from light neutral meson decay (π^0, η) have an angular separation which is of the same size as the ECAL granularity. These light mesons constitute the leading particle in some fraction of jet processes, and thus form the major background to photon signals. Event-by-event discrimation is difficult for such backgrounds, but statistical separation is possible using analysis of the energy deposit structure, or shower shapes, and the isolation of deposits. Deposits from the light mesons should be accompanied by deposits from the other particles in jets, thus discrimination can be achieved by restricting the amount of energy carried by neighbor particles.

3.4.1 Shower shape

Shower shapes are a powerful discriminator between prompt photons and jet background. The three that are used for this analysis are the following:

Hadronic/EM. Due to the large length of ECAL crystals, the probability of punch through by an EM shower is very small. Thus the ratio between the HCAL and ECAL deposits along a given vector can discriminate EM from jet events. H/E is defined as the ratio of the energy in the HCAL within a cone of $\Delta R = \sqrt{((\Delta\eta)^2 + (\Delta\phi)^2)} \leq 0.15$ from the SC position, to the energy of the SC.

ECAL ratios, R1, R9, etc. To distinguish EM deposits from a single source, vs overlapping deposists from two or more photons, we can use the ratio of various matrices of crystals to detect a double peak structure. Examples include R1, the ratio of max crystal to SC energy, and R9, the ratio of 3x3 energy to SC energy. Asymmetric ratios incorporating blocks such as 1x5, 2x5 also carry some information about the peak structure.

Shower moments. Another way to examine the peak structure is through the moments in the $\eta-\phi$ variables. These are computed as energy weighted covariances of the individual crystal η, ϕ coordinates, relative to the SC coordinates. In this way, we can form three covariances: $\sigma_{i\eta i\eta}$, $\sigma_{i\phi i\eta}, \sigma_{i\phi i\phi}$. The "i" notation indicates these coordinates are calculated in units of number of crystals, because geometrical projects are not linear as a function of η, as explained in Chapter 2. Because of the variation in bending at different momenta, $\sigma_{i\eta i\eta}$ is the most robust, and will be discussed further in Sec 6.2.

$$\sigma^2_{i\eta i\eta} = \frac{\sum_i^{5x5}(\eta_i + \eta_{seed} - \overline{\eta_{5x5}})^2 w_i}{\sum_i^{5x5} w_i}, \tag{3.2}$$

where w_i are the log weights previously described in the position reconstruction.

3.4.2 Isolation

Further discrimation of prompt photons and jet backgrounds utilize the difference in surrounding deposits. Only the jet backgrounds should be associated with deposits in neighboring ECAL clusters, the HCAL detector, and the tracker. In all cases, an isolation sum is formed using energy from a subdetector, within a radius $\Delta R < 0.4$, vetoing a region corresponding to a photon footprint where appropriate.

Track isolation. The scalar sum of p_T from tracks consistent with the same primary vertex. The veto region is $\Delta R < 0.04$, and also an $\eta - \phi = 0.015 \times 0.4$ strip, to protect deposits from photon conversion.

ECAL isolation. The sum of transverse energies, removing the inner region of $\Delta R < 0.06$ and an $\eta - \phi = 0.04 \times 0.4$ strip.

HCAL isolation. The sum of energy deposited in the HCAL towers, with a veto region of $\Delta R < 0.015$.

The veto regions are chosen so that the response for prompt electrons and photons are similar, allowing extrapolation of results from one to the other [23].

3.5 Beam backgrounds

One of the unique backgrounds to diphoton searches at CMS is that of beam halo decays (typically into muons) that occur in the beam line before reaching the interaction point. Such particles traverse the detector parallel to the beam line, and can leave small deposits along η in the ECAL (Figure 3.4). In all other particle IDs such deposits would be eliminated due to the lack of corresponding hits in the tracker. However, lack of track requirement for photons requires that these events be removed through other means.

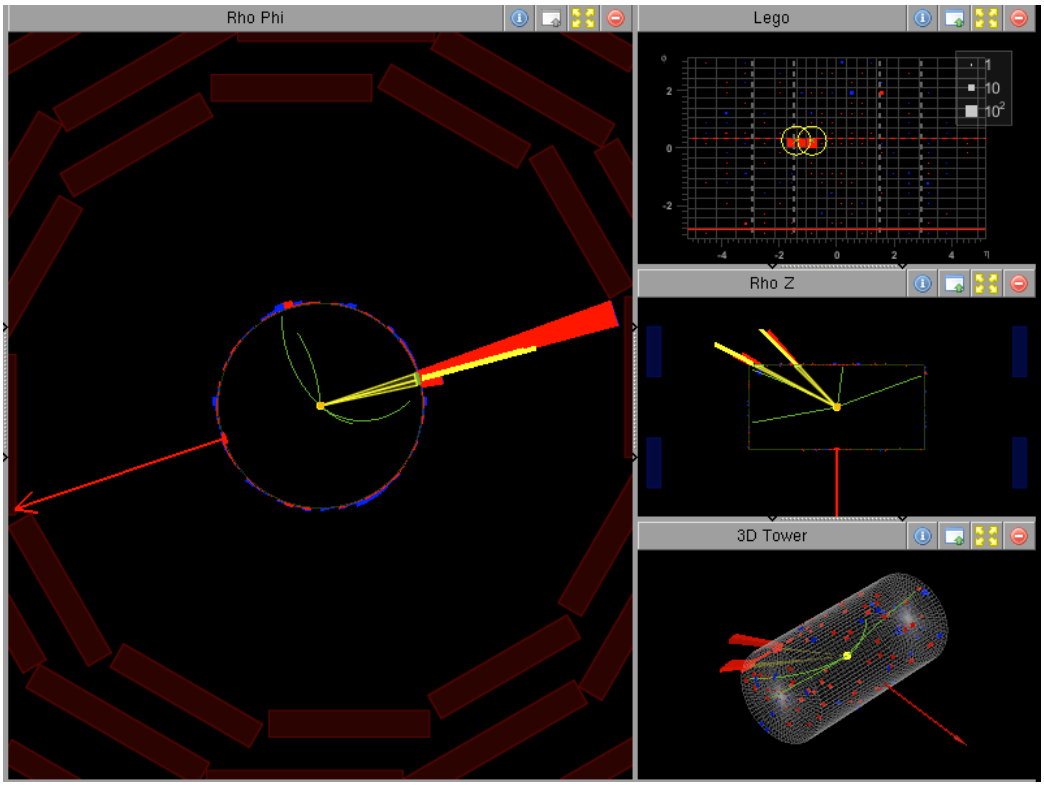

Figure 3.4: Event display of beam halo event

Normally, the shower shape variable $\sigma_{i\eta i\eta}$ will be distorted in such deposits which, in addition to the rarity of such double deposits, is why there is no contamination of beam halo in the tight-tight signal region. However, when the constraint on shower shape variable or other isolation variables are relaxed, as in the data driven background estimation, the effect of beam halo is clearly found, in the low $M_{\gamma\gamma}$ control region (Figure 3.5). The Monte Carlo (MC) simulation does not include these beam

particle processes, and thus a discrepancy arises. This data/MC anomaly is limited to the low $M_{\gamma\gamma}$ region because the energy deposits from such muons are small, and because of the geometric limitation that the hits occur at most at the two ends of the barrel ($\eta = 1.44$).

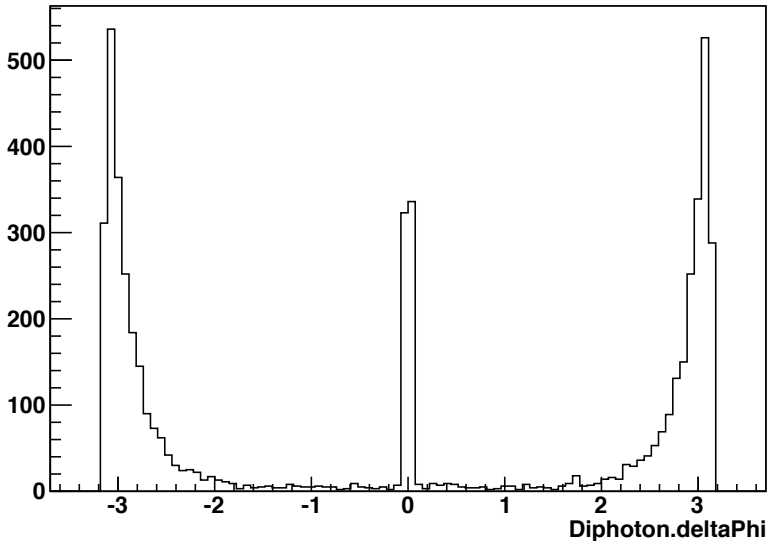

Figure 3.5: $\Delta\phi$ of candidates in the loose loose sample. The peak around 0 is due to beam halo

The top plot in Figure 3.6 shows a double curve structure, which corresponds to halo events from either beam direction, with the advanced arrival times relative to collision events corresponding to the geometrical difference in flight for particles to enter parallel to the beam line, vs. those that travel to the center of the detector and then outward from the interaction region. While there could be consideration toward using a timing based exclusion of these events (Figure 3.6), the efficiency of such a cut is no more optimal than a spatial cut. In fact it turns out that the simplest exclusion is to remove a small part of the phase space, requiring $\Delta\phi > 0.05$, removing all known halo events, with minimal impact on the signal yield. With the addition of this beam halo veto, the anomaly in the low $M_{\gamma\gamma}$ control region is removed.

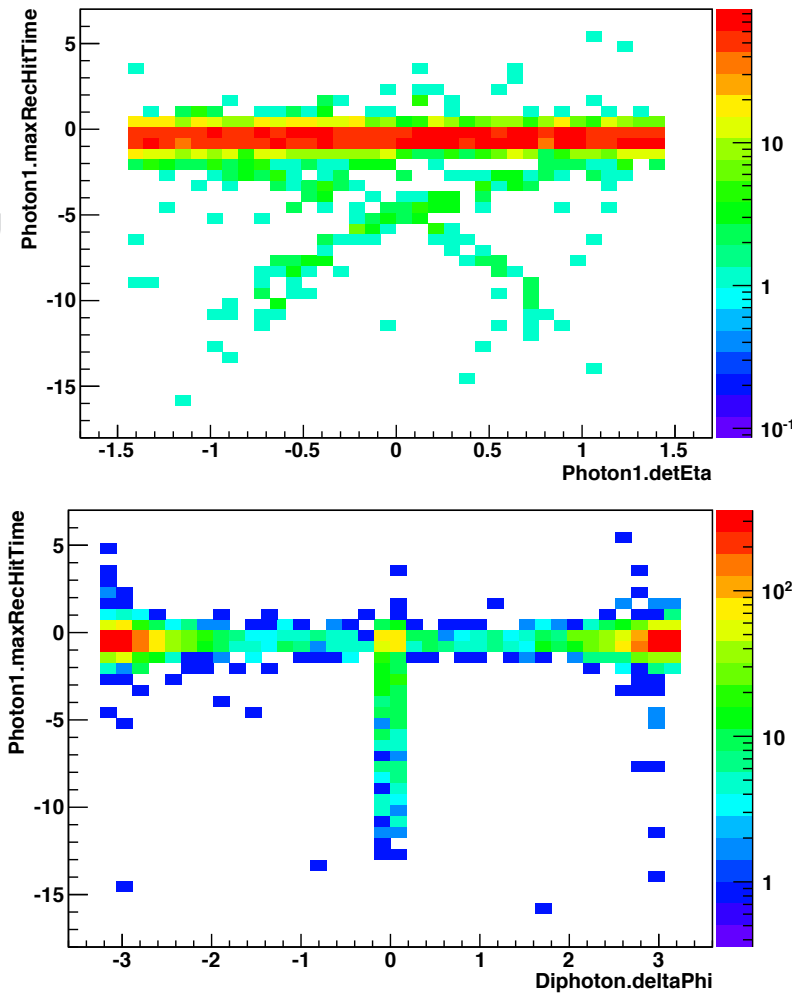

Figure 3.6: Timing vs. η of events (top). Timing vs $\Delta\phi$ of events (bottom).

Chapter 4

Laser Monitoring

4.1 Overview

One of the unique features of CMS is the crystal electromagnetic calorimeter, a first of its kind in a hadron collider enviroment. While this design allows unprecedented precision in energy measurements, the response of the crystals is subject to change, under damage from the high radiation dose rates [24]. The suspected mechanism for the transparency change of the crystals is the formation of color centers, points in the crystal lattice where an ion has been displaced due to external radiation [25]. These color centers in turn change the local potential, and thus the scintillation light response of the crystal.

To compensate for this type of process, CMS utilizes a laser monitoring system, which is both designed and operated by the Caltech group. The overall idea is to use a fixed, stable input (the laser) to monitor the light yield of the crystal over short time periods, where the change in transparency can be followed with an accuracy that maintains the excellent resolution of the ECAL. The assumed form of the transparency change is the following:

$$\frac{E(t)}{E(t_0)} = (\frac{L(t)}{L(t_0)})^{\alpha} \tag{4.1}$$

where $E(t)$ is the crystal response to electrons, $L(t)$ is the crystal response to laser light, and α is a constant for each given crystal.

4.2 Light distribution system

The laser light, via a network of switches and optical fibers, is distributed to all ECAL crystals in sequence, as well as a set of PN diodes, which deliver the reference measurement for the amount of laser light generated. All of the laser light injection is done during LHC beam gaps, which occur each 90 μsec and last for 3 μsec, less than 1% of the beam gap time is needed to cycle through the entire ECAL every 20-30 minutes, with a significant portion of the time devoted to the optical switching. The diagram of the optical distribution system is shown in Figure 4.1.

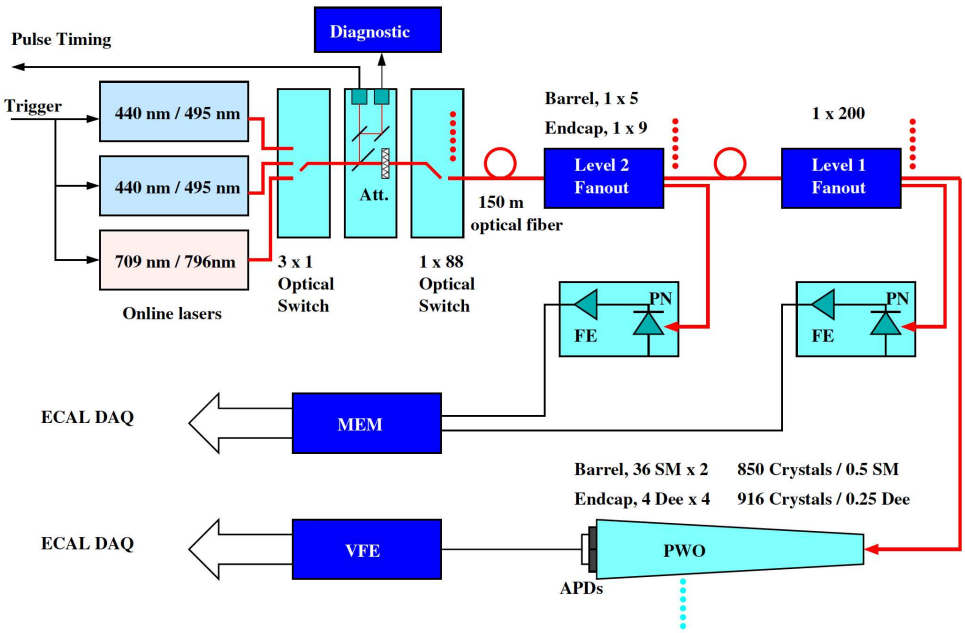

Figure 4.1: Diagram of Laser Monitoring Optical Components

4.3 Online reconstruction

The main deliverable from the laser system is the correction for the avalanche photodiodes (APD) of the ECAL. The transparency change is captured in the variable APD/PN for each crystal as a function of time, and updated each 90 μsec as new monitoring data arrives. The transparency ratio, along with a few pulse shape parameters, are stored in the Online Master Data Storage (OMDS) database, where they

are later transferred to offline databases to be used in the reconstruction of ECAL objects. The workflow for the transparency correction system is shown in Figure 4.2.

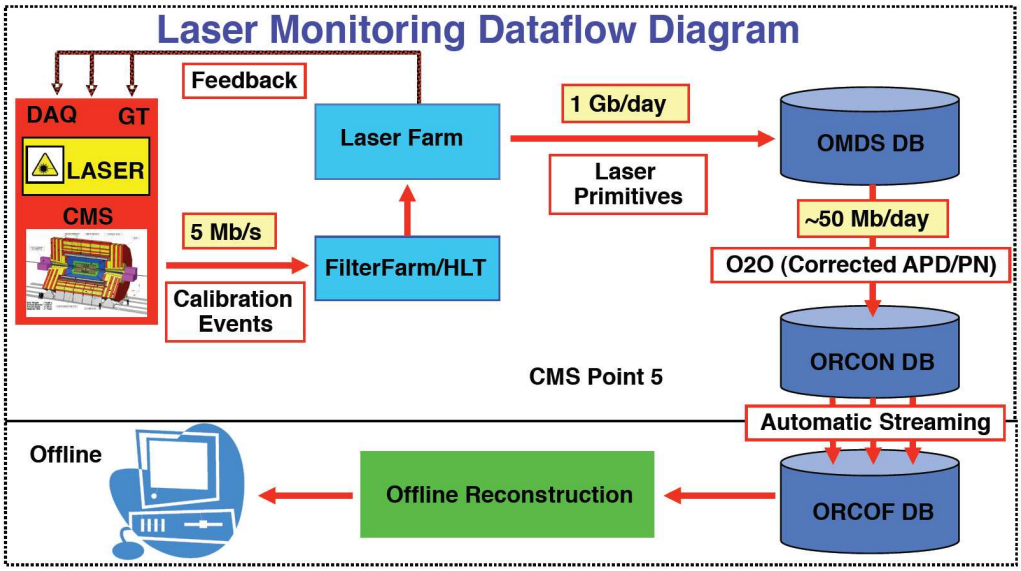

Figure 4.2: Flowchart of Laser Monitoring System

4.4 Performance with 2011 data

Each point in Figure 4.3 is computed from 12000 selected W-¿enu events with the reconstructed electron located in the ECAL Barrel. The E/p distribution for each point is fitted to a template E/p distribution measured from data (using the entire 2011 dataset) in order to provide a relative scale for the E/p measurement versus time.

The history plots are shown before (red points) and after (green points) corrections to ECAL crystal response due to transparency loss are applied. The magnitude of the average transparency correction for each point (averaged over all crystals in the reconstructed electromagnetic clusters) is indicated by the continuous blue line.

A stable energy scale is achieved throughout the 2011 run after applying transparency corrections to the ECAL data. The average signal loss of 2.5% in the ECAL barrel is corrected with an RMS stability of 0.14%.

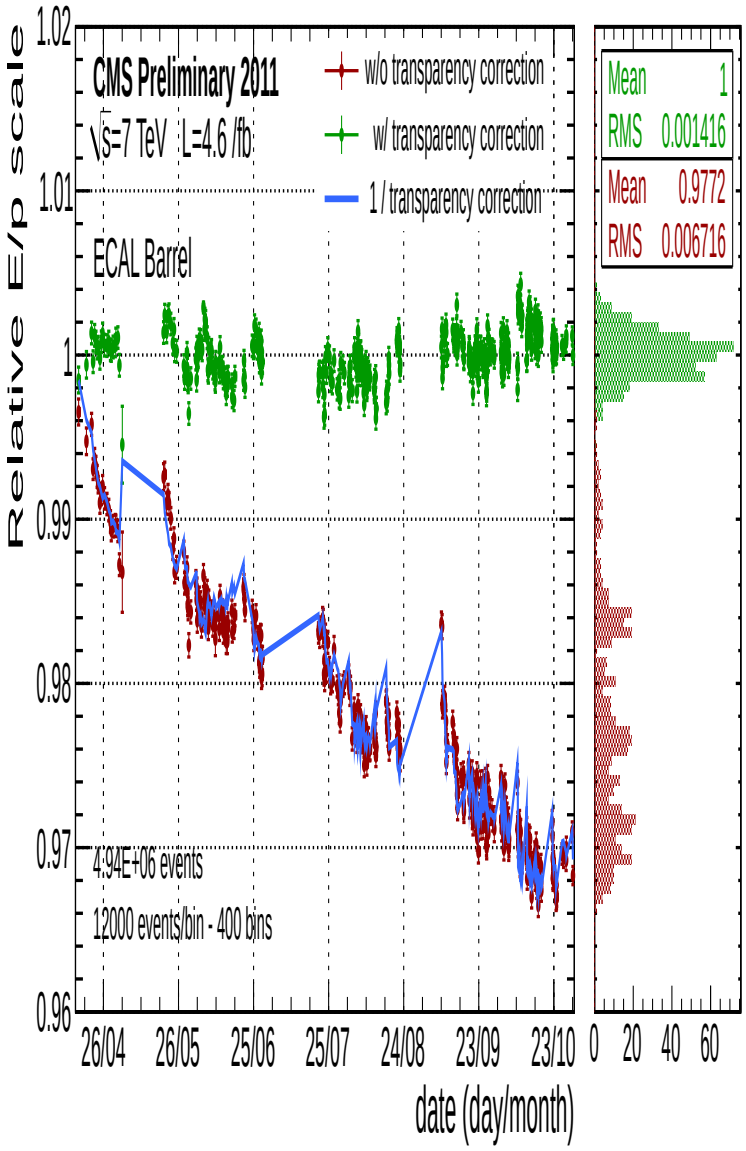

Figure 4.3: History plot for 2011 data of the ratio of electron energy E, measured in the ECAL Barrel, to the electron momentum p, measured in the tracker

Figure 4.4 includes only electrons with low energy loss through bremsstrahlung in the CMS tracker. The plot shows the improvements in $Z \rightarrow e^+e^-$ energy scale and resolution that are obtained from applying energy scale corrections to account for the intrinsic spread in crystal and photo-detector response, and time-dependent corrections to compensate for crystal transparency loss.

The former are determined using three independent methods: in-situ phi-symmetry,

beam-induced muon data, and di-photon invariant mass plots from pi0 and eta decays. The latter are measured using laser monitoring data, which is recorded in the LHC abort gaps during physics data taking. The position of the peak of the $Z \to e^+e^-$ invariant mass plot in data is used to calibrate the overall energy scale of the calorimeter.

The instrumental resolution (width of the Crystal Ball function convoluted to the $Z \to e^+e^-$ invariant mass lineshape) after preliminary energy calibration of 2011 data is measured to be 1.0 GeV in the ECAL Barrel.

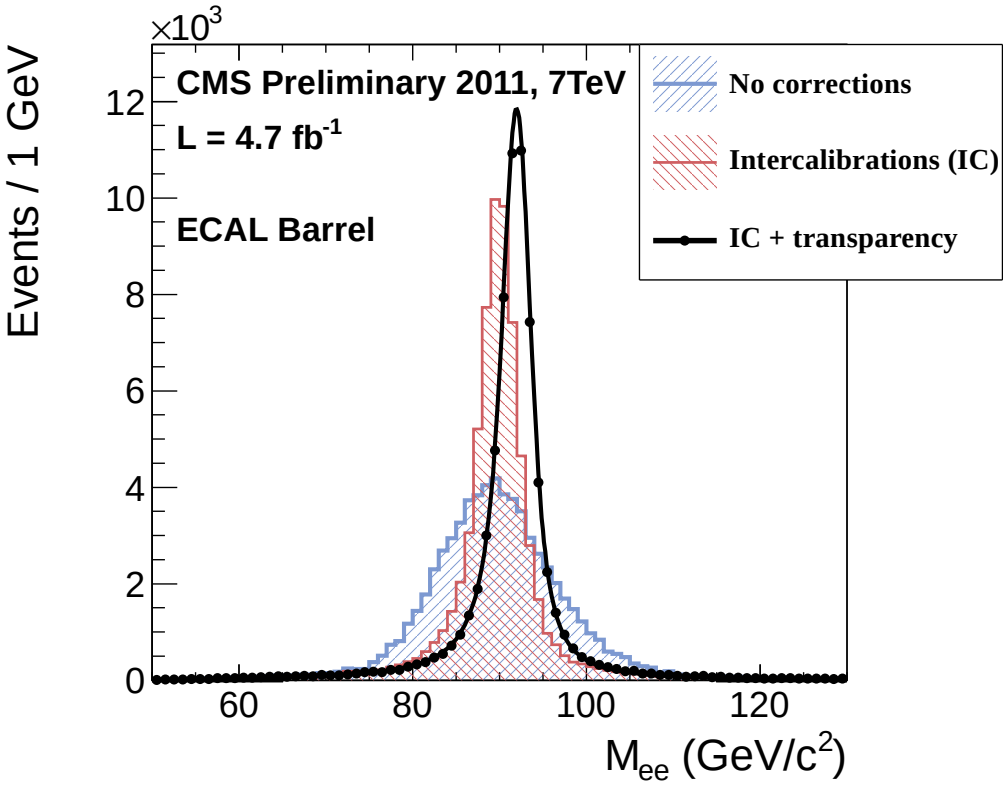

Figure 4.4: $Z \to e^+e^-$ invariant mass plot for 2011 data, from the reconstruction of di-electron events with both electrons in the ECAL Barrel

Chapter 5

Analysis and Event Selection

The goal of this analysis is to measure the rate of diphoton production as a function of mass, and either confirm the existence and measure the properties of one or more high mass resonances stemming from extra dimensions; or, in the absence of such a feature, to set upper limits on new physics processes of this kind.

The background prediction cannot be formed by fitting mass sidebands, as previous analyses [26, 27, 28] have already constrained the search to high mass regions where the rate in data will be either low, or zero. Additionally, a single-sided fit would not accurately estimate the high-mass region, as the lower-mass regions have a higher fraction of backgrounds from γ+jet and di-jet events, while the fraction of diphoton backgrounds rises at higher masses. Therefore, the background estimation is done by using a data-derived ratio of misID jets, summed with simulation samples of SM diphotons. If this procedure leads to agreement between the summed background expectation and the observed data in the lower-mass region, it is assumed that the simulation and NLO calculations for the diphotons are reliable, and therefore can be used as the background prediction at high mass.

The expected signal rate and signal rate is determined from simulation samples, and calculation of NLO cross sections for RS gravitons. In all cases of simulation, the efficiency for photon reconstruction and selection is normalized to the data by the calculation of ratios from known processes, such as $Z \to e^+e^-$ for the overall data/MC efficiency ratio, and $Z \to \mu\mu\gamma$ for the efficiency of the track veto algorithms.

5.1 Dataset and Trigger

This analysis uses data collected in 2011. The integrated luminosity delivered by the LHC, and collected by CMS is shown in Figure 5.1. The total luminosity delivered by the LHC was 6.1 fb^{-1}, while that recorded by CMS was 5.6 fb^{-1}. This is split into the two run periods, 2011A and 2011B, corresponding to lower and higher levels of pileup. Run 2011A contains the 2.2 fb^{-1} used for this analysis, and is further split into four dataset/periods corresponding to different states of the detector calibration.

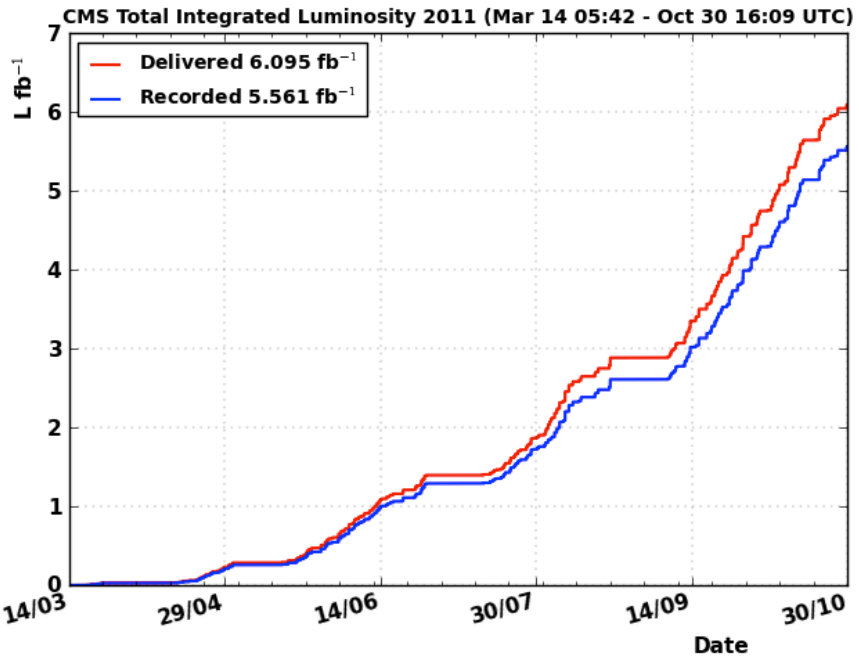

Figure 5.1: Delivered and recorded luminosity for 2011 data taking. The plateau region around August/September demarcates the two run periods of the year.

In addition to the calibration conditions, The 2.2 fb^{-1} dataset contained three distinct diphoton trigger versions, with p_T requirements on the leading photon which started from 33 GeV and increased as the luminosity increased, due to the limited trigger and data storage bandwidth, reaching 60 GeV by the technical stop at the end of August. Since the final analysis selection utilizes a much higher mass region, the strategy is to set offline p_T cuts at 70 GeV per photon, well above the highest

diphoton trigger during the entire period. The trigger selection is thus the logical OR of the highest p_T diphoton trigger from each period, and does not contain any trigger based object selection. This type of trigger selection is fairly uncommon among CMS analyses, which are usually constrained by the trigger/data taking rate to include some level of trigger based object selections.

5.2 Photon Identification

The strategy for Photon identification (ID) for this search, and all Exotica group photon searches for 2011 is driven by two main factors:

- optimization of the efficiency for channels with high expected S/B, and
- selection of a suitable set of "tight" and "loose" identification criteria to derive data-driven jet-misidentification-rate functions.

The definition of the "loose" ID is determined by choosing a set of isolation cuts which select a high statistics sample of potentially misidentified jets, and combining with an inversion of the "tight" ID isolation cuts to ensure orthogonality of the two IDs. The "loose" ID is chosen by construction to have negligible contribution from true photon processes compared to the jet backgrounds.

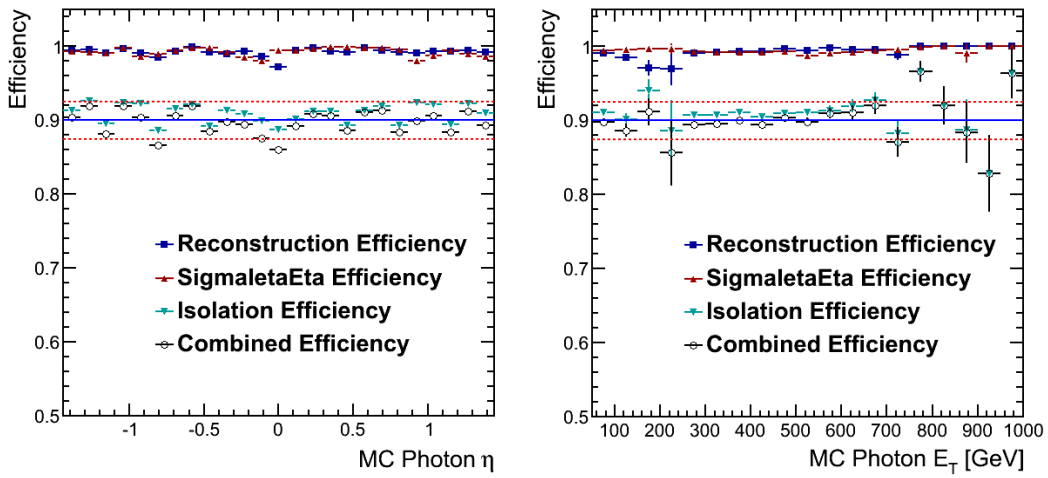

Figure 5.2: Photon ID efficiency

Criteria	Requirement
Tight ID	
H/E	< 0.05
Track Veto	No Pixel Seed
ECAL Isolation	$(0.06 < \Delta R < 0.4) < 4.2GeV + 0.006 \cdot p_T$
HCAL Isolation	$(0.15 < \Delta R < 0.4) < 2.2GeV + 0.0025 \cdot p_T$
Track Isolation	$(0.04 < \Delta R < 0.4) < 2.0GeV + 0.001 \cdot p_T$
$\sigma_{i\eta i\eta}$	< 0.013
Loose ID	
H/E	< 0.05
Track Veto	No Pixel Seed
ECAL Isolation	$(0.06 < \Delta R < 0.4) < min(5 * (4.2GeV + 0.006 \cdot p_T), 0.2 \cdot p_T)$
HCAL Isolation	$(0.15 < \Delta R < 0.4) < min(5 * (2.2GeV + 0.0025 \cdot p_T), 0.2 \cdot p_T)$
Track Isolation	$(0.04 < \Delta R < 0.4) < min(5 * (3.5GeV + 0.001 \cdot p_T), 0.2 \cdot p_T)$
Inversion of Tight ID	
$\sigma_{i\eta i\eta}$	> 0.013 OR
ECAL Isolation	$(0.06 < \Delta R < 0.4) > 4.2GeV + 0.006 \cdot p_T$ OR
HCAL Isolation	$(0.15 < \Delta R < 0.4) > 2.2GeV + 0.0025 \cdot p_T$ OR
Track Isolation	$(0.04 < \Delta R < 0.4) > 2.0GeV + 0.001 \cdot p_T$ OR

Table 5.1: Photon ID: tight and loose definitions

The efficiency of the ID is measured from MC sample of prompt photons, plotted in Figure 5.2, and found to be 90.0 ± 2.5% The variation with respect to η and E_T is taken to be a systematic uncertainty on the photon identification efficiency.

The main distinguishing feature between electron and photon energy deposits in the ECAL is the presence or absence of a corresponding track, and discriminated by the tracker pixel seed veto. The pixel seed veto efficiency is measured from $Z \rightarrow \mu\mu\gamma$ events, by using the kinematics of the reconstructed Z mass, and the independent identification of the muons to select true photons in data. The efficiency of these selected photons to pass the pixel seed veto is found to be 96.6 ± 0.5%. [29]

Additionally, it is necessary to account for an overall difference in the photon event rates between the simulations and data. This is determined by assuming a similarity between the data/Monte Carlo (MC) ratio for electrons and photons, and by studying the efficiency of electron reconstruction from Z decays. The Data/MC scale factor is determined from a "tag and probe" analysis of $Z \rightarrow e^+e^-$, where one electron is subject to strigent selection requirements (the "tag"), along with the constraint that the two selected objects have a reconstructed mass close to the Z mass. The second

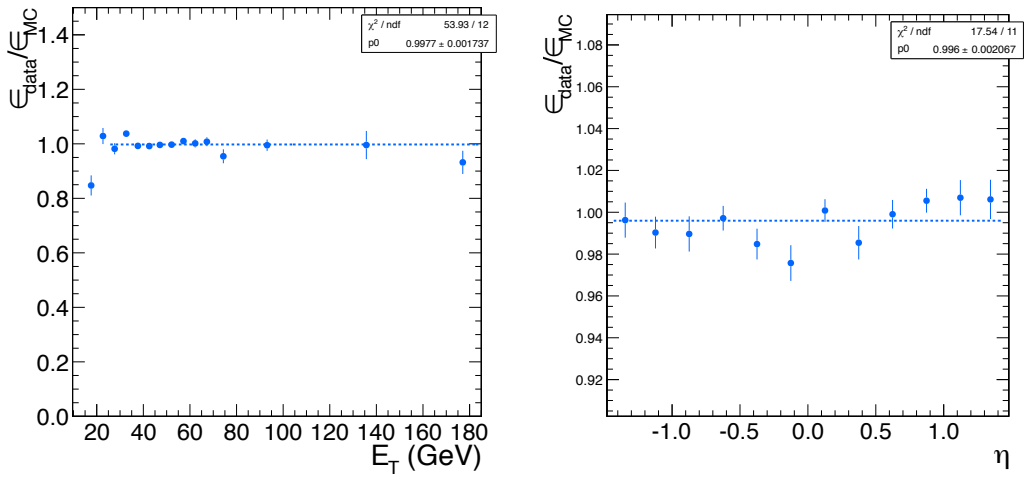

Figure 5.3: Data/MC scale factor, measured with tag and probe electrons from $Z \rightarrow e^+e^-$

object then forms the "probe", and its selection rate is taken as the efficiency. Any features arising from the kinematics of Z decays are removed by taking the ratio of this efficiency measured in data and in MC simulation samples. The ratio is found to be 1.005 ± 0.034 [30], as shown in Figure 5.3, and is applied to all MC photon samples, both signal and background.

Along with the efficiency considerations, as the year progressed the robustness of the selection to the effects of pileup also became important. For the 2011A dataset, the pileup was fairly low, with the average number of reconstructed vertices, $n_{vertices} \sim 6$ during this period. The handling of pileup is also simpler in this case, since the signal to background ratio is high, and the tight selection is not too stringent, and is optimzed to have high signal efficiency ($\sim$ 90%). The efficiency of the "tight" selection as a function of the pileup is shown (black line) in Figure 5.4, and for the range of pileup that existed for the 2.2 fb^{-1} dataset, an additional 4% systematic is assigned to the ID efficiency. For illustration, a much tighter selection (red line) is shown in the same figures, and exhibits a much stronger dependence on the pileup.

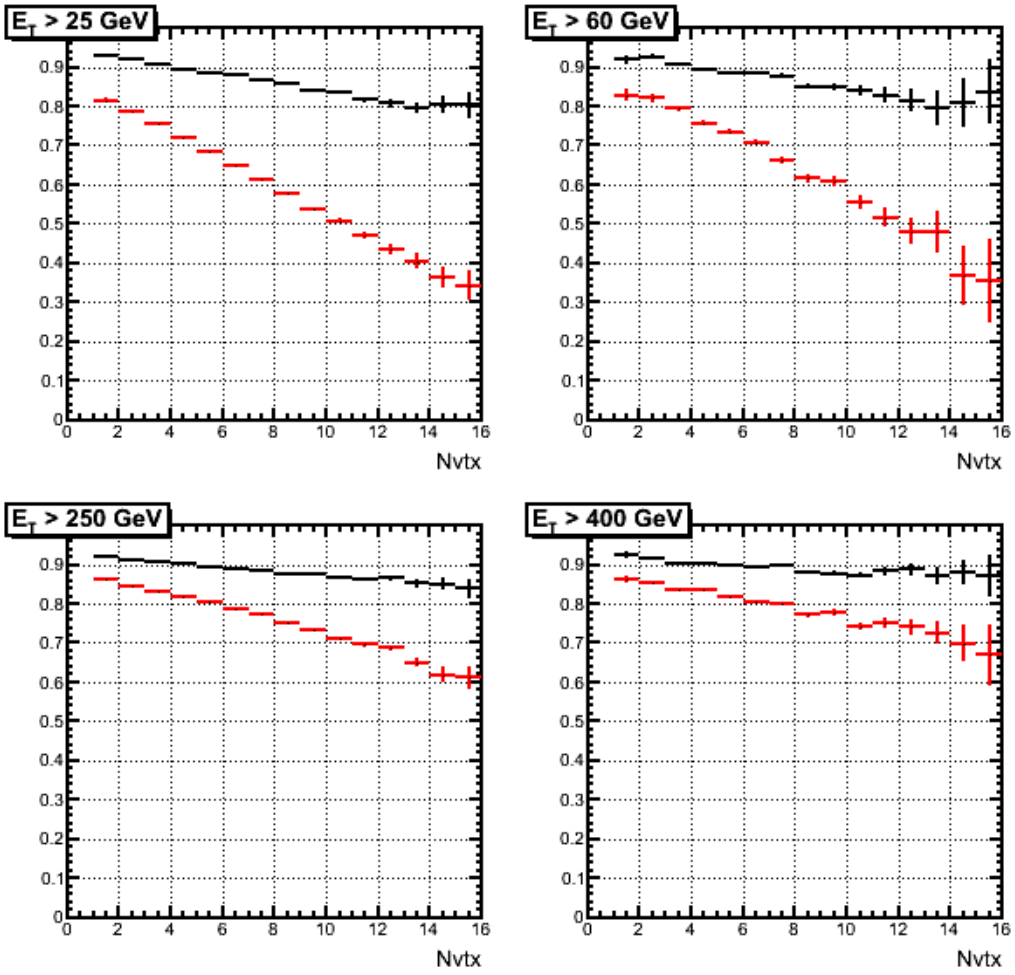

Figure 5.4: Photon ID efficiency dependence on the number of reconstructed pileup vertices, N_{vtx}. Black points are for "tight" ID, Red points are for an illustrative supertight ID selection

5.3 Kinematics

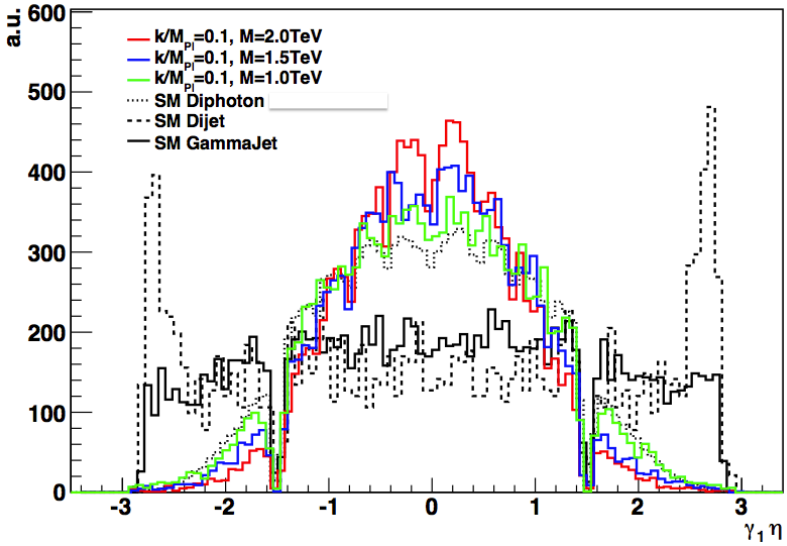

Figure 5.5: η distribution of background and signal. The dips at $|\eta| = 1.4442$ are due to the ECAL barrel and endcap boundaries.

Motivated by keeping a relative trigger efficiency of 100%, the p_T cuts are set at $p_T > 70\ GeV$ for both photons, leading to a corresponding $M_{\gamma\gamma}$ cut of $M_{\gamma\gamma} > 140\ GeV$. This has the added benefit of eliminating any contribution from $Z \rightarrow e^+e^-$ to the background control region. Additionally, as the range of excluded masses increases, the signal distribution in η becomes more and more central, to the point that there is less than 5% expected signal to be gained from the inclusion of endcap photons (Figure 5.5). This, coupled with the poor endcap resolution, and the desire to synchronize the selection to allow interpretation in the ADD scenario, suggested that the analysis be limited to barrel photons ($|\eta_{det}| < 1.4442$).

5.4 K-factors

In the high mass signal region, there are negligible contributions from reducible, jet misidentification backgrounds, thus the key MC simulation inputs are the simulation of true diphoton background and the RS graviton signals. Each of these simulation samples was generated with PYTHIA [31], calculated at leading order (LO). To improve the knowledge of these cross sections, we computed k-factors, which are the ratio of next-to-leading order (NLO) to LO predictions for each process, as a function of the mass (both signal and background) and $\tilde{k}$ (signal only).

For the signal, we use recently calculated k-factors [32], which range from 1.55 to 1.73 (Figure 5.6).

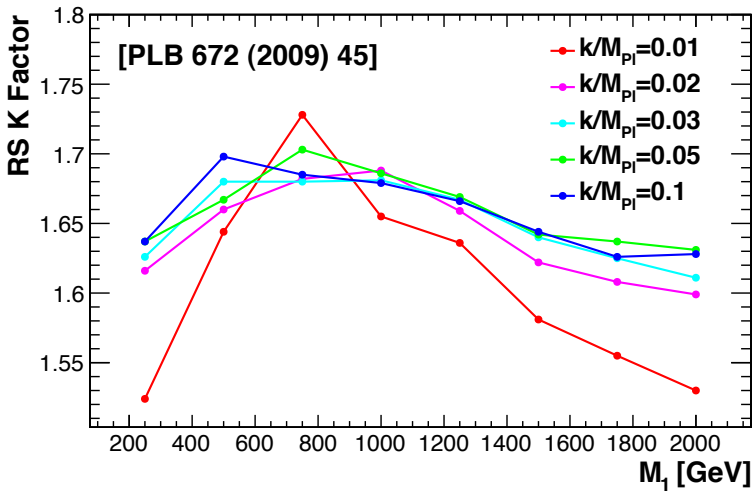

Figure 5.6: Ratios of NLO and LO cross sections, and corresponding k-factors for SM diphoton production

For background, the (NLO) prediction is calculated with the DIPHOX+ GAMMA2MC [33, 34] generators, which take into account the fragmentation processes in which the photons can come from the collinear fragmentations of hard partons. A separate analysis by CMS has also demonstrated good agreement with the NLO prediction at low mass, in the region $M_{\gamma\gamma} < 300\ GeV$ [35]. The sub-leading-order gluon-fusion box diagram is included as a part of the PYTHIA calculation because of its large contribution at the LHC energy, although its effects are small at high $M_{\gamma\gamma}$. The K factor varies between 1.7 and 1.1 from low to high $M_{\gamma\gamma}$. A systematic uncertainty of 7% on the value of

the K factor is determined by examining the PDF uncertainties and variation of the renormalization and factorization scales. The background calculations are discussed in more detail in Section 6.1.

5.5 Signal Samples and Resonance Width

The RS graviton signal samples are simulated using PYTHIA [31], in steps of 250 GeV, for three values of $\tilde{k} = 0.01$, 0.05, and 0.10 (Table 5.2).

$\tilde{k}$	M_1	cross section (pb)
0.01	250	1.652
	500	0.05779
	750	0.006354
	1000	0.0011635
	1250	0.0002832
	1500	0.00007992
0.05	500	1.444
	750	0.1596
	1000	0.0294
	1250	0.007123
	1500	0.002006
	1750	0.0006297
0.1	750	0.6346
	1000	0.1164
	1250	0.02767
	1500	0.007935
	1750	0.002500
	2000	0.0008492

Table 5.2: MC signal samples

In the search, a fixed window is selected around each M_1 mass point of interest. Because the signal shapes deviate from Gaussian distributions, we define an effective measure of the signal width σ_{eff} as the half-width of the narrowest mass interval containing 68% of the signal from simulation (Figure 5.7). A window is then formed around the central value of size $\pm 5\,\sigma_{\text{eff}}$ in the data. This window contains 96–97% of the signal acceptance for all mass points considered in this analysis. The detector resolution is negligible compared to the window size. This choice of the window max-

imizes the signal acceptance and analysis sensitivity in the case of small backgrounds.

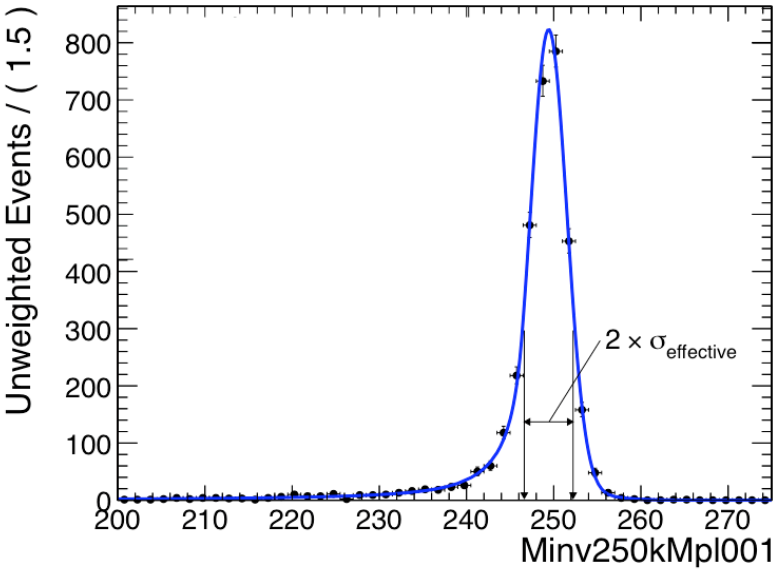

Figure 5.7: Graphical definition of σ_{eff}, for RS signal peak

Due to the high mass, and the correspondingly high p_T of each photon, the ID efficiency is relatively flat over the M_1 and $\tilde{k}$ parameter space. The main differences arise from the kinematics, which causes a narrowing in η space as a function of mass, and in the resonance width, which grows with the mass and also with the coupling as shown in Figures 5.8 and 5.9

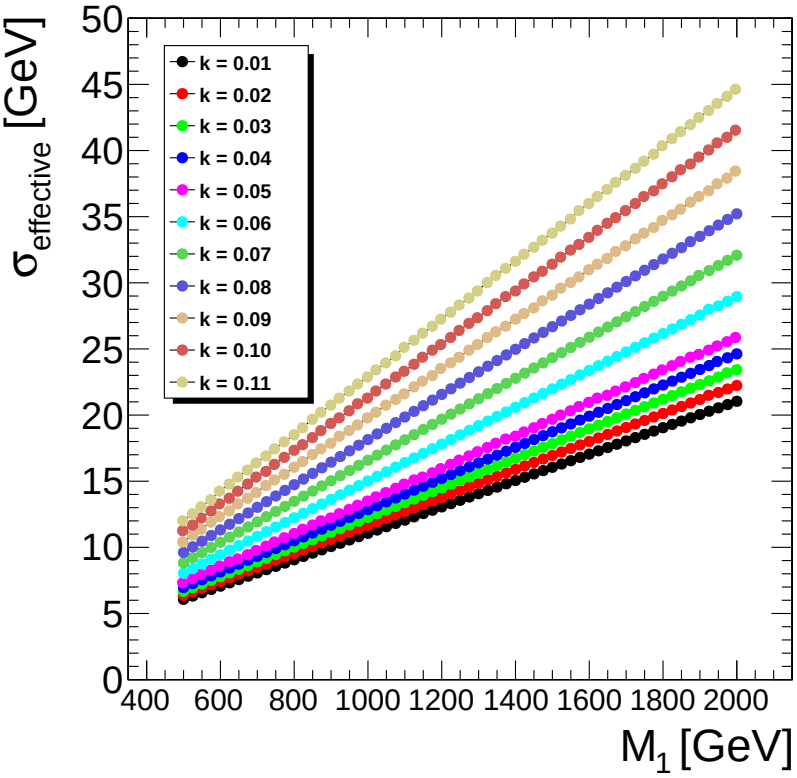

Figure 5.8: σ_{eff} for the RS graviton signal, as a function of resonance mass, for $\tilde{k}$=0.01–0.10.

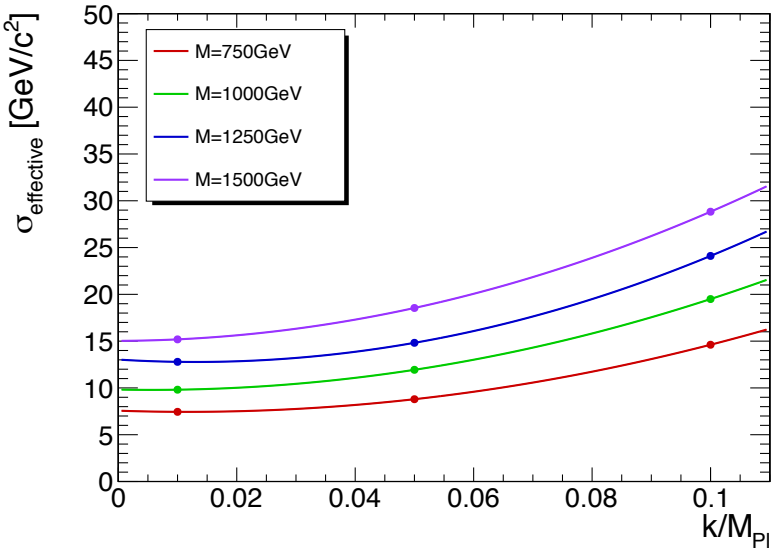

Figure 5.9: σ_{eff} for the RS graviton signal, as a function of $\tilde{k}$, for $M_1 = 750, 1000, 1250, 1500$ GeV

5.6 Efficiency and Acceptance

The signal efficiency is measured using the RS graviton MC simulation samples described in Section 5.5. The combined kinematic acceptance (applying cuts described in Section 5.3) and the efficiency of the photon identification (described in Section 5.2) are shown in Figure 5.10.

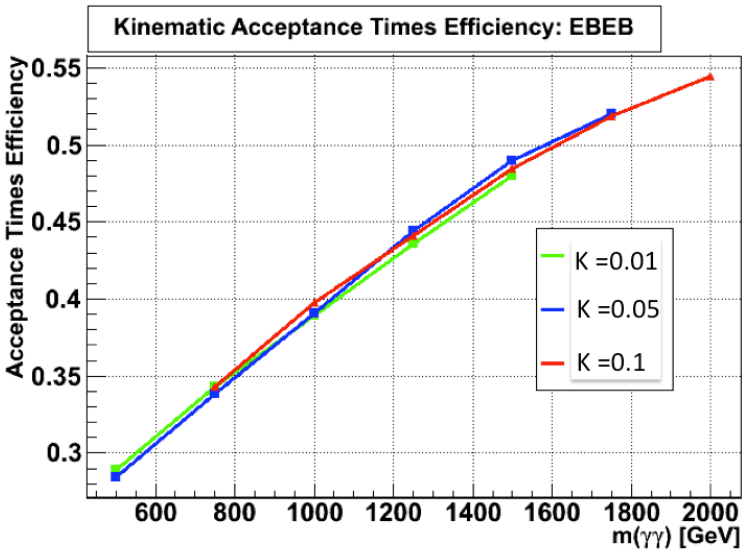

Figure 5.10: Kinematic acceptance times selection efficiency as a function of invariant mass, measured in signal MC samples.

The majority of the total efficiency is due to the kinematic acceptance as a function of M_1, as the photon identification efficiency was already shown to be relaltively flat in η and E_T in Section 5.2. The data-driven correction for MC efficiency, from Z decays as mentioned in Section 5.2, is also applied here. Note that there is no significant dependence on the coupling $\tilde{k}$, as the ID of the photons is entirely governed by the p_T spectrum which is in turn set by the mass, M_1. For those points outside of the generated values of $\tilde{k}$ and M_1, interpolations are performed for all of the corresponding efficiencies and acceptances.

Chapter 6

Backgrounds

Backgrounds fall into two categories:

Reducible Processes in which one or more jets is misidentified (misID) as a photon

- γ + Jet: one prompt photon and one jet misID
- Di-Jet: two jets misID as photons

Irreducible True diphoton processes, such as gluon fusion and quark annihilation

In the low mass control region, the reducible backgrounds are important, and are estimated in a data-driven way from related datasets. At higher mass, the contribution from jet backgrounds becomes negligible, and thus the background rate is driven by the selection rate and cross section of the irreducible backgrounds. There are no events in the related datasets in this high mass region, so this prediction relies on accurate simulation of the diphoton processes.

6.1 Monte Carlo simulation

The expected SM diphoton contributions are derived from MC simulations with PYTHIA. Contributions from Box (gluon fusion) and Born (quark annihilation) diagrams are included at LO (Figure 6.1).

To reduce the statistical uncertainty by sampling more at higher p_T, the samples are binned in p_T, as shown in Table 6.1:

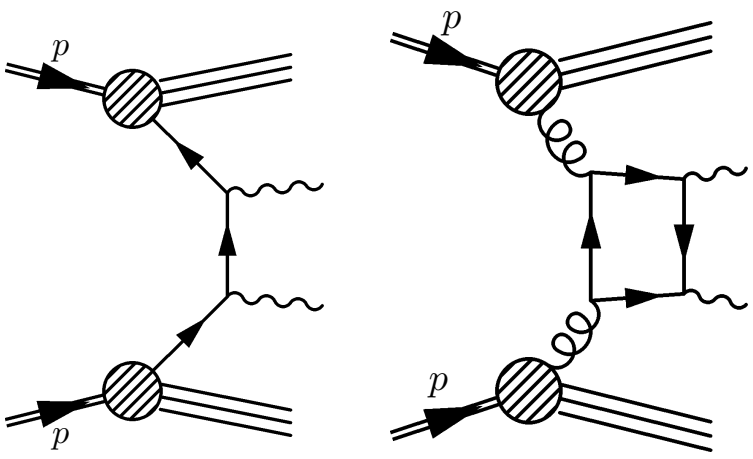

Figure 6.1: Diagrams for LO quark annihilation and gluon fusion processes [36].

Sample Name	p_T range	cross section (pb)
Born	10–25	236.4
	25–250	22.37
	250–∞	0.008072
Box	10–25	358.2
	25–250	12.37
	250–∞	0.000208

Table 6.1: MC background samples

Although convenient for computation and interfacing with CMS software, the PYTHIA calculation is not as accurate as needed, with higher order terms contributing nearly half that of the leading-order calculation [36]. To obtain the rates expected at NLO, a dedicated program DIPHOX [36] is used, and then K-factors (the ratios of NLO to LO) are computed as a function of $M_{\gamma\gamma}$ and applied to the PYTHIA simulation samples.

Here, the contributing diagrams are split into three categories:

The first is direct, where both photons are prompt (Figure 6.2).

Diagram a is the born process ($q\bar{q} \rightarrow \gamma\gamma$) already described, while diagrams b and c represent the leading NLO corrections of order $\mathcal{O}(\alpha_s)$.

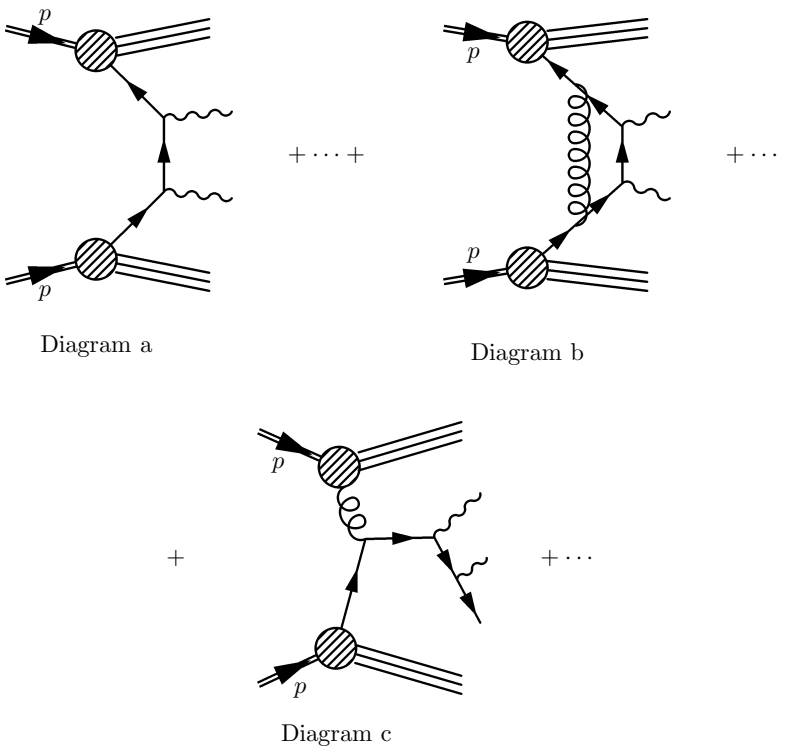

Figure 6.2: Direct production diagrams. A: Born process, the annihilation of quarks to two photons. B: virtual gluon correction to diagram A. C: radiative photons from quark/gluon interaction [36]

.

However, these also represent the leading-order terms for single fragmentation, where one photon is prompt and the other results from collinear fragmentation of a quark or gluon, such as diagram d (Figure 6.3).

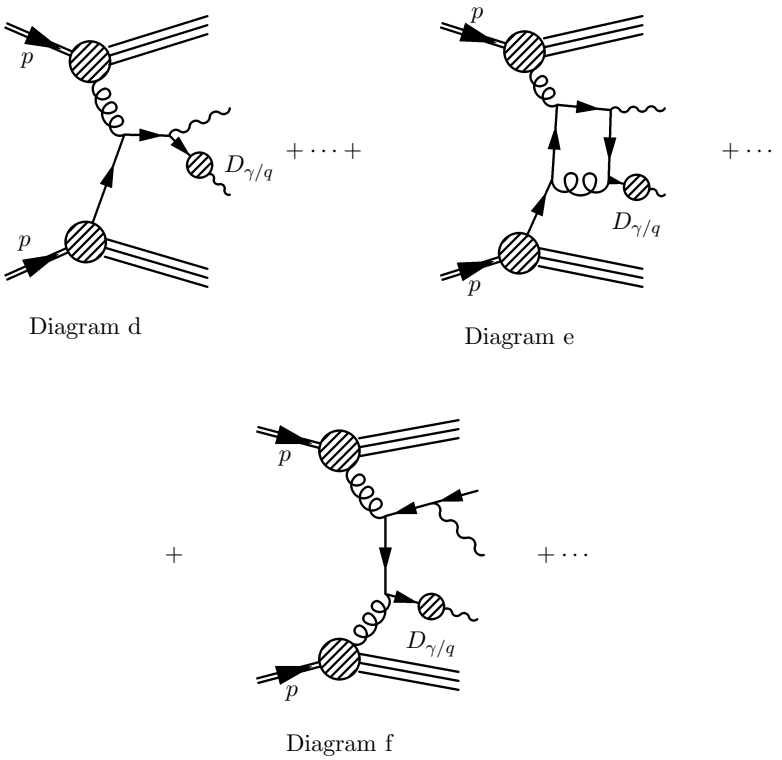

Figure 6.3: Single fragmentation diagrams. D: leading order fragmentation of a quark to photon. E: virtual gluon exchange correction to diagram D. F: same process replacing an initial state quark with a gluon [36].

The singularity from having a collinear parton and photon is factorized to all orders, and then absorbed into the fragmentation functions for quarks and gluons, $D_{\gamma/q \text{ or } g}$, which depend on the arbitrary choice of factorization scheme and factorization scale. [1] When the factorization scale is large compared to typical hadronic scales ($\sim$ 1GeV), these functions behave as $\sim \alpha/\alpha_s$, and thus contribute at the same orders as corresponding direct processes. Because of the high gluon-gluon luminosity

[1] A fundamental property of QCD theory is the ability to factorize the long- and short-distance contributions to any physical cross section involving larger momentum transfers. Although factorization provides a prescription for dealing with logarithmic signularities, there is remaining freedom in how the finite contributions are treated. How the finite contribution is factored out, whether to the quark distribution, or structure functions, or both define a 'factorization scheme'. The factorization scale refers to the choice of cutoff between what is considered long- and short-distance, and is usually set to the scale of the hard process.

of the LHC, additional processes starting with gq or $g\bar{q}$ states must be included as well (diagrams e, f).

This leads once again to leading-order terms for another process, double fragmentation, where both final state objects result from fragmentation (Figure 6.4)

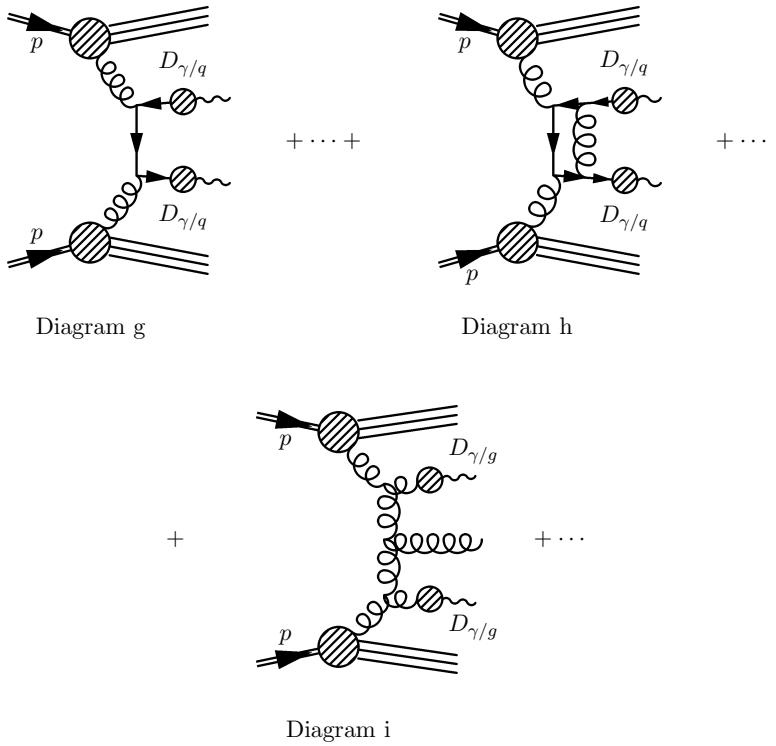

Figure 6.4: Double fragmentation diagrams [36].

and the corresponding NLO corrections to this process (diagrams h, i). Even though it is technically NNLO, the gluon fusion process is included because the high gluon luminosity nearly cancels the additional suppression by α_s.

The NLO cross sections are calculated with DIPHOX [36], a program dedicated to diphoton processes. DIPHOX includes all direct and fragmentation diagrams from LO to NLO, and is configured using the CTEQ6 Parton Density Function (PDF) [37]. To match the kinematics and isolation used at CMS, additional cuts are implemented as in Table 6.2.

The $|\eta|$ and p_T requirements correspond to the barrel detector, and the fully efficient plateau for trigger purposes, as explained in Section 5.2. The isolation cone is similarly matched to the selection requirements of this analysis, because although the differentiation of direct and fragmentation is arbitrary in the theory summation,

Parameter	Value
PDF	CTEQ6
$\|\eta\|$	< 1.4442
p_T	$> 70GeV$
Isolation Cone Radius	0.4

Table 6.2: DIPHOX parameters for MC simulation

selection on part of the isolation phase space will necessarily have different impacts on direct/fragmentation objects.

Figure 6.5 shows the NLO and LO cross sections, as well as the corresponding K-factors.

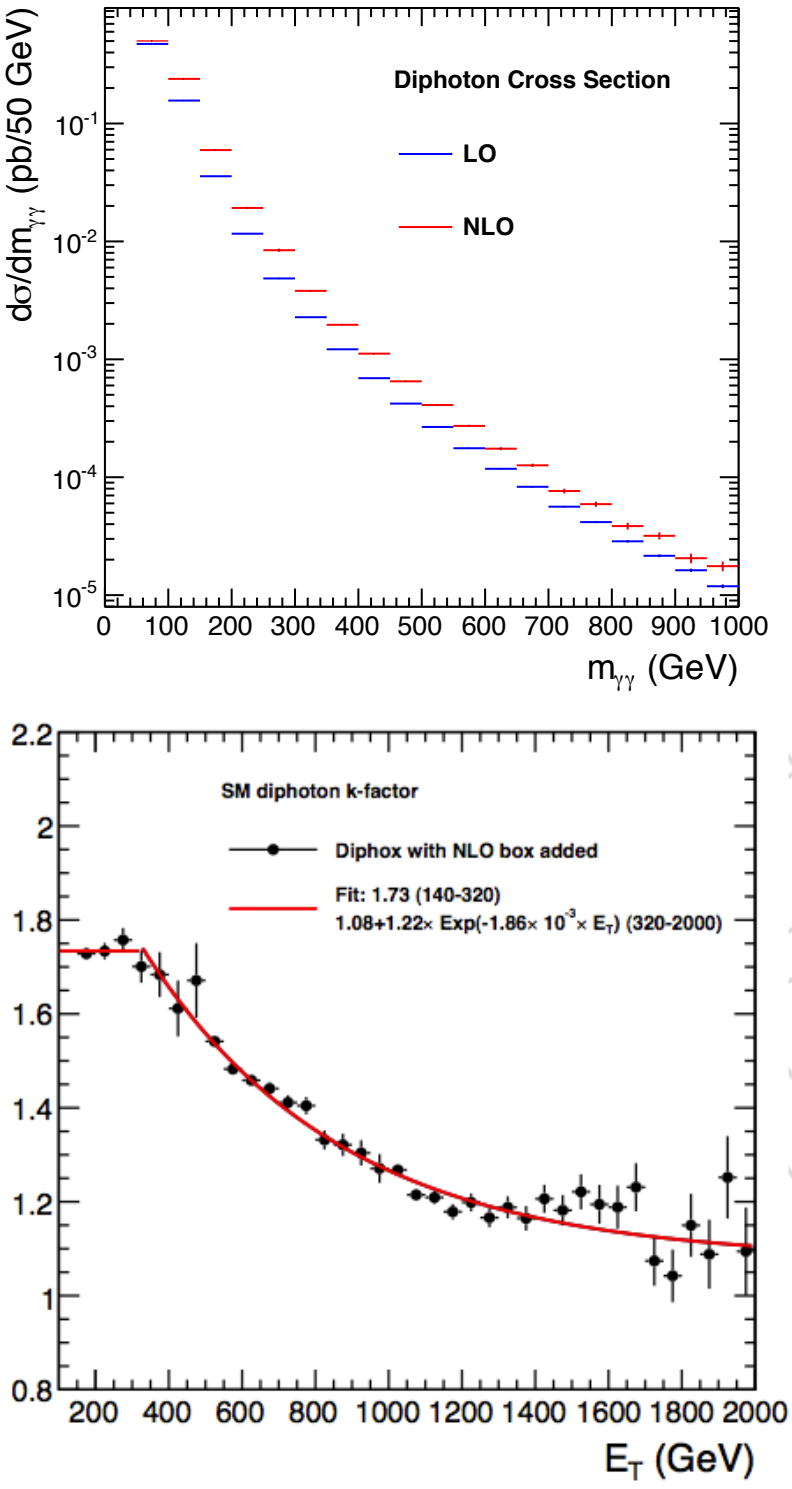

Figure 6.5: (Top) plot of the LO cross section, from PYTHIA, and the NLO cross section, from DIPHOX. The ratio of these forms the k-factor for SM diphon production (Bottom). Note that the bottom plot starts at $M_{\gamma\gamma} = 140$ to correspond with the kinematic selection, $p_T > 70$. The k-factor is parametrized as a constant function at low mass (140-320), joined with an exponential function at high mass (320-2000).

The systematics uncertainties are estimated by changing the PDF to MSTW [38], which leads to a maximum variation of 7% in the k-factor. The choice of factorization scales changes the composition of direct, single-fragmentation, and double-fragmentation monotonically, but has a minimal effect on the physically observable total cross section [36] and is not added as an additional uncertainty.

6.2 Data-Driven Misidentification Rate

The overall goal of a misidentification or "fake" rate method, is to measure the rate of jet misidentification which leads to background events in the signal selection. There is a dual dichotomy present in this case (Figure 6.6), first because the signal selection will contain contributions from real prompt photons as well as misidentified jets, and second because the two objects selected in each event can be (mis)identified independently.

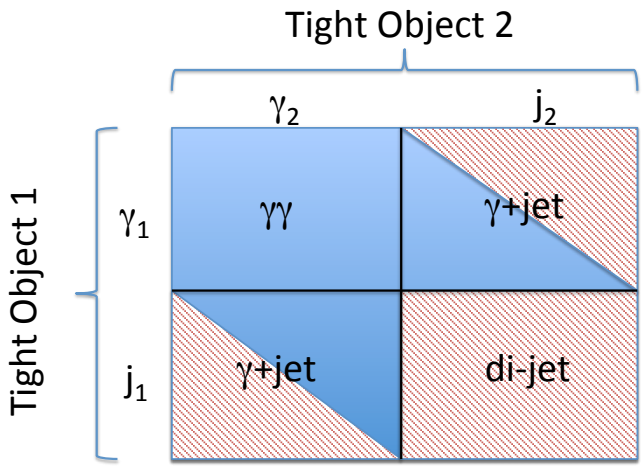

Figure 6.6: Breakdown of signal sample composition

The background prediction therefore consists of contributions from $\gamma\gamma$, γ+jet, and di-jet. In the lower mass region, each of these gives a significant contribution, while at high masses, the contribution from jet-related processes is negligible compared to

the diphoton processes. Therefore, the high mass background prediction is made with MC simulation, including NLO terms, of SM diphoton processes.

$$\begin{cases} \gamma\gamma & \text{use MC} \\ \gamma + jet, di - jet & \text{estimate from data sidebands} \end{cases} \tag{6.1}$$

To validate the MC predictions, the other contributions in the low mass region are estimated from data sidebands. Comparison of the sum of these contributions and the observed data give an indication of the agreement. Here, sidebands will refer to a selection which is orthogonal to the signal sample, but related to and predictive of the rate in the signal sample.

The sideband choice in this case will be a "loose" selection, with relaxed ID requirements relative to the "tight" signal selection defined in Section 5.2. An explicit inversion of at least one of the requirements ensures orthogonality of the two selections. The quantity which will relate the sideband and signal regions is the ratio between the tight and loose selections, for misidentified jets.

$$T_{selection} = r \cdot L_{selection} \tag{6.2}$$

The first assumption is that loose ID and tight ID applied to jets will select mutually exclusive subsets of the phase space of how fragmentation and hadronization of quarks/gluons occurs (Figure 6.7).

This is satisfied by the explicit orthogonality in the choice of "loose" selection, as well as the gap between the two selections to remove any leakage of events from one type to another. Now, this ratio of jets passing tight selection to jets passing loose selection is exactly the misidentification rate. However, this cannot be measured immediately in data, because even the jet-triggered datasets will contain events with other particles, such as electrons, muons, and in particular, photons (Figure 6.8).

The contributions from electrons, muons, and other particles can be eliminated by veto selection in the tracker (pixel veto), and HCAL or muon system selections. By

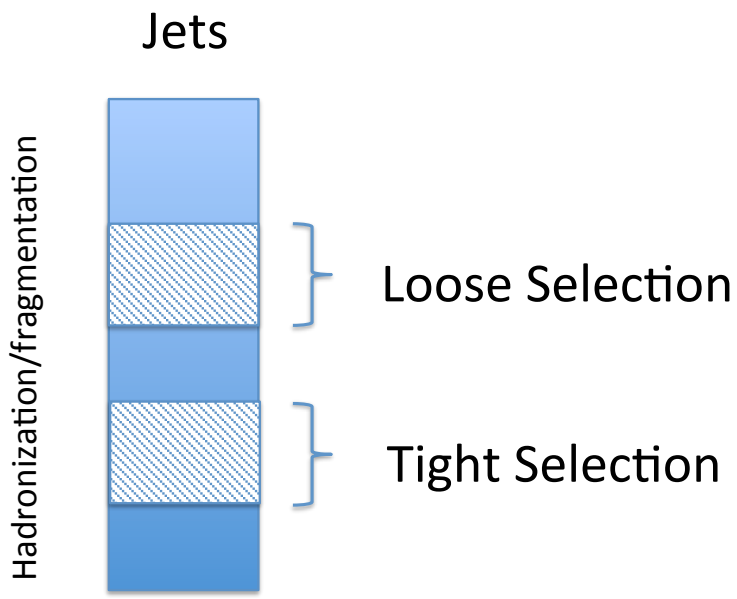

Figure 6.7: Cartoon of jet fragmentation and selection ID relationship

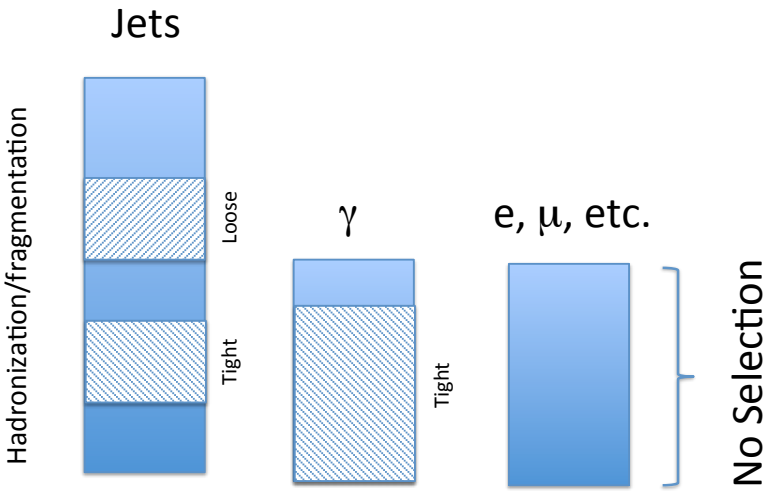

Figure 6.8: Cartoon of particle composition in data sets

design, the loose selection picks only contributions from jets, and so the denominator of the ratio is satisfied. The tight selection, however, picks contributions both from jets, and from photons, and thus a strick ratio of tight ID objects to loose ID objects will depend on the photon content of the particular dataset. Clearly, this would not be transferrable from a jet-triggered dataset to a Photon triggered dataset. A solution is to use an additional method to estimate the photon contribution to the tight ID

objects, and thereby remove it from the calculation. The following is the procedure for the entire method:

Events which contain at least two of these Tight or Loose photons (with the same minimum p_T cut applied to all objects) are partitioned into signal and background samples, as follows:

- Tight-Tight, which is our data signal sample
- Tight-Loose, where one of the objects is a tight ID object, but the other is a loose ID object
- Loose-Loose, where both objects in the event are loose ID objects.

This partitioning is mutually exclusive, based on assigning priority to events with two tight objects, then events with one tight object, and finally events with no tight objects.

If our signal region were also low mass, then this procedure would be complete, and the background would be estimated by taking the Loose-Loose sample and applying the ratio, r, twice. However, for the high mass region, even the sideband LL would be unpopulated, and thus the prediction

$$TT_{predicted} = r^2 \cdot LL_{observed} = 0 \tag{6.3}$$

would not contribute any information.

As outlined earlier, the sidebands are instead used to predict the non-photon parts of the background at lower mass, and consequently validate the MC prediction for diphoton background, which can then be trusted in the higher mass region. Therefore, the ratio r, is modified to measure only the fraction of misidentified jets implied in the tight selection.

$$r_{fake} = r \cdot f_{jet} = r \cdot (1 - f_{\gamma}) \tag{6.4}$$

where f_{jet} is the fraction of jets in the tight selection, and f_γ is the complimentary fraction of photons in the same tight selection. These fractions are dependent on the triggering, and kinematic requirements of each particular dataset, and are calculated separately in each case.

Remember that a tight object is not equivalent to a true photon, as the tight selection will still contain some fraction of misidentified jets. We do however have a correspondence between the loose objects and misidentified jets by construction, using sidebands of isolation variables where there is no signal leakage from true photons.

The purity of each Tight object selection in terms of percentage of real photons can be determined by the template fitting method [39]. A variable which is discriminant between two processes, in this case direct photons and misidentified jets, is used to form templates of the signal and background. The shower shape variable $\sigma_{\eta_i\eta_i}$ is a powerful discriminant for prompt photons, and thus a good choice for a template. For each photon E_T bin, the data are fit with $f(\sigma_{i\eta i\eta}) = N_S S(\sigma_{i\eta i\eta}) + N_B B(\sigma_{i\eta i\eta})$, where N_S and N_B are the estimated number of signal and background events in the bin. The fit is performed using a binned extended maximum likelihood, minimizing

$$\mathcal{L} = -\ln L = -(N_S + N_B) + \sum_{i=1}^{n} N_i ln(N_S S_i + N_B B_i), \tag{6.5}$$

where N_i, S_i, and B_i are the observed events, and corresponding signal and background components, and the sum is over the range of $\sigma_{i\eta i\eta}$ values. The template fitting method can only yield the likely composition of a sample as a whole, but does not sort individual events into the two classes.

The signal templates could be derived from direct photons in $W\gamma$ and $Z\gamma$ processes, where the selection, and kinematic reconstruction of the vector boson provide a high purity sample of photons from the data. However, we are limited in statistics, and would be restricted to lower p_T photons than our region of interest. The signal templates are therefore derived from MC photon samples (blue lines in Figure 6.9). There is no lack of statistics nor need for a specific jet process and thus the background templates (green lines in Figure 6.9) are formed by inverting the track

isolation requirement:

$$2.0GeV + 0.001 \cdot p_T < Iso_{TRK}(0.04 < \Delta R < 0.4) < 3.5GeV + 0.001 \cdot p_T. \quad (6.6)$$

Any data based selection of background template must necessarily be distinct from the data selection of interest. This choice of background template exploits the lack of correlation between the track isolation, and the $\sigma_{i\eta i\eta}$ variables to minimize systematic differences between the background template, and the background distribution in data. The inversion of track isolation has an upper limit, to further limit possible variations due to differences in the track isolation in signal and background samples.

The results of the template fits (Figure 6.9), and the corresponding purity (% γ) (Figure 6.10), are combined with the Tight/Loose ratio to yield the final fake rate, $r_{Fake} = n_{Fake}/n_{Loose}$, in several bins of p_T .

The fake rates are then parametrized as a function of p_T:

$$FR = p_0 + p_1/x^{p_2}. \quad (6.7)$$

The fake rates (Figure 6.11) are measured on samples from several photon triggers, as well as jet and muon triggers to quantify the trigger dependence and universality of the ratio in Equation 6.2. The variation with respect to the parametrization is covered by a systematic uncertainty of 20%, by examining the variation in photon triggers on Figure 6.11, and this systematic is indicated by the dashed red lines.

The events containing Loose objects are then weighted by the fake rate function evaluated at the p_T of the Loose object. In the case of Loose-Loose, the event weight is the product of the two weights coming from both Loose objects. The Tight-Loose and Loose-Loose samples are then combined to obtain a data-based background prediction for the contribution of fake photons to the diphoton final state, which estimates the sum of the γ+jet and dijet backgrounds.

A subtlety arises because the Tight selection contains both prompt photons and jet misIDs, while the Fake rate applied to the Loose selection gives only the yield of

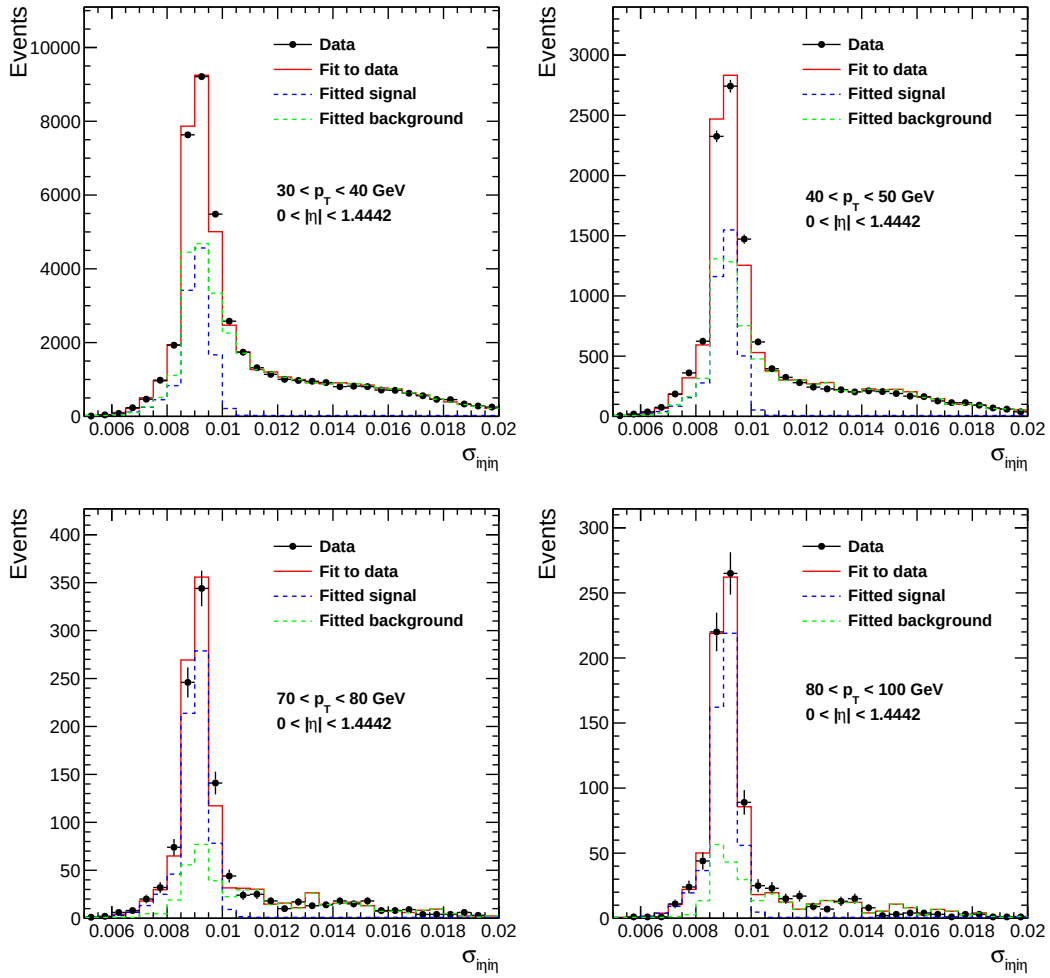

Figure 6.9: $\sigma_{i\eta i\eta}$ template fits, in exclusive bins of p_T , in Jet trigger dataset. Note the sharper peak due to the photon template (blue lines), and the long tail for misidentified jets (green lines). The combined fit is shown in red, and the corresponding fractions are derived from the fit.

jet misID. Simple summation and application of the fake rate to the TL, LT, and LL samples would actually overcount the fake-fake contribution. Our desired quantity, the number of events in the TT sample, contains contributions from dijet, diphoton, and photon/jet (counted twice for p_T ordering):

$$TT = (j + \gamma) * (j + \gamma) = jj + j\gamma + \gamma j + \gamma\gamma, \tag{6.8}$$

where T represents an object passing tight selection, and j, γ represent real jets and photons that are counted in this selection.

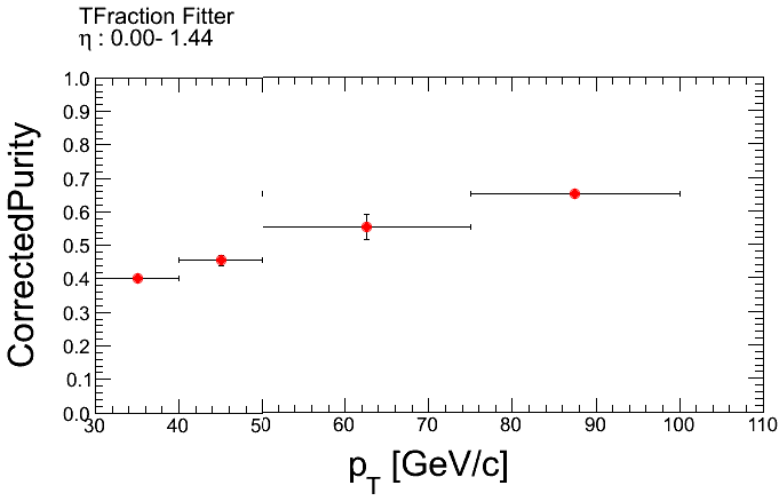

Figure 6.10: Corresponding Purity from TFraction Fitter

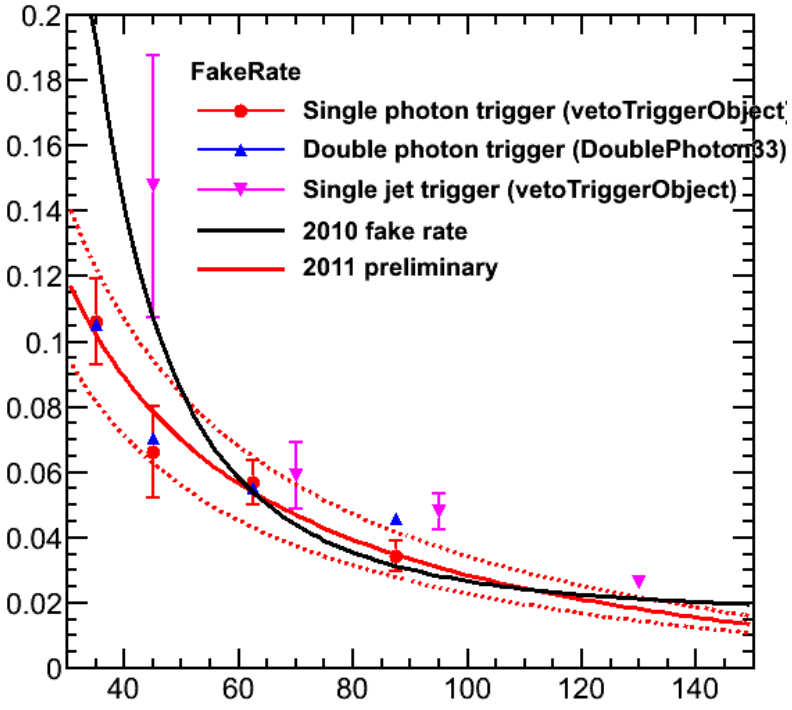

Figure 6.11: Fake rate and parameterized fit function.

The contribution from real-real diphotons is obtained from the diphoton MC as described earlier, and needs to be added to the fake contributions to give the total background estimate for the final state.

The breakdown of the data driven background samples is as follows:

$$TL = (j + \gamma) * (j) = jj + \gamma j, \tag{6.9}$$

$$LT = (j) * (j + \gamma) = jj + j\gamma, \tag{6.10}$$

$$LL = (j) * (j) = jj, \tag{6.11}$$

where L represents an object passing the loose selection, which is assumed to be composed only of real jets and no photons, so that the total contribution from the TL and LT samples overcounts the di-jet contribution by a factor of 2. Therefore, subtraction of the contribution from the LL sample leads to the correct relation:

$$TT = \gamma\gamma + TL + LT - LL. \tag{6.12}$$

It is also possible to derive the contribution from photon+jet algrebraically, for comparison with MC.

$$j\gamma + \gamma j = TL + LT - 2 * LL. \tag{6.13}$$

6.2.1 Systematic Uncertainty on Fake Rate

The propagation of the 20% systematic on the fake rate needs carefull treatment. The first important point is that this uncertainty must be calculated bin by bin, as it is not an overall scale factor, and the fraction of Loose-Loose and Loose-Tight is not constant in different kinematic ranges. The second point is whether or not the systematic is treated as correlated between points at different p_T . Each appearance of a Loose object, L, in equation 6.2 carries with it one factor of the systematic uncertainty, and the LL term would carry either 40% (fully correlated) or 28% (fully uncorrelated, added in quadrature). Normally, the conservative way to propagate

errors is to assume maximal correlation, but the minus sign from the algebra actually reduces the total uncertainty in this case. Thus, to be safe, the systematic is treated as uncorrelated between different p_T points, and thus the TL (LT) and LL uncertainties add in quadrature, properly weighted in each bin, e.g.,

$$\delta^2_{totalfake} = \delta^2_{TL/LT} + \delta^2_{LL}, \tag{6.14}$$

where $\delta^2_{totalfake}$ is the systematic uncertaint on the non-diphoton part of the background, and $\delta_{TL/LT}$ and δ_{LL} are the uncertainties on the TL (LT) and LL sideband estimates. In terms of the estimated numbers from each sideband, this would be:

$$\delta^2_{totalfake} = (0.2TL)^2 + (0.2 \times \sqrt{2}LL)^2, \tag{6.15}$$

and as a concrete example, assume there were 200 estimated events from the TL (LT) sideband, and 100 from the LL sideband, then the systematic uncertainty on each would be: $\delta_{TL/LT} = 0.2 \times 200 = 40$, and $\delta_{LL} = 0.2 \times \sqrt{2} \times 100 = 28$, while the total uncertainty would be $\sqrt{40^2 + 28^2} = 49$ events.

Chapter 7

Results

The data are in agreement with the background predictions from the fake rate method and diphoton MC + K-factors, as seen is Figure 7.1 and Table 7.1.

In each bin, the observed number of events agrees with the total background prediction within the uncertainty. The uncertainties include both the systematics, discussed in Chapter 6, and statistical uncertainty, though in most of the cases besides the dijet bins, it is the systematic uncertainties that dominate. The slight excess (two events) around $M_{\gamma\gamma} = 600$ GeV is not highly significant, corresponding to 1.2σ, and would not be compatible with an RS signal (see Chapter 5 for the cross section for such a value of M_1).

Process	Diphoton Invariant Mass Range [TeV]			
	[0.14, 0.2]	[0.2, 0.5]	[0.5, 0.9]	> 0.9
Multijet	15 $\pm$ 6	17 $\pm$ 7	0.2 $\pm$ 0.1	0.003 $\pm$ 0.001
$\gamma +$ jet	102 $\pm$ 15	124 $\pm$ 18	2.5 $\pm$ 0.4	0.19 $\pm$ 0.04
Diphoton	372 $\pm$ 70	414 $\pm$ 78	16.9 $\pm$ 3.2	1.3 $\pm$ 0.3
Backgrounds	489 $\pm$ 73	555 $\pm$ 81	19.6 $\pm$ 3.2	1.5 $\pm$ 0.3
Observed	484	517	16	2

Table 7.1: Observed event yields and background expectations for different reconstructed diphoton invariant-mass ranges. Full systematic uncertainties are included (see Section 6.2.1).

Additional control plots also show good agreement between data and the predicted backgrounds in the control region. No sign of an excess of events is observed in the signal region; therefore, exclusion limits are set using a Bayesian method [40].

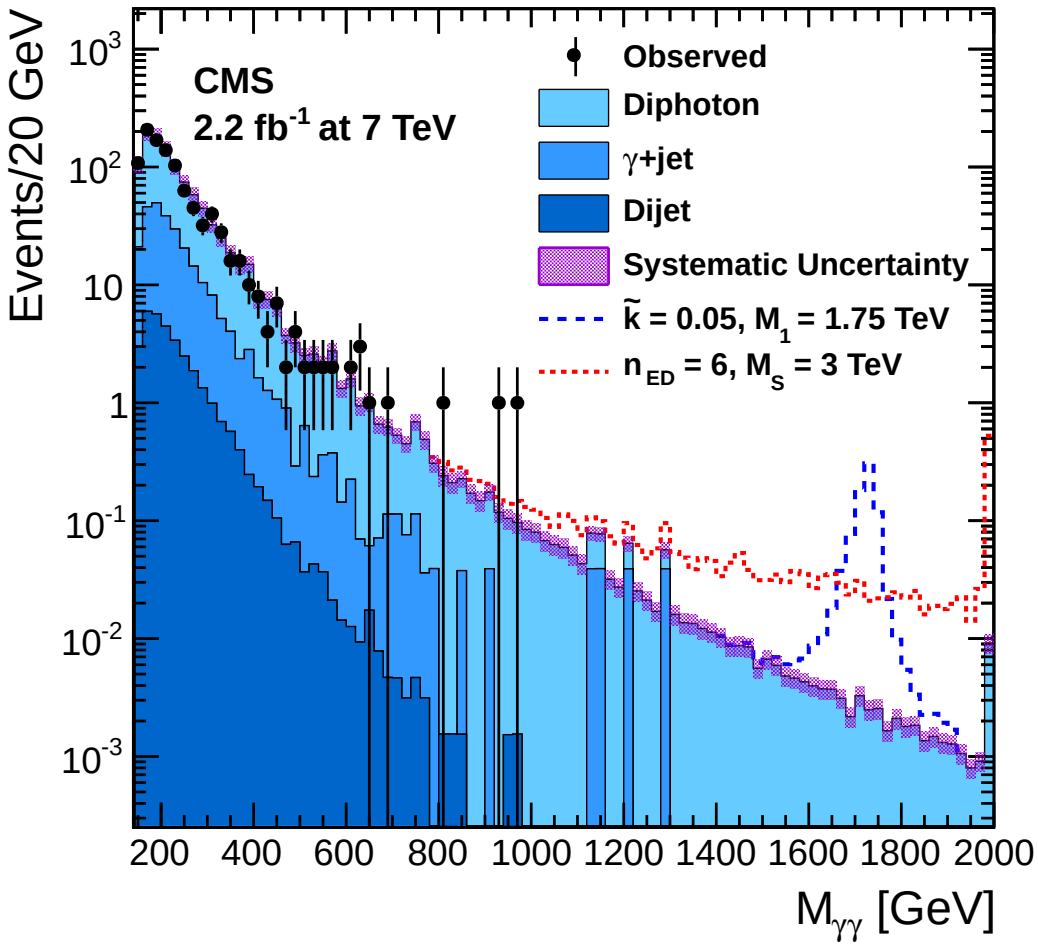

Figure 7.1: Observed event yields (points with error bars) and background expectations (filled solid histograms) as a function of the diphoton invariant mass. Photons are required to be isolated, with $E_T > 70$ $GeV$and $|\eta| < 1.4442$, corresponding to the ECAL barrel region. The shaded band around the background estimation corresponds to the systematic uncertainty. The last bin includes the sum of all contributions for $M_{\gamma\gamma} > 2.0$ TeV. The simulated distributions for two, non-excluded signal hypotheses are shown for comparison as dotted and dashed lines.

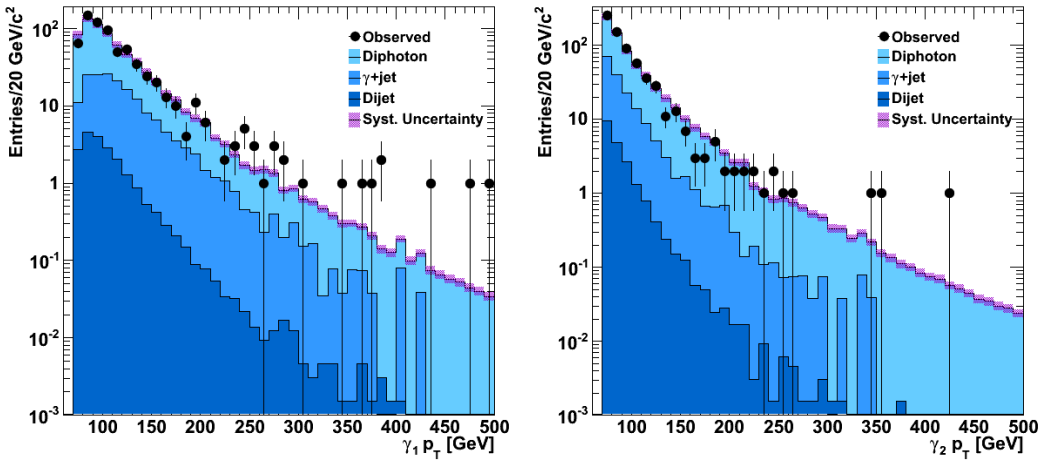

Figure 7.2: p_T of the leading (highest p_T) and subleading photons

In Figure 7.2, the predicted and observed p_T spectrum are in agreement and show a monotonically decreasing behavior. The slight excess in the leading photon spectrum near 350 GeV corresponds to a single event, and is an artifact of the bin size and low occupancy.

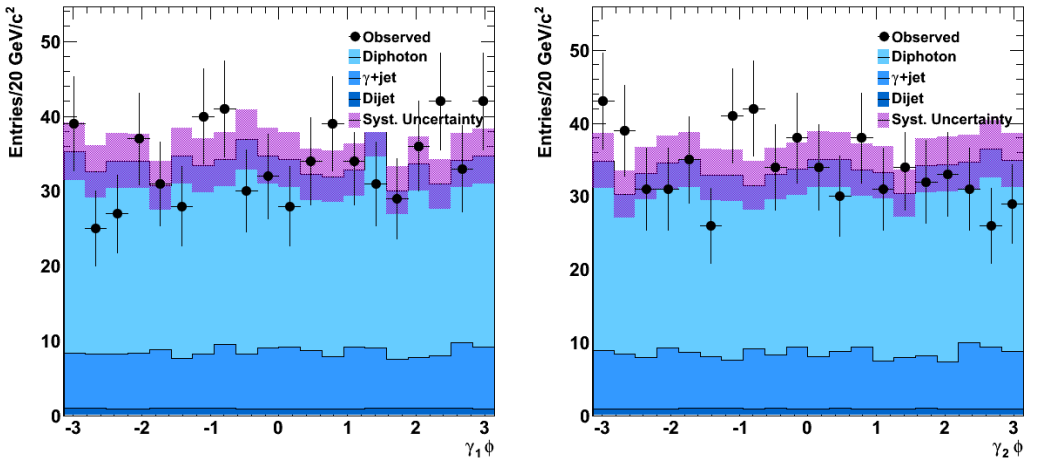

Figure 7.3: ϕ of the leading and subleading photons

The predicted and observed ϕ distributions are also in agreement, and are also compatible with a uniform distribution (Figure 7.3) as expected.

The η distributions are also in agreement, with the sharp cutoffs corresponding to the fiducial region used in the analysis (Figure 7.4).

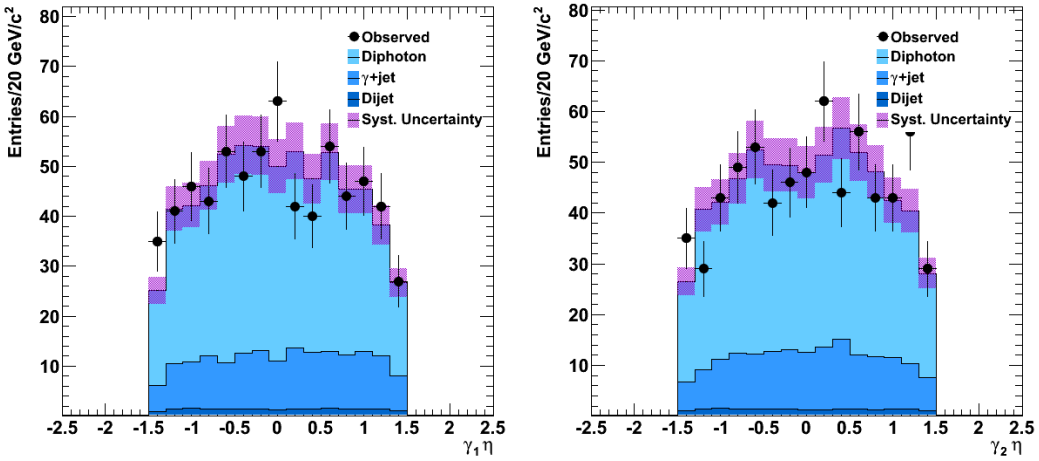

Figure 7.4: η of the leading and subleading photons. The selection restricts photons to the ECAL barrel ($|\eta| < 1.4442$)

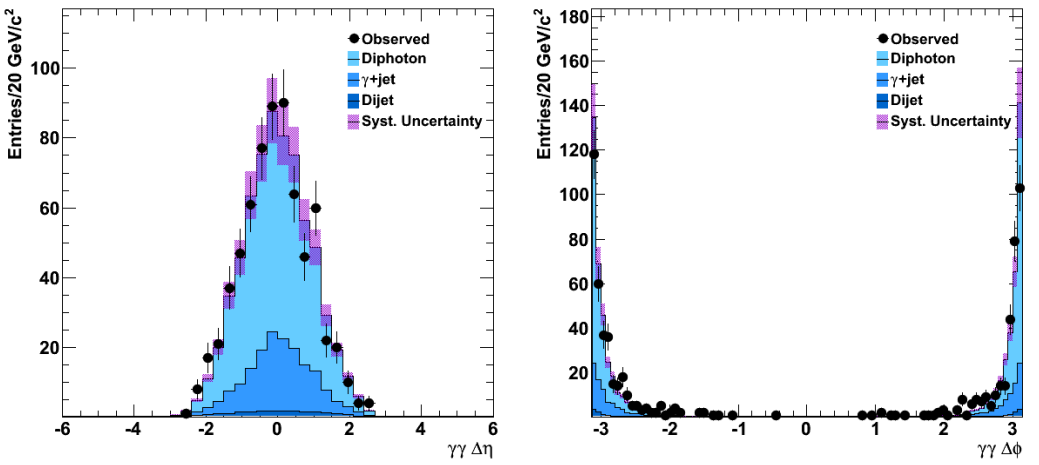

Figure 7.5: $\Delta\eta$ and $\Delta\phi$ between the leading and subleading photons. The beam halo peak at $\Delta\phi = 0$ has been vetoed.

In Figure 7.5 the $\Delta\eta$ is restricted to $\sim (-2.88, 2.88)$ due to the restriction of $|\eta| < 1.442$, while the $\Delta\phi$ distribution is in agreement with the observed data after the beam halo veto is applied. For the effect from beam halo, compare to Figure 3.5 in the prior discussion of beam background.

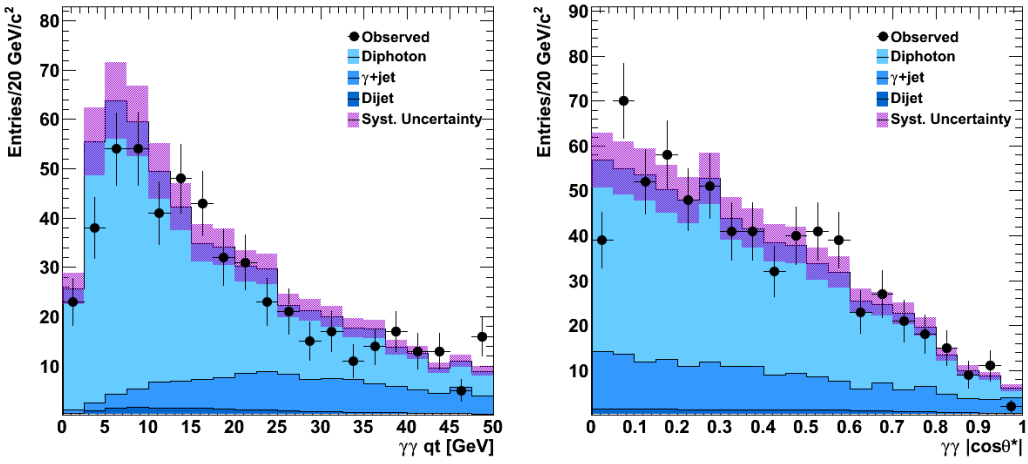

Figure 7.6: Diphoton transverse momentum and $cos(\theta^*)$, where θ^* is the angle relative to the z-axis in the Collins-Soper center of mass frame (see Figure 7.7).

The diphoton transverse momentum shows a low momentum distribution for the diphoton prediction, as the energy reconstruction for photons is quite good (see Section 3.1) and thus any non-zero transverse momentum comes from radiative processes in higher order diagrams. Compare this to the backgrounds with misidentified jets, where the momentum balance applies to the jet-photon or jet-jet system, but only the Electromagnetic fraction of the jet energy is reconstructed, which can lead to an imbalance in the total reconstructed momentum when treated as a diphoton event. The predictions for the jet misidentification backgrounds show a harder total momentum distribution for the photons, as some of the particles that carry the balancing transverse momentum may not be included in the jet which is mistaken for a photon. The variable $|cos(\theta^*)| = |P_1 - P_2|/P_{diphoton}$ falls from a maximum at zero, corresponding once again to perfect momentum balance of the photons, with a tail corresponding to some amount of non-zero total momentum for the diphoton pair (Figure 7.6). The geometrical interpretation of $cos(\theta^*)$ comes from some flexibility in the choice of axes

for a diphoton rest frame. Here, we use the Collins-Soper rest frame [41], characterized by a z-axis which cuts the angle between the proton momenta in half, with the boost from the diphoton q_T defining the two other orthogonal directions x, and y. The angle θ^* is defined between either photon and the z-axis in the Collins-Soper frame (Figure 7.7)

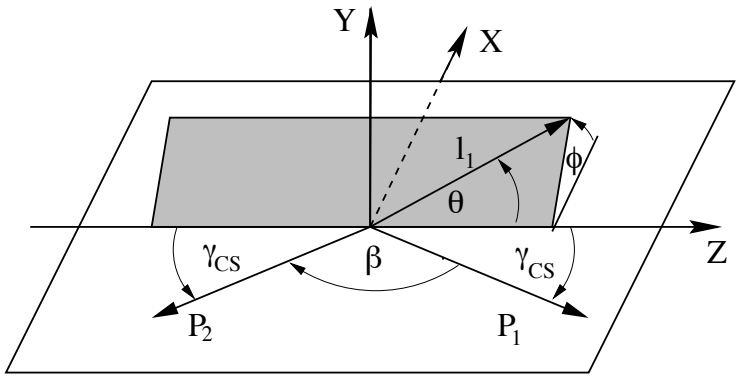

Figure 7.7: Diagram of the Collins-Soper frame, a rest frame of the diphoton system with axes chosen such that the z-axis bisects the angle between colliding proton momenta, P_1 and P_2. The bisected angle is also know as the Collins-Soper angle, γ_{CS}. l_1 is the momentum of the leading photon, and thus defines θ^* relative to the z-axis.

7.1 Cross Section Limits

A Bayesian approach is used to set limits on the RS graviton production cross section as a function of mass [40]. As a review [42], suppose there is a parameter of interest, σ, a vector of nuissance parameters θ, and a vector of observables x. In our case, σ would be the cross section for graviton production and decay in the diphoton mode, θ would include uncertainties on the luminosity, ID efficiency, kinematic acceptance, background prediction, and anything else which affects the measurement of σ but has an uncertain value. The observable is the number of events in the $M_{\gamma\gamma}$ spectrum, in a given window. Bayes' theorem [43] relates these quantities through the posterior density $P(\sigma, \theta|x)$, the prior density, $\pi(\sigma, \theta)$, and the model density $P(x|\sigma, \theta)$:

$$P(\sigma, \theta|x) = \frac{P(x|\sigma, \theta)\pi(\sigma, \theta)}{\iint P(x|\sigma', \theta')\pi(\sigma', \theta')\mathrm{d}\theta'\mathrm{d}\sigma'}. \tag{7.1}$$

The integral over the nuissance parameters is performed, leading to the posterior density, $L(\sigma)$ as a function of σ. An upper limit on the cross section is found by integration:

$$CL = \int_0^{\sigma} L(\sigma|x)\mathrm{d}\sigma. \tag{7.2}$$

Since the observable is an integer n, the number of events observed in data, the model density is chosen as the Poisson likelihood of observing n events, given an expectation of $(S + B)$, which depends on the backgrounds, signal cross section, signal efficiencies, and the luminosity:

$$P(n|S, B, \epsilon, L) = e^{-(B+S\epsilon L)}\frac{(B + S\epsilon L)^n}{n!}. \tag{7.3}$$

A flat prior is chosen for the cross section, while log-normal distributions are used for the nuissance parameters, since they are positive by definition (luminosity, efficiency, etc.) The associated systematic uncertainties are listed in Table 7.2. 95%

confidence upper limits on the cross section are set by solving Equation 7.2:

$$0.95 = \int_0^{\sigma_{95\%}} L(\sigma|n)\mathrm{d}\sigma. \tag{7.4}$$

where the uncertainties on photon efficiency are taken from Chapter 5, and the background fake rate uncertainty is applied as described in Section 6.2.1.

Quantity	Uncertainty
Luminosity	4.5% relative
photon efficiency vs. pileup	4%
photon efficiency vs. E_T/η	2.5%
photon data/MC energy scale	3.9%
Signal Efficiency	**12.2% relative**
background diphoton efficiency	11.1% relative
background photon k-factor	7% relative
background diphoton	**13.2% relative**
background fake rate	20% (See Section 6.2.1)

Table 7.2: Systematics used for nuissance parameters in limit calculation

This procedure is used over a scan of the coupling parameter $\tilde{k}$ and the first resonance mass M_1, leading to upper limits on the cross section as a function of mass. The results for $\tilde{k} = 0.01, 0.05,$ and 0.10 are shown in Figures 7.8, 7.9, and 7.10

In each figure, the red dotted line represents the expected limit, based on the background predictions, with the green and yellow bands representing the $\pm 1\sigma$ and $\pm 2\sigma$ deviations from the median expectation. As the number of expected background drops below one, the bands also become one sided because fluctuations to negative event yields are not possible. Similarly, the upper band eventually disappears when the background rate is so low that an upward fluctuation to 1 event becomes sufficiently improbable. The solid black line represents the actual observed limit, using the number of data points observed in each search window. The choices of M_1, and the corresponding mass windows (discussed in Chapter 5) used in the scan leads to the discrete features of the line, and these correspond to inclusion and exclusion of data points as they fall inside and outside the given mass windows. Above 1 TeV, there are no events observed in the data, and the observed limit very closely matches

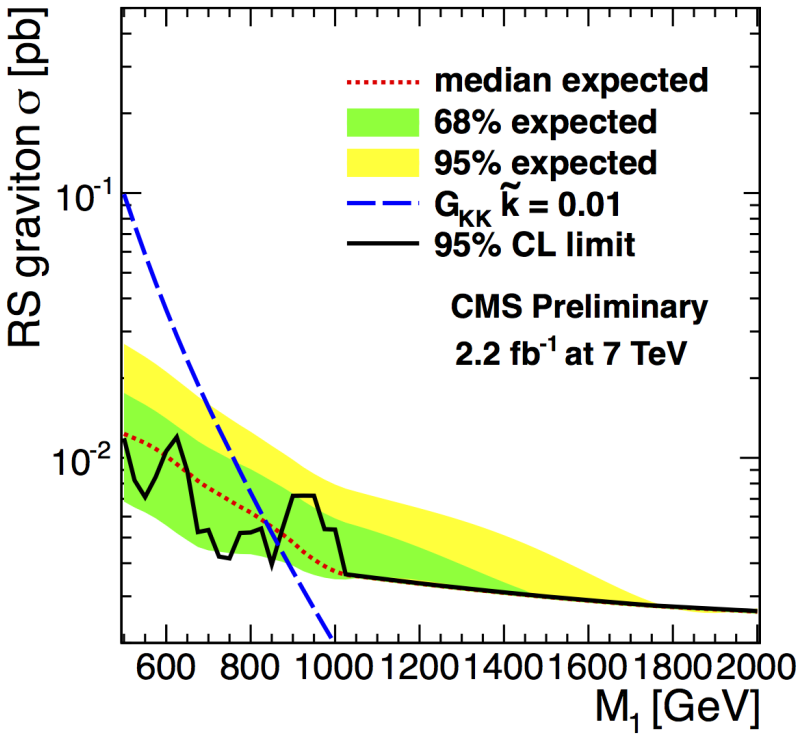

Figure 7.8: 95% CL upper limit on the RS graviton cross section for $\tilde{k} = 0.01$ as a function of the diphoton resonance mass M_1.

the expected limits.

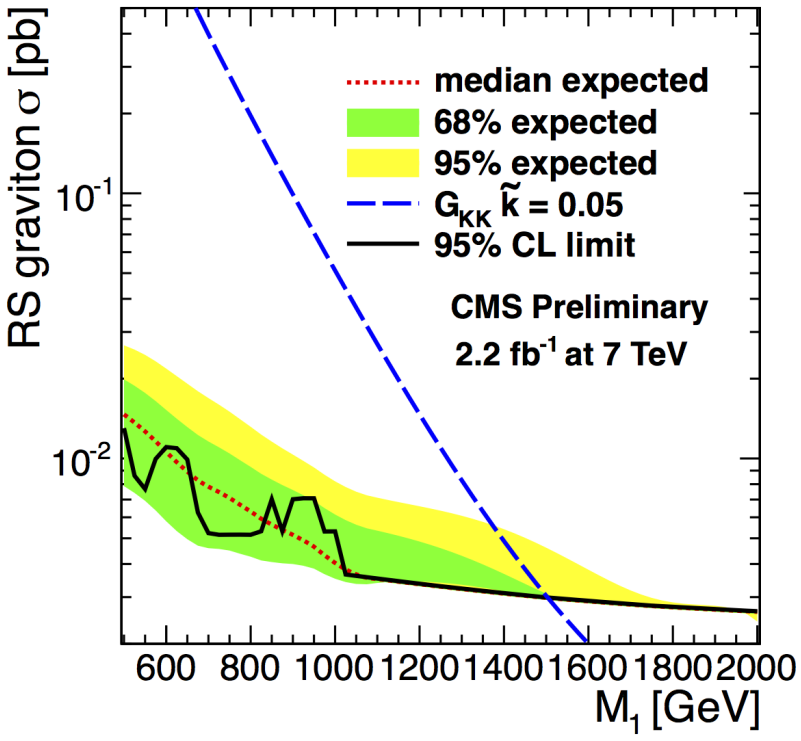

Figure 7.9: 95% CL upper limit on the RS graviton cross section for $\tilde{k} = 0.05$ as a function of the diphoton resonance mass M_1

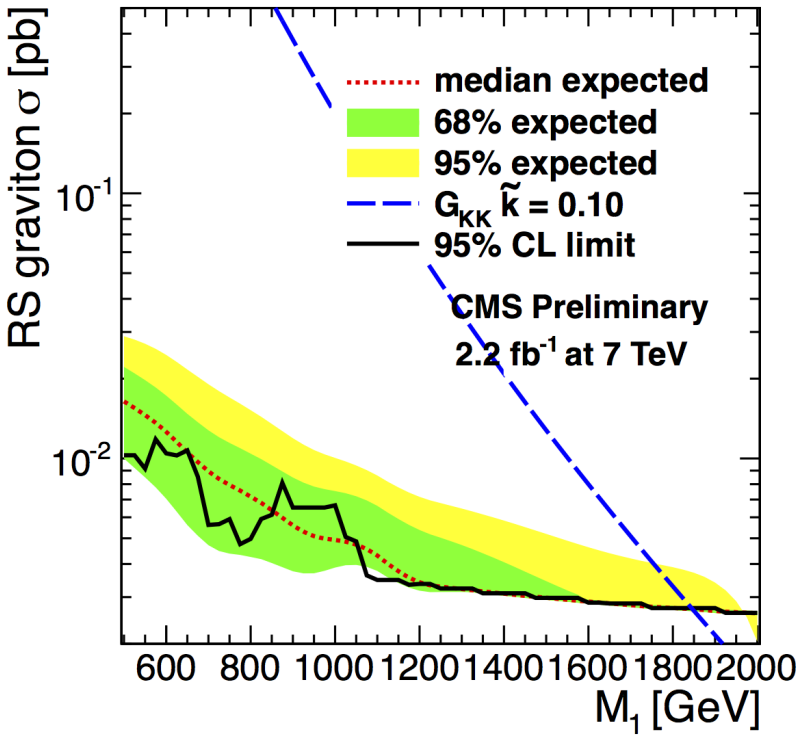

Figure 7.10: 95% CL upper limit on the RS graviton cross section for $\tilde{k} = 0.10$ as a function of the diphoton resonance mass M_1

7.2 Interpretation in RS Models

To translate the general cross section upper limits into limits on the model parameters $\tilde{k}$ and M_1, the cross section for graviton production as a function of M_1 is plotted for each value of the coupling as a dashed line in Figures 7.8, 7.9, and 7.10. The intersection of the signal cross section line and the cross section limit line represents the lower bound on graviton mass for each coupling value. The corresponding mass limits are shown in Table 7.3, and the exclusion in the two parameter ($\tilde{k}$,M_1) space is plotted in Figure 7.11. Electroweak and naturalness constraints,[1] together with the results of this analysis, have now excluded all masses for weak values of the coupling $\tilde{k} < 0.03$.

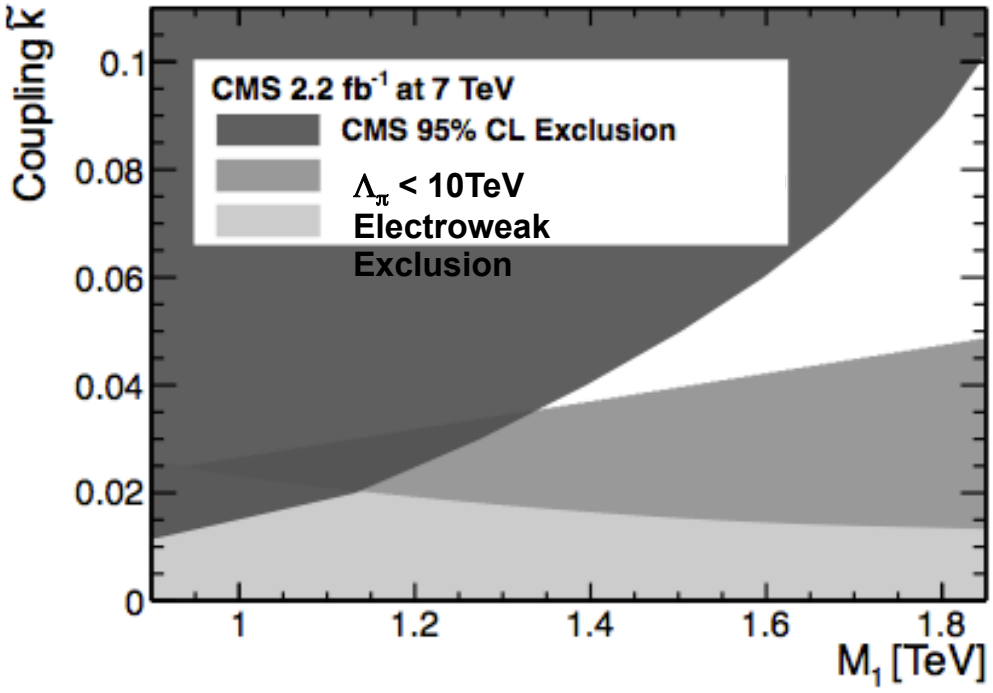

Figure 7.11: 95% CL exclusion in RS parameter space

[1] As discussed in Chapter 1, the curvature has a natural restriction related to the mass scale of the RS theory, M_5. In effect, for the theory to remain perturbative, $\tilde{k} < 0.1$.

$\tilde{k}$	0.01	0.02	0.03	0.04	0.05	0.06	0.07	0.08	0.09	0.10	0.11
M_1 [TeV]	0.86	1.13	1.27	1.39	1.50	1.59	1.67	1.74	1.80	1.84	1.88

Table 7.3: The 95% CL lower limits on M_1 for given values of the coupling parameter, $\tilde{k}$. For $\tilde{k} < 0.03$, masses above the presented limits are excluded by the electroweak data [14] and by naturalness constraints.

7.3 Comparison with other results

The results presented here represent the most stringent experimental limits to date, as shown in Table 7.4 where we compare them to the results obtained by other experiments. The benefit of the high signal cross section from the high energy of the LHC leads to the much stronger limits obtained by the CMS and ATLAS analyses, compared to similar analyses at CDF and D0 with more than twice the luminosity. Of further note is that the ATLAS analysis is performed assuming a flat signal k-factor of 1.75, which is higher than the maximum value from the updated theory calculations used for this analysis. Additionally, we remark that the CMS dilepton search will become nearly competitive with the diphoton analysis when the full luminosity is analyzed, and the two results are targeted for a future combination at the time of this writing.

$\tilde{k}$	CMS $\gamma\gamma$ 2.2 fb^{-1}	ATLAS $\gamma\gamma$ [44] 2.12 fb^{-1}	CDF $\gamma\gamma$ [26] 5.4 fb^{-1}	CDF e^+e^- & $\gamma\gamma$ [27] 5.7 fb^{-1}	D0 e^+e^- & $\gamma\gamma$ [28] 5.4 fb^{-1}	CMS e^+e^- [45] 1.1 fb^{-1}
0.01	860	740	459	604	560	-
0.03	1270	1260	-	-	-	-
0.05	1500	1410	838	937	940	1300
0.1	1840	-	963	1055	1050	1590
0.11	1880	1790	-	-	-	-

Table 7.4: Comparison of result from different experiments: 95% CL limits obtained on the RS graviton mass (GeV) for different values of the coupling parameter $\tilde{k}$.

Chapter 8

ADD Intepretation

8.1 ADD Theory of Large Extra Dimensions

The results of the RS graviton search can also be used to set limits on Large Extra Dimensions, as formulated by Arkany-Hamed, Dimopoulos and Dvali citeADD. In the case of large EDs, the modes of excitation are quantized as in the case of energy levels in a potential well, but because of the large size of the EDs, the spacing between levels is small O(10^{-3}eV to 100 MeV) compared to the detector resolution, and this produces an apparently continuous spectrum. This is especially relevant in the high mass region, where there are many more contributing modes. Thus, we do not search for a particular resonance, but for an excess in the diphoton production rate over the SM predictions.

Summation over all modes is divergent, so an ultraviolet (UV) cutoff is introduced (M_S). The scale M_S is related to, but possibly different from, the fundamental planck scale M_D, with the exact relation depending on the UV completion of the theory. The effects of virtual graviton production (Figure 8.1) on the diphoton cross section are parametrized by a single variable, $\eta_G \equiv \mathcal{F}/M_S^4$, where $\mathcal{F}$ is an order-unity dimensionless parameter, for which several conventions exist:

$$\mathcal{F} = 1 \quad \text{(Giudice, Rattazzi, and Wells, GRW [46])}, \tag{8.1}$$

$$\mathcal{F} = \begin{cases} \log\left(\frac{M_S^2}{\hat{s}}\right) & \text{if } n_{ED} = 2 \\ \frac{2}{(n_{ED}-2)} & \text{if } n_{ED} > 2 \end{cases} \quad \text{(Han, Lykken, and Zhang, HLZ [47])}, \tag{8.2}$$

$$\mathcal{F} = \pm\frac{2}{\pi} \quad \text{(Hewett [48])}, \tag{8.3}$$

where $\sqrt{\hat{s}}$ is the center-of-mass energy of the hard parton-parton collision.

The GRW choice of unity for $\mathcal{F}$ is natural when there are no other desired features. We note that the HLZ convention (uniquely among the three) contains an explicit dependence on n_{ED}, and that the Hewett convention allows for both constructive and destructive interference (via the minus sign) with the Standard Model processes.

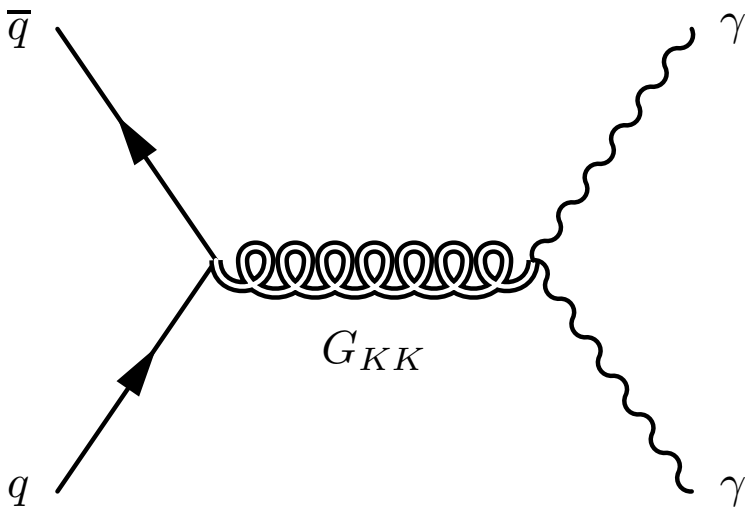

Figure 8.1: Feynman diagram for virtual KK graviton production through $q\bar{q}$ annihilation decaying into two photons.

8.2 Limit calculation

The event selection is identical to the one used in the RS analysis, with the exception of the search mass windows. Since there is no particular resonance mass hypothesis, the search extends over a one sided window, starting at a cutoff which was found to

be optimal at $M_{\gamma\gamma} > 900$ GeV. Additionally, the signal k-factor is treated as non-differential, and the variation with respect to $M_{\gamma\gamma}$ is treated as part of the systematic uncertainty on the signal yield.

The simulation of ED in the ADD model is performed using version 1.3.0 of the SHERPA [49] MC generator. The simulation includes both SM diphoton production and signal diphoton production via virtual-graviton exchange in order to account for the interference effects between the SM and ADD processes. The LO SHERPA cross sections are multiplied by a constant NLO K factor of 1.6 ± 0.1, a value that represents an updated calculation by the authors of [32, 50]. The systematic uncertainty on the signal K factor reflects the approximate variation of the K factor over a large region of the model parameter space; it is not intended to account for the theoretical uncertainty. This differs from the RS case, where an explicitly $M_{\gamma\gamma}$ dependent k-factor was used because of the M_1 dependent mass windows. The cross sections in the simulation are conservatively set to zero for $\sqrt{\hat{s}} > M_S$ because the theory becomes non-perturbative for larger values of $\sqrt{\hat{s}}$. Introducing this sharp truncation reduces the upper limits on M_S by a few percent, compared to allowing them to extend into the non-perturbative region.

The background estimations are the same as in the RS graviton case, and the last column of Table 8.1 represents the prediction and observation in the signal region, while the first columns represent the control regions. The data agree with the sum of the predicted backgrounds, as already discussed in Chapter 7.

Process	Diphoton Invariant Mass Range [TeV]			
	[0.14, 0.2]	[0.2, 0.5]	[0.5, 0.9]	> 0.9
Multijet	15 ± 6	17 ± 7	0.2 ± 0.1	0.003 ± 0.001
$\gamma +$ jet	102 ± 15	124 ± 18	2.5 ± 0.4	0.19 ± 0.04
Diphoton	372 ± 70	414 ± 78	16.9 ± 3.2	1.3 ± 0.3
Backgrounds	489 ± 73	555 ± 81	19.6 ± 3.2	1.5 ± 0.3
Observed	484	517	16	2

Table 8.1: Observed event yields and background expectations for different reconstructed diphoton invariant-mass ranges. Full systematic uncertainties are included.

8.3 Interpretation in terms of model parameters

To set limits on virtual-graviton exchange in the ADD scenario, we compare the number of observed and expected events in the signal region ($M_{\gamma\gamma} > 0.9\ TeV$) and set 95% confidence level (CL) upper limits on the quantity $S \equiv (\sigma_{\rm total} - \sigma_{\rm SM}) \times \mathcal{B} \times \mathcal{A}$, where $\sigma_{\rm total}$ represents the total diphoton production cross section (including signal, SM, and interference effects), and $\sigma_{\rm SM}$ represents the SM diphoton production cross section. The signal branching fraction to diphotons is indicated by $\mathcal{B}$ and the signal acceptance by $\mathcal{A}$. We use the Bayesian technique [40] to compute the limits with a likelihood constructed from the Poisson probability to observe N events, given S, the signal efficiency $(76.4 \pm 9.6)\%$, the expected number of background events (1.5 ± 0.3), and the integrated luminosity $\mathcal{L} = (2.2 \pm 0.1)\ fb^{-1}$ [51]. The basis for such limit calculations is as discussed in Chapter 7.

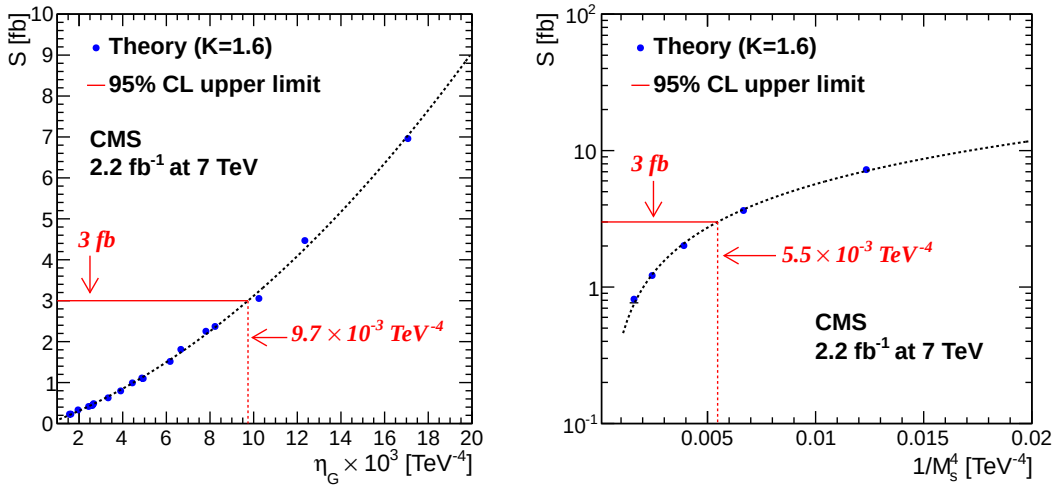

Figure 8.2: Signal cross section S parameterization as a function of the strength of the ED effects, η_G (left) and as a function of $1/M_S^4$ for the HLZ $n_{ED} = 2$ case (right).

The observed 95% CL upper limit on S is 3.0 fb. For the HLZ $n_{ED} = 2$ case, we parameterize S directly as asmooth function of $1/M_S^4$, because it is the only case where the coupling $\mathcal{F}$ depends explicitly on M_S. For all other conventions, S is parameterized as a function of the parameter η_G, as in [52], and can be simply transformed into a condition on M_S, by inverting the relations in equations 8.1, 8.2, and 8.3. The observed 95% CL limit, together with the signal parameterization, is

shown in Fig. 8.2. The intersection of the cross section limit with the parameterized curve determines the 95% CL upper limit on the parameter η_G in the left plot, and on the parameter $1/M_S^4$ in the right plot. As seen from the plots, these upper limits on S correspond to upper limits of $\eta_G \leq 0.0097$ TeV^{-4} and $1/M_S^4 \leq 0.0055$ TeV^{-4}. The upper limits on η_G are equated to lower limits on M_S for each of the conventions other than HLZ, and are shown together in Table 8.2.

K factor	GRW	Hewett		HLZ (n_{ED})					
		positive	negative	2	3	4	5	6	7
1.0	2.94	2.63	2.28	3.29	3.50	2.94	2.66	2.47	2.34
1.6	3.18	2.84	2.41	3.68	3.79	3.18	2.88	2.68	2.53

Table 8.2: The 95% CL lower limits on M_S (in TeV) in the GRW, Hewett, and HLZ conventions for two values of the ADD signal K factor. All limits are computed with a signal cross section truncated to zero for $\sqrt{\hat{s}} > M_S$. The limits are presented for both positive and negative interference in the Hewett convention and for $n_{ED} = 2$–7 in the HLZ convention.

Note that the limits are stronger in the positive interference case than the negative interference, as expected. The limits become less restrictive as the number of extra dimensions increases, with the exception of the $n_{ED} = 2$ case where the M_S dependence is slightly weakened by the additional logarithmic term. All of these limits are the most stringent to date.

Chapter 9

Summary and Outlook

9.1 Summary

2.2 fb^{-1} of data collected at $\sqrt{s} = 7$TeV were analyzed, and no excess over the SM predicted diphoton distribution was found. In the context of the Randall–Sundrum model, lower limits are set on the mass of the first graviton excitation in the range of 0.86–1.84 TeV for values of the associated coupling parameter $\tilde{k}$ between 0.01 and 0.10. Additionally, in the context of the large-extra-dimensions model, lower limits are set on the effective Planck scale in the range of 2.3–3.8 TeV at the 95% confidence level. These are the most restrictive bounds to date.

9.1.1 Potential Effects on Higgs Production

Recently, experiments at the LHC and the Tevatron have observed a small excess of events which may be the sign of a Higgs boson signal. If this excess is confirmed with additional data, then it will be critical to confirm whether it is produced with the SM cross section. It will also be important to understand how the electroweak and Planck scales are related, quite possibly through extensions of the SM. The couplings for photons and gluons to Higgs are zero at tree level, but non-zero at first loop order and higher. These couplings are therefore sensitive to new heavy particles, which contribute to the loop integrals. An understanding of the effects of any particular extension of the SM on these processes then allows the measurement of the Higgs

cross section to constrain the properties of the new physics.

In particular, the effect of the RS gravitons of a warped extra dimension have been derived analytically [53].

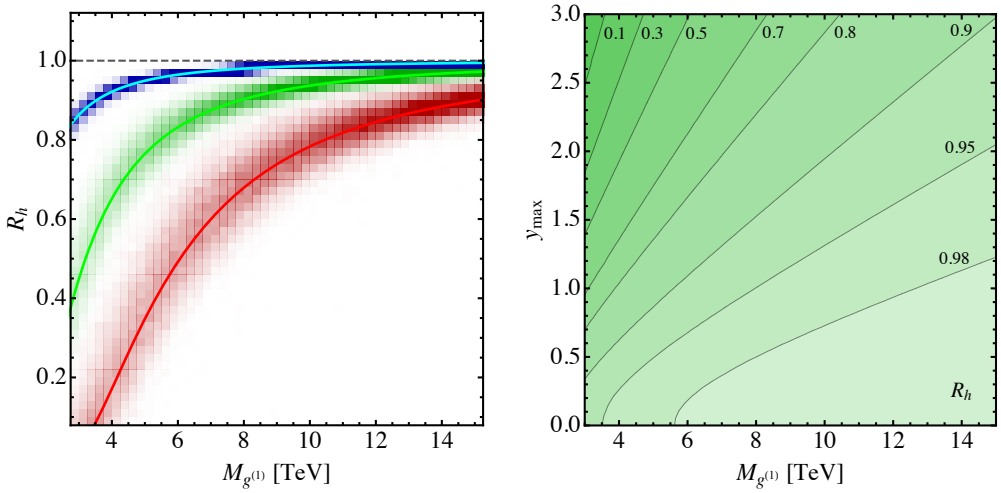

Figure 9.1: Predicted ratio R_h in a minimal RS model to the SM for $\sigma(gg \to H)$. The red, green, and blue density bands correspond to different choices of the parameter y_{max} (left). Contour plot of R_h using a parametrization of the center of the bands (right). [53]

If the excess of events is indeed confirmed as Higgs boson signal, then the careful measurement of the production cross section will yield information about the parameters of any extra dimensional extension to the SM.

9.2 Projection for 2012 Dataset

In the 2012 running, it is anticipated that CMS will record a total of 20 fb^{-1}. For this dataset, the expected limits can be calculated assuming a similar set of efficiencies for signal and background, and projecting out to the higher luminosity number. This assumption would overestimate the sensitivity of the analysis if no further improvements are made to the selection with regards to pileup, as the number of reconstructed vertices has greatly increased since this analysis was completed. Recall from Section 5.2 the decrease in efficiency for a fixed selection as a function of pileup, which was assigned a 4% systematic uncertainty in the present analysis, but

would need either a much larger uncertainty, or an implementation of a subtraction of "average" pileup deposits to restore the efficiency. However, the projection with existing Monte Carlo simulation samples also does not include the increase in signal cross section from the increase in the collision energy from 7 to 8 TeV. For the values of the coupling $\tilde{k} = 0.01, 0.02$, and 0.03, the expected lower limits on the mass are respectively $1300, 1570, 1930$ GeV, and above this, the lack of MC simulations with 2000 GeV $< M_1 <$ 4000 GeV precludes estimating the mass limits with this simple method. One can already see that nearly the entire parameter space in Figure 9.2 will be covered, and if a similar increase in the mass limits for coupling values above $\tilde{k} = 0.03$ is assumed, the mass limit for $\tilde{k} = 0.10$ would be ~ 3 TeV, and this would cover most of the remaining theoretical region, which closes at ~ 4 TeV and $\tilde{k} = 0.10$ (see Figure 1.4).

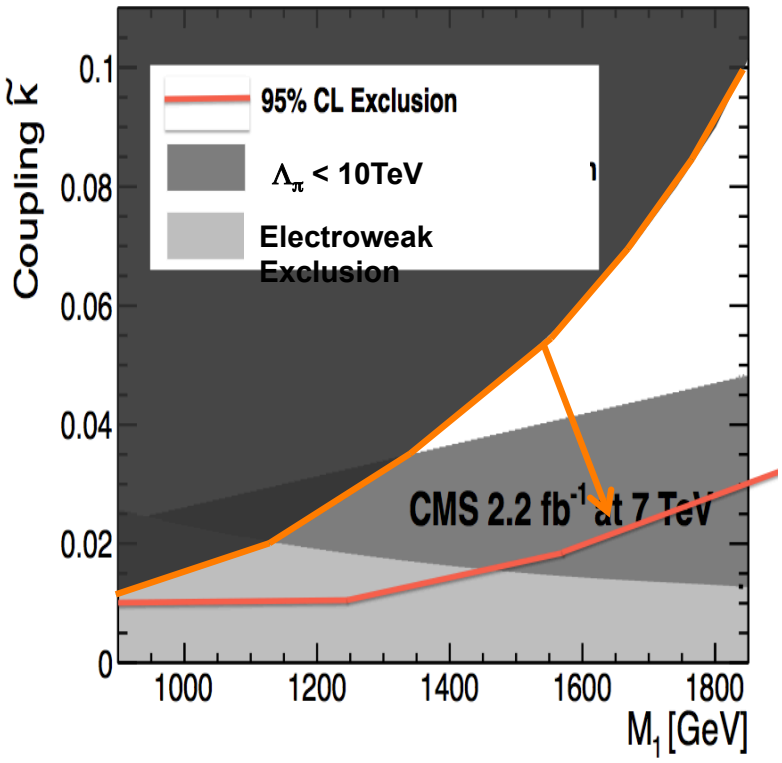

Figure 9.2: 95% CL exclusion in RS parameter space, with 20 fb^{-1}projection overlayed in orange

Although the final word on the original RS Graviton model, in which all of the

SM is constrained to the brane should be coming soon, there are still new implementations of extra dimensions to be explored. For example, other realizations of the RS model [48, 54, 55] which allow SM particles to reside in the extra dimensional bulk could explain the fermion mass generations and hierarchy, in addition to solving the Planck and Electroweak scale hierarchy problem. In such models, the constraints on the first excited mass of the graviton from the LHC data would be less restrictive. Which, if any, of these theories is correct? Only nature knows, and I leave further exploration to the next generation of students.

Appendix A

Multivariate Analysis for $H \to \gamma\gamma$

A.1 SM Higgs

This section covers prior work on early $H \to \gamma\gamma$analysis, before the startup of LHC. One key role of the Higgs in the SM is to allow mass terms for fermions and vector bosons, without violating either SU2 or gauge symmetries. Production of the Higgs at LHC proceedes mainly via gluon fusion, though there are also important contributions from vector boson fusion (VBF), and associated productions with either a W/Z or $t\bar{t}$, as shown in Figure A.1.

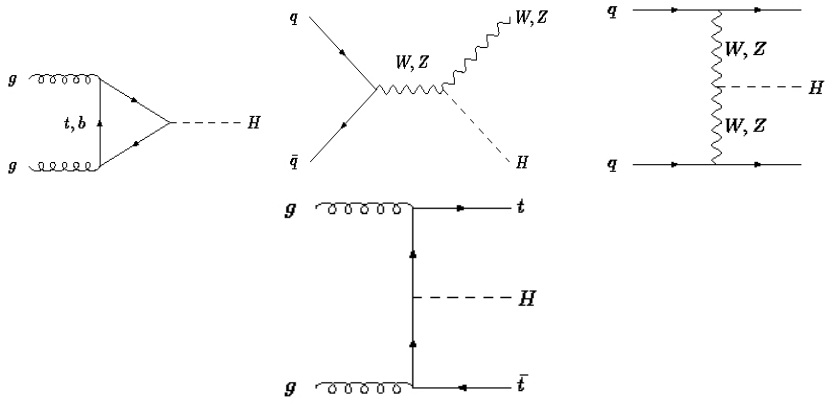

Figure A.1: Feynman diarams for Higgs

The associated cross sections are plotted in Figure A.2, and from the branching ratios it is also clear that the $\gamma\gamma$ mode is most significant at low masses.

The background processes are the same as for the RS graviton search, namely

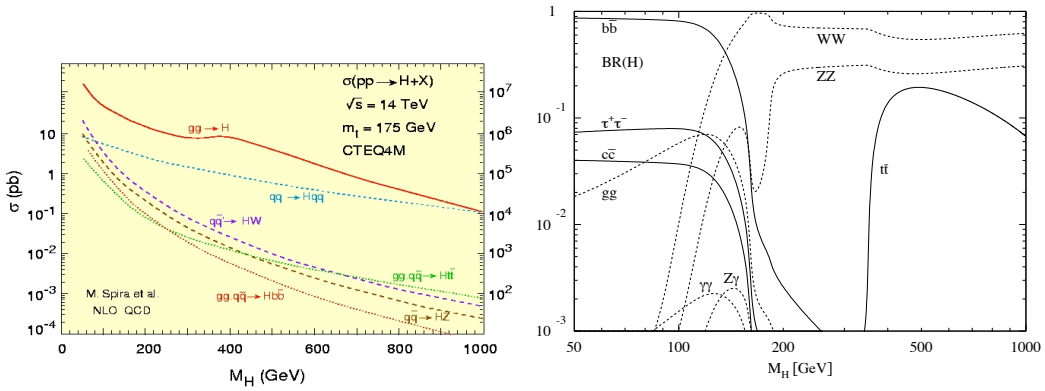

Figure A.2: Higgs production cross section and branching ratios

SM diphoton production, and $\gamma + jet$ and dijet production with the jets misidentified as photons. The reducible jet backgrounds are handled by photon ID selections, while the main handle on SM diphoton production is kinematic selection. One significant difference from the graviton case is the larger background expectations, due to the lower mass range of interest. Thus, background rejection, as well as event categorization, are important for optimizing the discovery potential of an analysis.

A.2 Stat Pattern Recognition

The analysis started with a traditional set of cut based selections, and was enhanced by using a multivariate method called Bagged Decision Trees (BDT) to enhance the significance. Bagging (Bootstrap Aggragating), is a statistical method to improve classification by using multiple copies of training data, generated from a larger training set. For each training subset, a decision tree (Figure A.3) is trained the data to optimize selection accuracy, and the equal weighted voting of these trees results in an ouput ranging from 0 to 1.

The framework is StatPatternRecognition, developed at Caltech by Ilya Narsky[56]. As with any multivariate classifier, there is the risk of overtraining on a given dataset, which can lead to unreliable results when applied from training set to validation sample. To counteract this, the entire simulated data sample is split into 3 exclusion parts, for training, monitoring, and validation (Figure A.4).

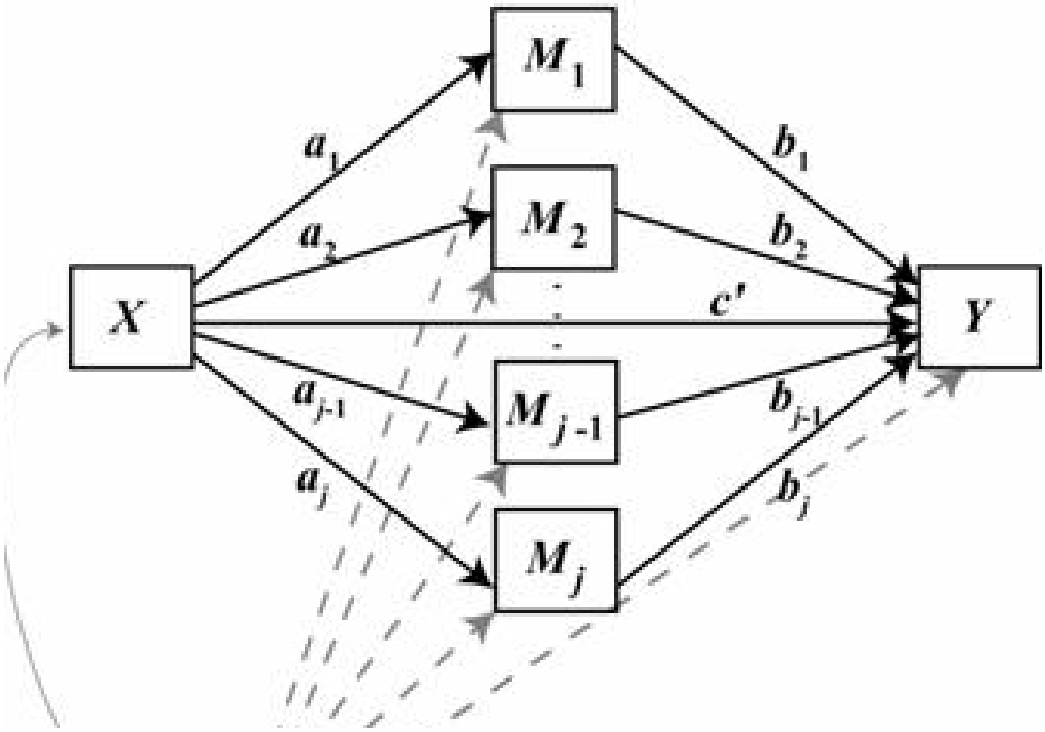

Figure A.3: Diagram of a Decision Tree

Figure A.4: Distribution of events for training and validation

A.3 Photon ID and Event selection

Again as in the RS analysis, the early Higgs analysis relies on shower shape and isolation deposits to identify photons. The shower shape variable used was R9, the ratio of 3x3 to SC energy, and tracker and ECAL isolations were applied. In this case, the track isolation is a count of the number of tracks with $p_T > 1.5$ GeV around the SC candidate, and the ECAL isolation is required to be < 1.25 GeV.

A.4 Fermiophobic models

Fermiophobic models contain an additional discriminating feature, which is the presence of two high η jets, due to VBF production becoming the dominant mode (ggH

relies on top quarks in the lowest loop order diagram). Two strong variables are the difference in η, which is large for jets in opposite hemispheres (Figure A.5), and the product of the η of the two jets, which is treated as a signed variable, and negative for opposite hemisphere jets, and positive otherwise. The distribution for the two variables is plotted in Figure A.6.

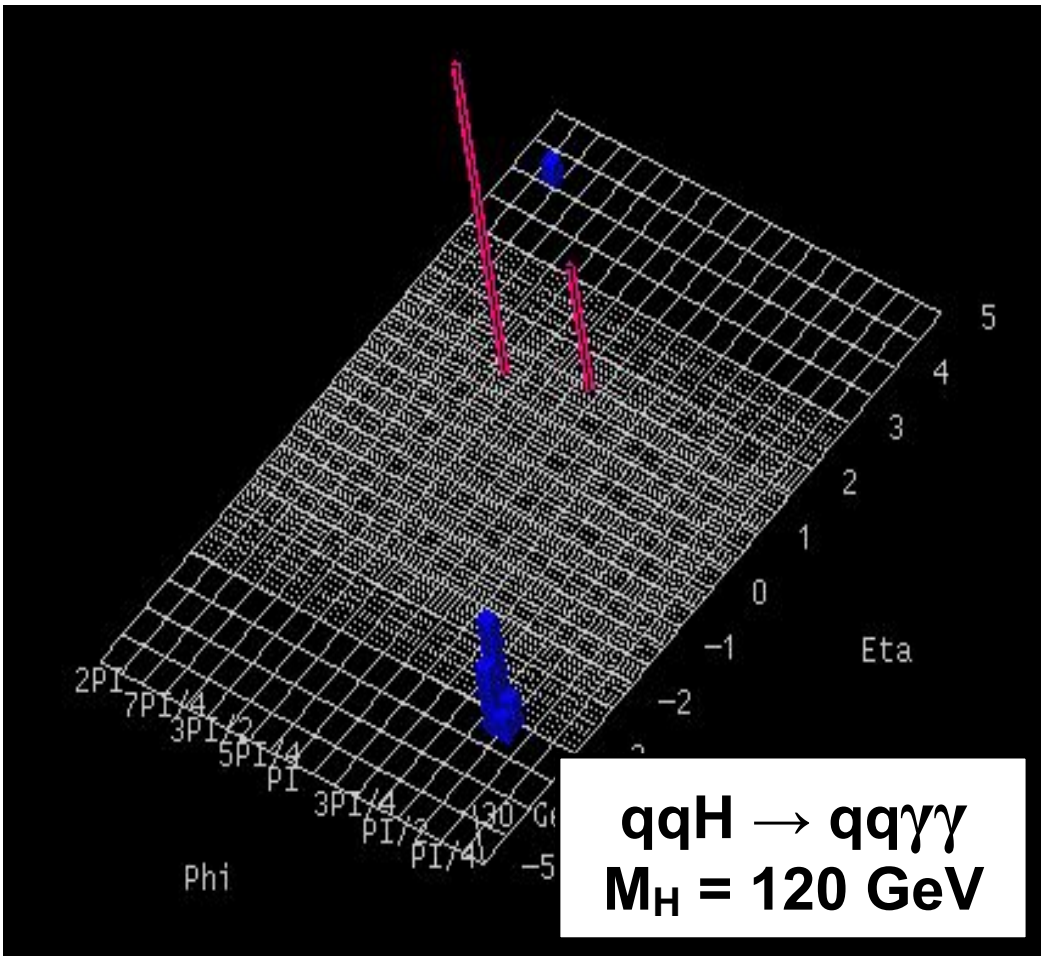

Figure A.5: Simulated VBF Event Display

The same variables are input to the BDTs, and the training is monitored for convergeance via a figure of merit (FOM), in this case the significance. It is clear from Figure A.7 that the training is quickly convergeant, and so the results are then applied to the validation sample, leading a spectrum of BDT outputs for each given sample.

In Figure A.8, the left plot shows the output for Signal and Background samples,

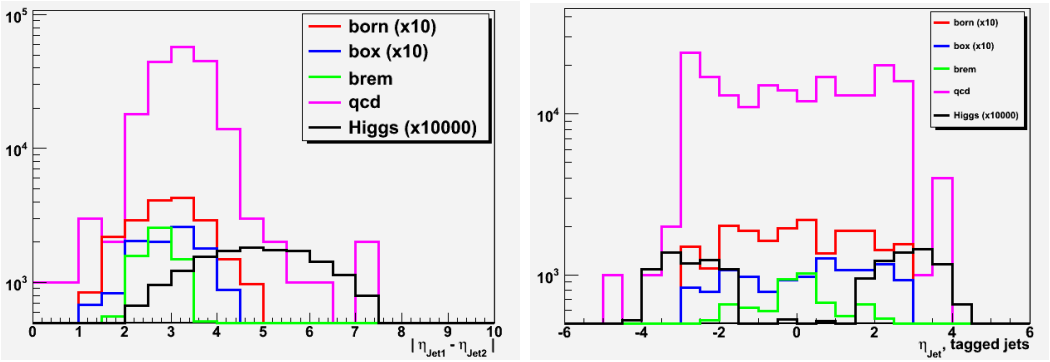

Figure A.6: Jet tagging variables for VBF

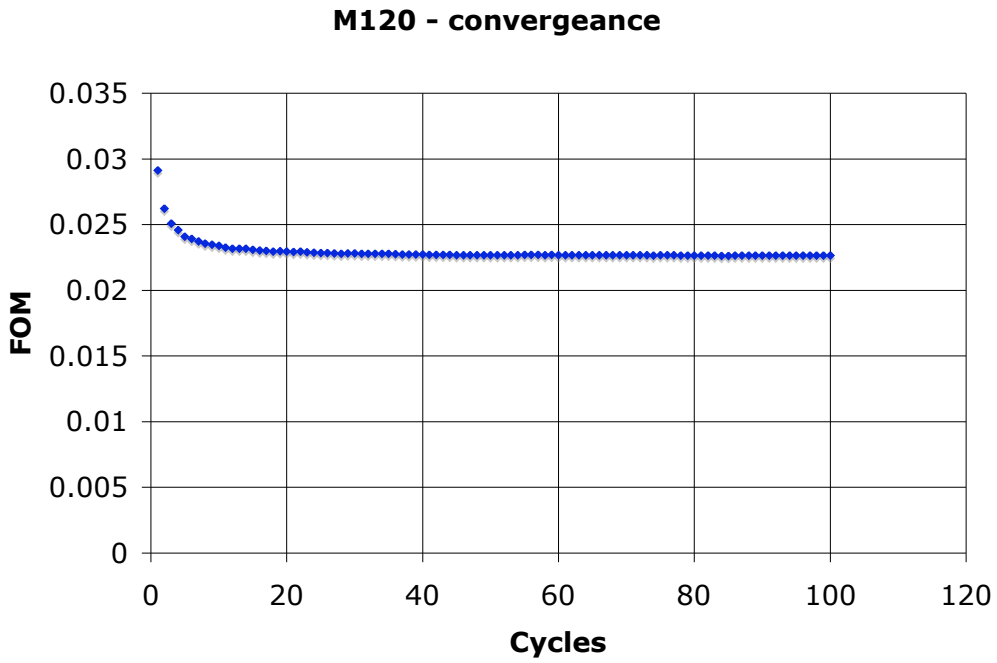

Figure A.7: Convergeance of BDT training

and the right plot is the same plotted into a 2D band. The 2D band will be used later for visualization in the case of multiple background and signal process types. Selection of a particular output threshold leads to corresponding values of N_S and N_B, which are then used to compute the significance of the selection.

For the same background rate as the cut based selection, there is significant improvement from using the BDT selection, as shown in Table A.1.

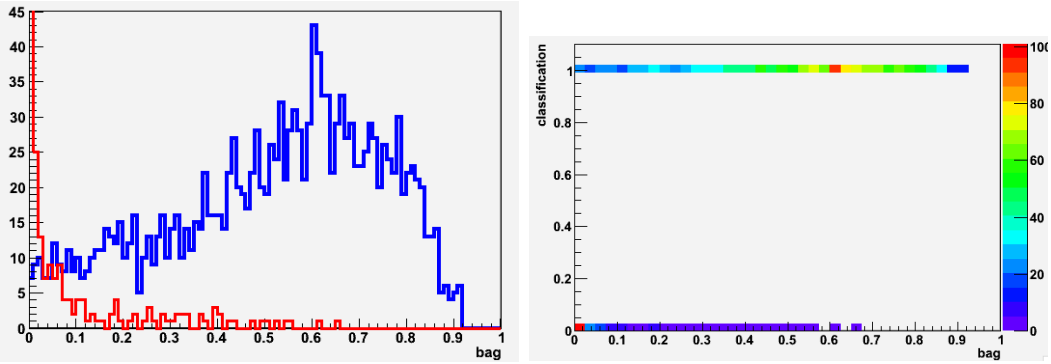

Figure A.8: Histogram of BDT outputs and corresponding 2D plot

Sample (GeV)	M = 120	M = 130	M = 140	M = 150
Cross Section (fb)	12	11.5	8.8	5.7
Events/fb, selected, cuts	0.39 ± 0.01	0.42 ± 0.02	0.40 ± 0.02	0.26 ± 0.01
Events/fb, selected, BDT	0.67 ± 0.03	0.73 ± 0.03	0.47 ± 0.02	0.33 ± 0.01

Table A.1: Event rates for cut based and BDT selections

A.5 Inclusive Production

In the inclusive selection, the jet tagging is no longer used, but there is an order of magnitude gain in cross section from inclusion of the ggH process. BDTs are used once again, but this time in a two phase training. The first phase trains the photon ID, using the isolation and shower shape variables as input, and training against the jet fake backgrounds only. The final phase uses the BDT output from the photon ID phase, along with the kinematic variables, and is trained against the full cocktail of backgrounds, including SM diphotons. The results can be seen a 2D band plot (Figure A.9) and the corresponding improvement in significance is shown in Figure A.10.

Clearly, the use of MVAs will be important in the optimization of the $H \rightarrow \gamma\gamma$analysis.

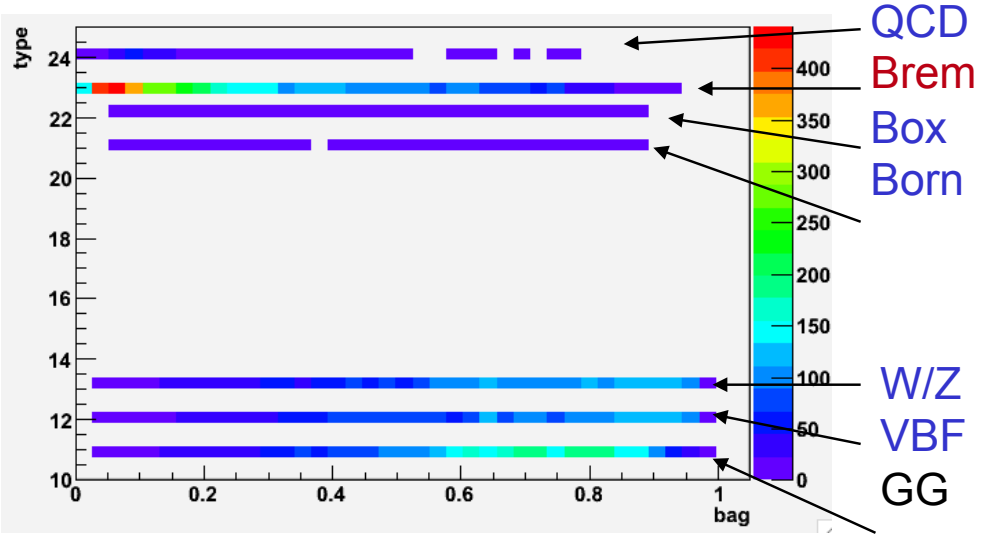

Figure A.9: Output bands for BDT trained for inclusive higgs

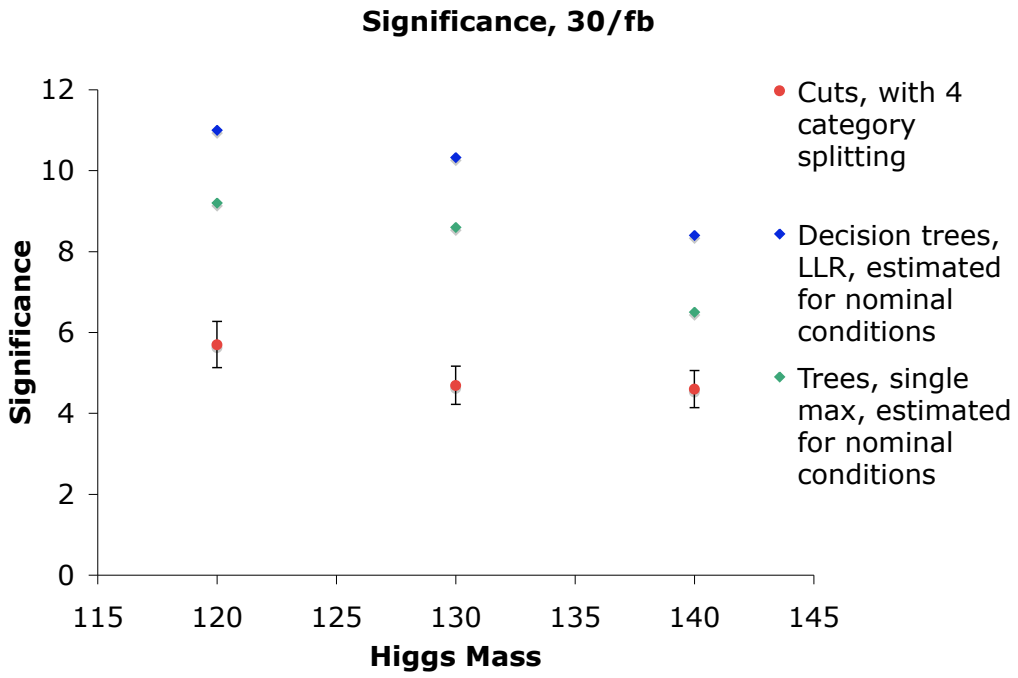

Figure A.10: Significance scenarios for inclusive Higgs

Appendix B

$H \rightarrow \gamma\gamma$ Mass Resolution

One of the main design goals of the LHC is to discover the Higgs boson. The $\gamma\gamma$ mode is promising because of the clean photon signature, and also the good resolution possible with the ECAL. The main theoretical challenge for the analysis is the abundance of irreducible background, from other SM diphoton processes, leading to a strong dependence of the sensitivity on the mass resolution for signal.

The mass of an object decaying into two photons or electrons is generally calculated as :

$$m^2 = 4E_1E_2 \sin^2 \frac{\Theta}{2} \tag{B.1}$$

Where E_1, E_2 are the energy of the photons, and Θ is the angle between the two three-vectors.

The error on the mass is then given as :

$$\frac{\Delta(m)}{m} = \frac{1}{2} \times \frac{\Delta(E_1)}{E_1} \oplus \frac{\Delta(E_2)}{E_2} \oplus \frac{\Delta(\Theta)}{tan(\frac{\Theta}{2})} \tag{B.2}$$

Unlike electrons, for which the $Z \rightarrow ee$ provides a standard candle, the signal modeling for $H \rightarrow \gamma\gamma$ must rely on MC simulation, combined with corrections gleaned from data/MC comparisons for electrons, and electron/photon similarities and differences. The following sections detail efforts to make these comparisons.

B.1 Line shape and resolution of $H \to \gamma\gamma$ signal for MC events

In this section we fit the MC signal line shape to measure the mass resolution for $H \to \gamma\gamma$ MC signal event. We carry out several systematic studies to estimate the uncertainties related to the extraction method and the event selection and categorisation. We also study how to relate the resolution measured in $Z \to ee$ to the one measured in $H \to \gamma\gamma$.

In all cases the resolution function is assumed to be of the Crystal Ball form:

$$CB(x;\alpha,n,\bar{x},\sigma) = \begin{cases} exp(-\frac{(x-\bar{x})^2}{2\sigma^2}), & \text{for} \frac{x-\bar{x}}{\sigma} > -\alpha \\ A \cdot (B - \frac{x-\bar{x}}{\sigma}), & \text{for} \frac{x-\bar{x}}{\sigma} \leq -\alpha \end{cases} \tag{B.3}$$

where

$$\begin{aligned} A &= (\frac{n}{|\alpha|})^n \cdot exp(-\frac{|\alpha|^2}{2}) \\ B &= \frac{n}{|\alpha|} - |\alpha| \end{aligned} \tag{B.4}$$

B.1.1 $H \to \gamma\gamma$ selection.

For the resolution plots, we use EGM-Tight ID (same as RS graviton analysis), and a symmetric $p_T > 30$ GeV for both photons.

- Ecal Isolation $<$ 4.2GeV + 0.006 * p_T
- Hcal Isolation $<$ 2.2GeV + 0.001 * p_T
- Track Isolation $<$ 2.0GeV + 0.0025 * p_T
- $\sigma_{i\eta i\eta} < 0.01$ (0.028) in EB (EE)
- Had/Em < 0.05

B.1.2 $H \rightarrow \gamma\gamma$ signal MC fit results.

We define the 4 categories as in the $H \rightarrow \gamma\gamma$ baseline analsis [57].

- Category 1: Both photons in EB, Both r9 > 0.94
- Category 2: Both photons in EB, at least one r9 < 0.94
- Category 3: At least one photon in EE, Both r9 > 0.94
- Category 4: At least one photon in EE, at least one r9 < 0.94

B.1.2.1 Spring11 MC

We keep here for reference the shape extraction from Spring11 MC. The difference between the Spring11 and Summer11 MC is a different amount of out-of-time pile-up (OOT PU).

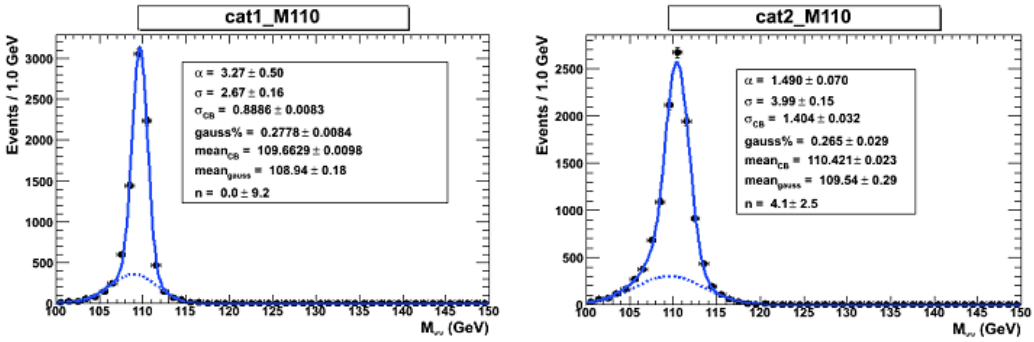

Figure B.1: Category 1 and 2 for the $H \rightarrow \gamma\gamma$ Spring11 MC production.

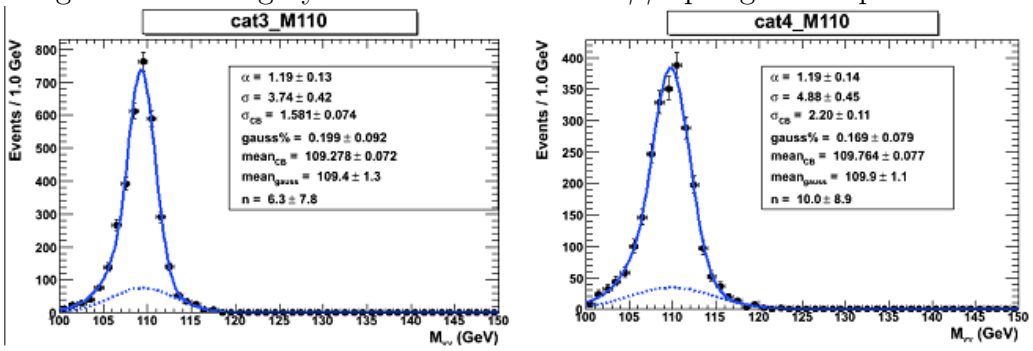

Figure B.2: Category 3 and 4 for the $H \rightarrow \gamma\gamma$ Spring11 MC production.

B.1.2.2 Summer11 MC

Datasets used are from Summer11 MC, with updated PU distributions

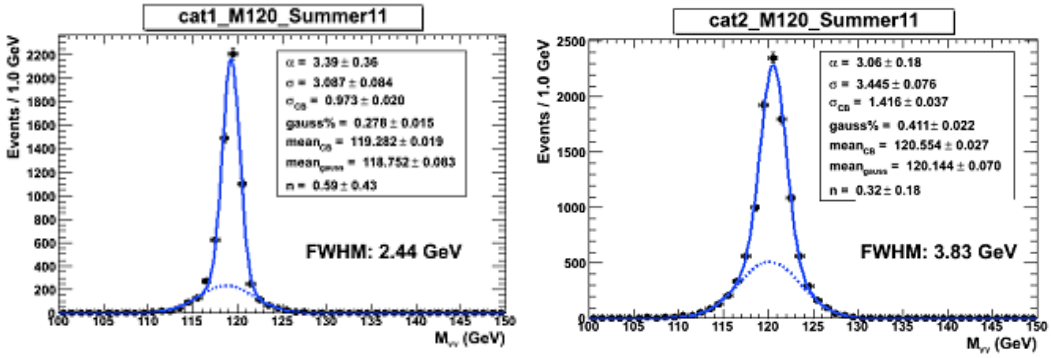

Figure B.3: Category 1 and 2 for the $H \rightarrow \gamma\gamma$ Summer11 MC production.

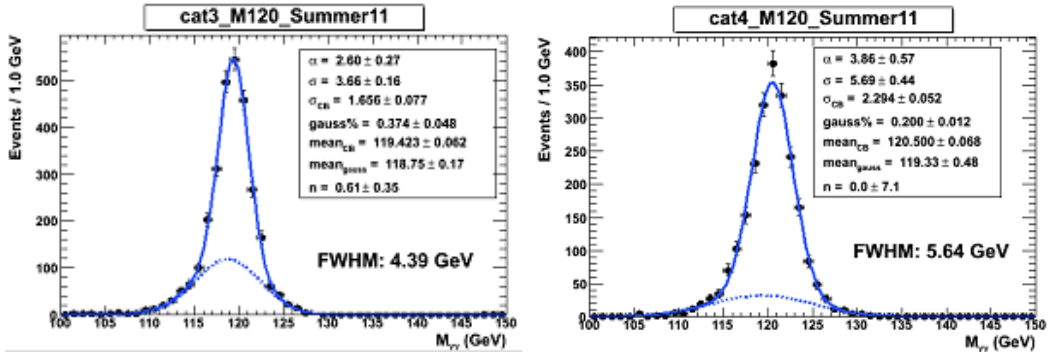

Figure B.4: Category 3 and 4 for the $H \rightarrow \gamma\gamma$ Summer11 MC production.

B.1.2.3 Summer11 MC, vertex matched

To differentiate the effect on resolution from mis-ID of primary vertex, we fit only to those events which have a match of the reconstructed vertex with the generated (true) vertex.

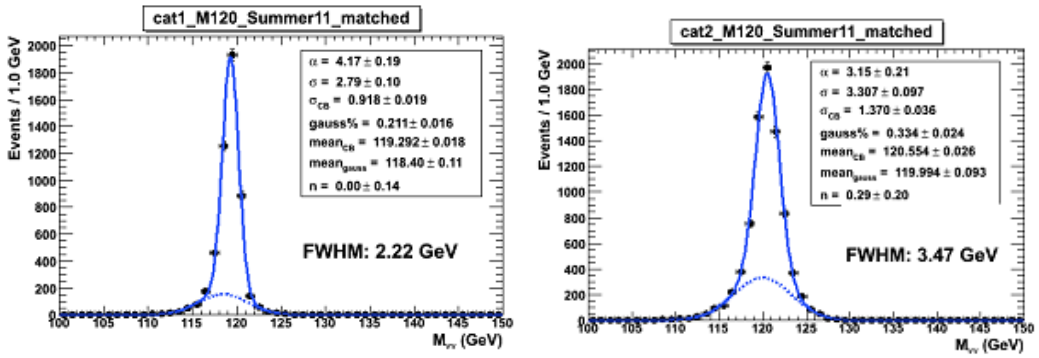

Figure B.5: Category 1 and 2 for the $H \rightarrow \gamma\gamma$ Summer11 MC production. The reconstructed vertex was required to match the true vertex.

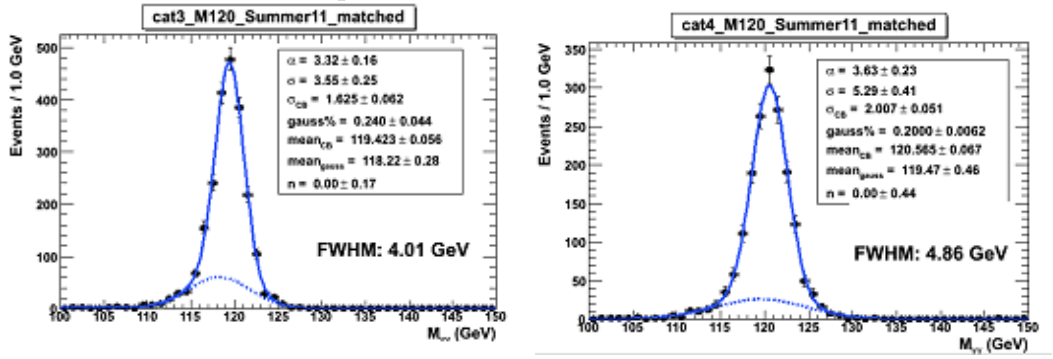

Figure B.6: Category 3 and 4 for the $H \rightarrow \gamma\gamma$ Summer11 MC production. The reconstructed vertex was required to match the true vertex.

B.1.2.4 Summer11 MC, pileup reweighted

To estimate the effect of pile-up we reweighted the in-time pileup to match the estimated pileup from data in May2011.

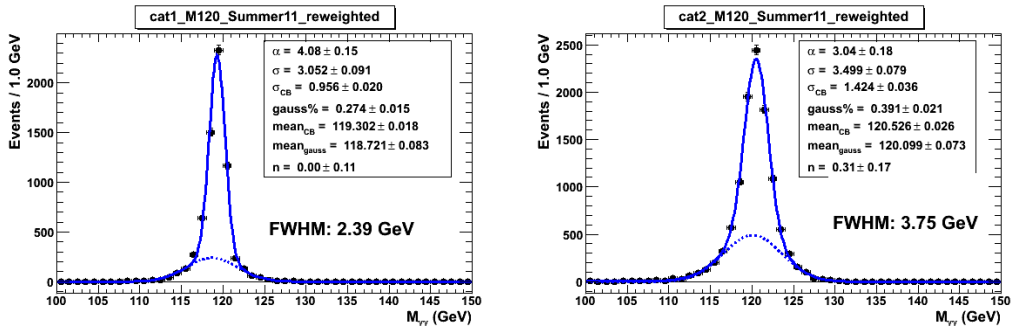

Figure B.7: Category 1 and 2 for the $H \to \gamma\gamma$ Summer11 MC production. Pileup reweighting has been applied.

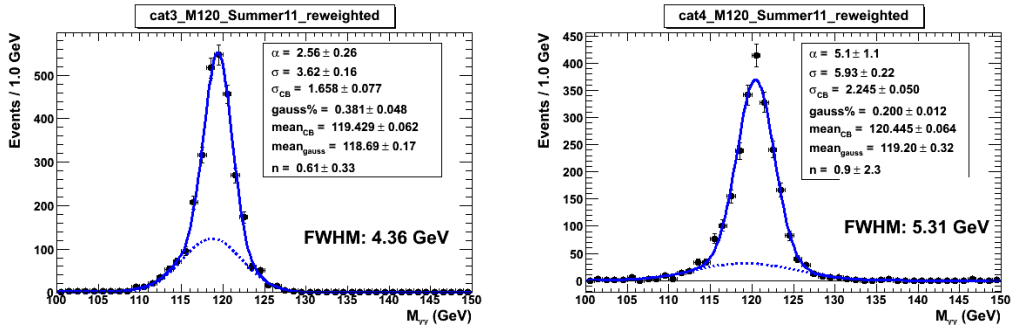

Figure B.8: Category 3 and 4 for the $H \to \gamma\gamma$ Summer11 MC production. Pileup reweighting has been applied.

B.1.3 Summary of the mass resolution extracted from $H \to \gamma\gamma$ signal MC.

$H \to \gamma\gamma$	EBEB, R9>0.94	EBEB, R9<0.94	EEEE, R9>0.94	EEEE, R9<0.94
Spring11 MC, m=110				
$\Delta(m), [GeV]$ reco-true	-0.34 ± 0.01	0.42 ± 0.02	-0.72 ± 0.07	-0.23 ± 0.07
$\sigma(CB), [GeV]$	0.89 ± 0.01	1.40 ± 0.03	1.58 ± 0.07	2.20 ± 0.11
$\sigma(CB), \%$	0.81	1.27	1.44	2.00
$\sigma(GAUSS)$	3.27 ± 0.50	3.99 ± 0.15	3.74 ± 0.42	4.88 ± 0.45
$Gauss\%$	27.8	26.5	19.9	16.9
$FWHM$	2.17	3.35	3.92	5.38
Summer11 MC, m=120				
$\Delta(m), [GeV]$ reco-true	-0.71 ± 0.02	0.55 ± 0.03	-0.58 ± 0.06	0.5 ± 0.07
$\sigma(CB), [GeV]$	0.97 ± 0.02	1.42 ± 0.04	1.66 ± 0.08	2.29 ± 0.05
$\sigma(CB), \%$	0.83	1.29	1.38	1.90
$\sigma(GAUSS)$	3.08 ± 0.08	3.45 ± 0.08	3.66 ± 0.16	5.69 ± 0.44
$Gauss\%$	27.8	41.1	37.4	20.0 (fixed)
$FWHM$	2.44	3.83	4.39	5.64
Summer11 MC, m=120, VTX matched				
$\Delta(m), [GeV]$ reco-true	-0.71 ± 0.02	0.55 ± 0.03	-0.58 ± 0.06	0.56 ± 0.07
$\sigma(CB), [GeV]$	0.92 ± 0.02	1.37 ± 0.04	1.63 ± 0.06	2.01 ± 0.05
$\sigma(CB), \%$	0.81	1.27	1.44	1.57
$\sigma(GAUSS)$	2.79 ± 0.10	3.31 ± 0.10	3.55 ± 0.25	5.29 ± 0.41
$Gauss\%$	21.1	33.4	24.0	20.0 (fixed)
$FWHM$	2.22	3.47	4.01	4.86
Summer11 MC, m=120 pile-up reweighted				
$\Delta(m), [GeV]$ reco-true	-0.70 ± 0.01	0.52 ± 0.02	-0.57 ± 0.06	0.45 ± 0.06
$\sigma(CB), [GeV]$	0.95 ± 0.02	1.42 ± 0.04	1.66 ± 0.08	2.25 ± 0.05
$\sigma(GAUSS)$	3.05 ± 0.09	3.49 ± 0.08	3.62 ± 0.16	5.93 ± 0.22
$Gauss\%$	27.4	39.1	38.1	20.0 (fixed)
$FWHM$	2.39	3.75	4.36	5.31
$Z \to ee$				
Summer11 MC				
$\Delta(m), [GeV]$ reco-true	0.01 ± 0.02	0.51 ± 0.02	1.61 ± 0.05	0.59 ± 0.04
$\sigma(CB), [GeV]$	1.00 ± 0.04	1.86 ± 0.02	1.74 ± 0.05	2.69 ± 0.04
$\sigma(CB), \%$	1.10	2.03	1.91	2.95
2011 DATA May10				
$\Delta(m), [GeV]$ reco-true	0.43 ± 0.06	0.34 ± 0.05	0.76 ± 0.16	0.40 ± 0.01
$\sigma(CB), [GeV]$	1.33 ± 0.08	2.23 ± 0.05	2.91 ± 0.18	3.42 ± 0.09
$\sigma(CB), \%$	1.46	2.45	3.19	3.75

Table B.1: Fit results for mass resolution from $H \to \gamma\gamma$ MC decays in four categories. The numbers for Spring11 (Fig B.1 and B.2), Summer11 (Fig B.3 and B.4), Summer11 with VTX match (Fig B.5 and B.6 and Summer11 with pile-up reweighting (Fig B.7 and B.8) are compared. The results from the fits to $Z \to ee$ are given for comparison as well.

B.1.4 Further systematic studies of the mass resolution extracted from $H \rightarrow \gamma\gamma$ signal MC.

B.1.4.1 Relation between non-showering electrons and unconverted photons.

We also studied the resolution using the electron categorization variable, $brem = \frac{\sigma_\phi}{\sigma_\eta}$, to allow translation of results from $Z \rightarrow ee$. The variable $brem$ is used as an estimator for the amount of energy lost by electrons via bremsstrahlung [58]. A correction is applied to the SuperCluster energy, parametrized as a function of $brem$. This correction was derived from a single electron MC gun sample and applied to all electrons as well as to photons with $R9 < 0.94$ in EB and $R9 < 0.95$ in EE. The variable $brem$ is correlated with the variable $R9$.

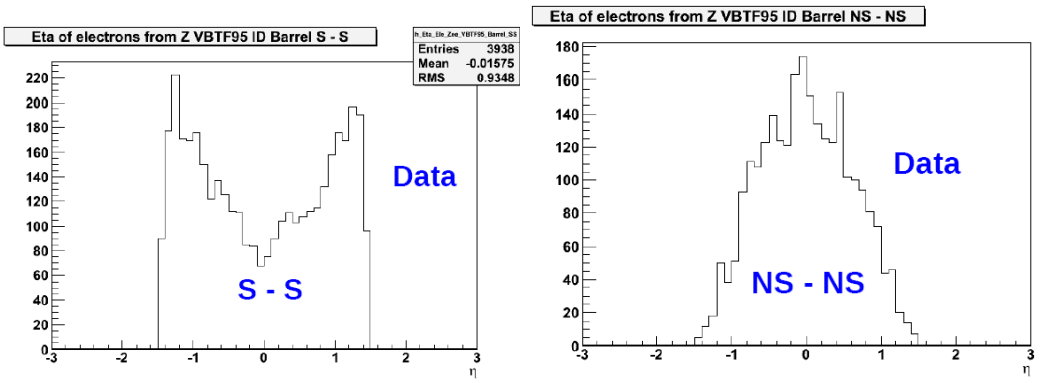

Figure B.9: Distribution of the supercluster η of showering (left) and nonshowering (right) electrons.

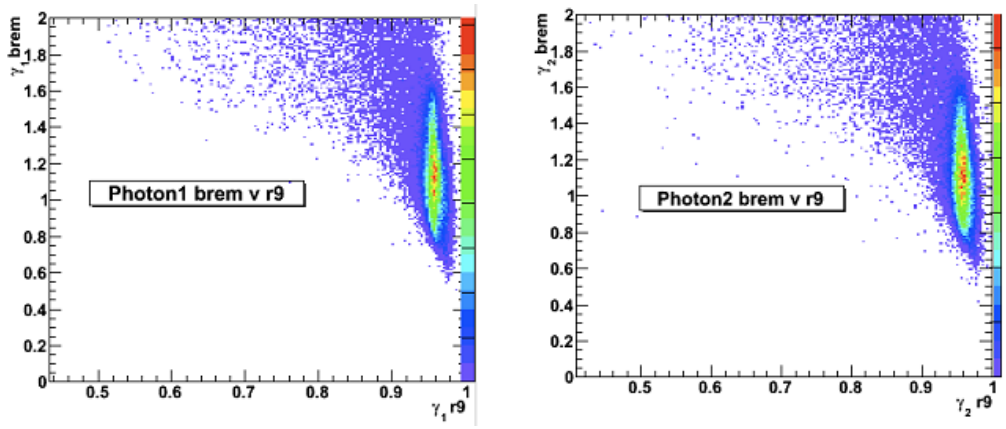

Figure B.10: Correlation between *brem* and R9.

B.1.4.2 Summer11 MC, brem categories.

Having established the connection between brem and r9, we can refit in categories of brem.

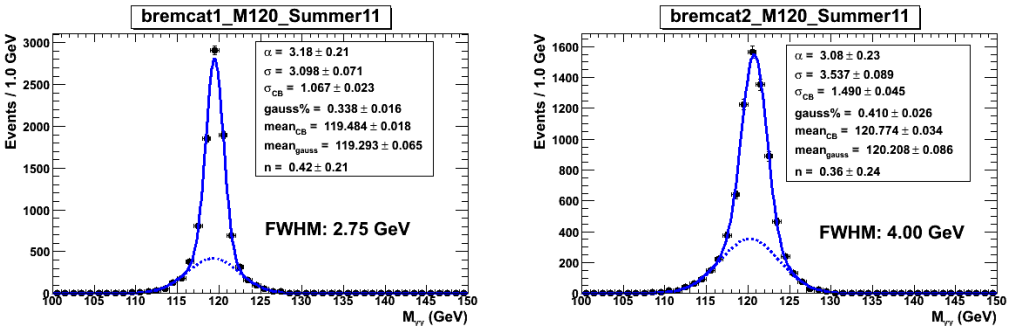

Figure B.11: Events selected by a cut at f(brem) > 2.0 (left) or < 2.0 (right) for the $H \to \gamma\gamma$ Summer11 MC production.

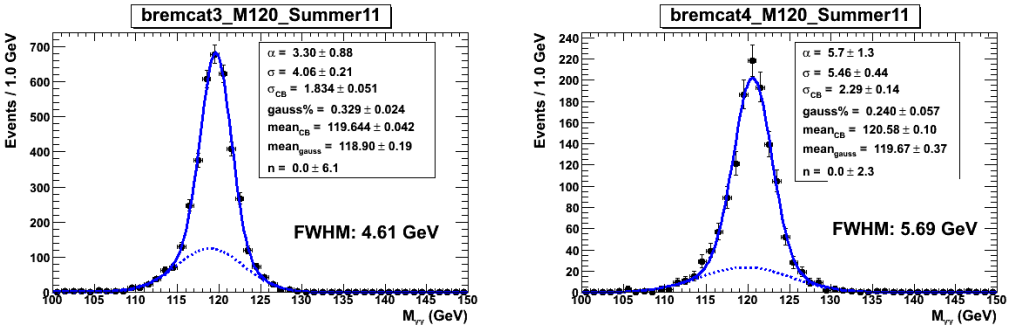

Figure B.12: Events selected by a cut at f(brem) > 2.0 (left) or < 2.0 (right) for the $H \to \gamma\gamma$ Summer11 MC production.

B.1.4.3 Summer11 MC, brem categories, vertex matched.

In the same way as for r9 categories, we can also add a vertex matching requirement

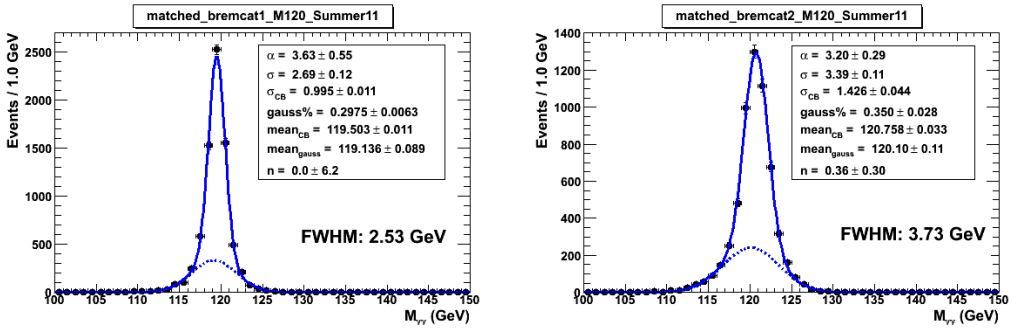

Figure B.13: Events selected by a cut at f(brem)>2.0 (left) or <2.0 (right) for the $H \to \gamma\gamma$ Summer11 MC production. The reconstructed vertex was required to match the true vertex.

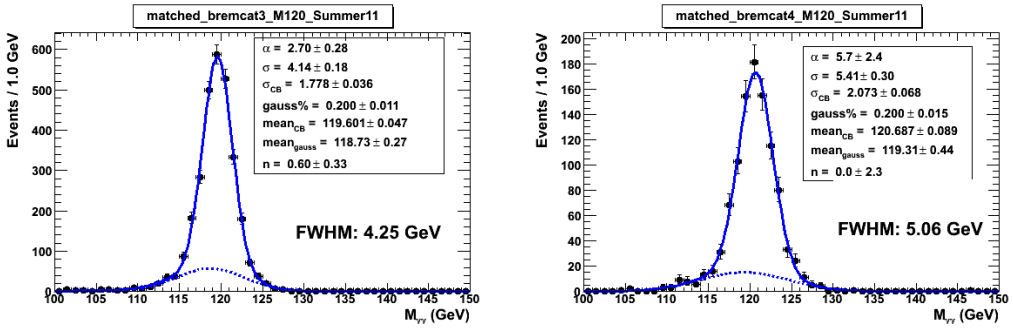

Figure B.14: Events selected by a cut at f(brem)>2.0 (left) or <2.0 (right) for the $H \to \gamma\gamma$ Summer11 MC production. The reconstructed vertex was required to match the true vertex.

	EBEB,brem<2.0	EBEB,brem>2.0	EEEE,brem<2.0	EEEE,brem>2.0
Summer11 MC, m=120,				
$\Delta(m), [GeV]$ MCreco-true	-0.52 ± 0.02	0.77 ± 0.03	-0.35 ± 0.06	-0.33 ± 0.07
$\sigma(CB), [GeV]$	1.07 ± 0.02	1.49 ± 0.04	1.83 ± 0.05	2.29 ± 0.14
$\sigma(CB), \%$	0.89	1.24	1.53	1.90
$\sigma(GAUSS)$	3.10 ± 0.07	3.54 ± 0.09	4.00 ± 0.21	5.46 ± 0.44
$Gauss\%$	33.8	41.0	32.9	24.0
$FWHM$	2.75	4.0	4.61	5.69
Summer11 MC, m=120,				
VTX matched				
$\Delta(m), [GeV]$ MCreco-true	-0.50 ± 0.02	0.76 ± 0.03	-0.40 ± 0.06	0.69 ± 0.07
$\sigma(CB), [GeV]$	1.00 ± 0.01	1.43 ± 0.04	1.78 ± 0.04	2.07 ± 0.07
$\sigma(CB), \%$	0.83	1.19	1.48	1.72
$\sigma(GAUSS)$	2.69 ± 0.12	3.36 ± 0.11	3.55 ± 0.25	5.41 ± 0.30
$Gauss\%$	29.8	35.0	20.0 (fixed ?)	20.0 (fixed)
$FWHM$	2.53	3.73	4.25	5.06
Summer11 MC, m=120				
pile-up reweighted				
$\Delta(m), [GeV]$ reco-true	-0.70 ± 0.01	0.52 ± 0.02	-0.57 ± 0.06	0.45 ± 0.06
$\sigma(CB), [GeV]$	0.95 ± 0.02	1.42 ± 0.04	1.66 ± 0.08	2.25 ± 0.05
$\sigma(GAUSS)$	3.05 ± 0.09	3.49 ± 0.08	3.62 ± 0.16	5.93 ± 0.22
$Gauss\%$	27.4	39.1	38.1	20.0 (fixed)
$FWHM$	2.39	3.75	4.36	5.31

Table B.2: Fit results for the mass resolution from $H \to \gamma\gamma$ MC decays in four categories, using *brem* to categorize converted and unconverted photons. The numbers from the pile-up reweighted sample from table are given for comparison.

B.1.4.4 Summer11 MC, Higgs pT bins

We also split the signal in 3 bins of pT, and we can see that the higher pT bins have a narrower peak, though this effect is dispersed into the two fitted widths and also a drop in the relative fraction of the gaussian (tail) component.

	pT < 20GeV	20 < pT < 40	pT > 40GeV
Summer11 MC, m=120, cat1			
$\Delta(m), [GeV]$ MCreco-true	-0.70 ± 0.03	-0.68 ± 0.03	-0.70 ± 0.03
$\sigma(CB), [GeV]$	1.02 ± 0.04	0.95 ± 0.04	0.90 ± 0.03
$\sigma(GAUSS)$	3.32 ± 0.13	3.00 ± 0.16	2.75 ± 0.12
$Gauss\%$	30.6	28.7	23.3
$FWHM$	2.58	2.39	2.23
Summer11 MC, m=120, cat2			
$\Delta(m), [GeV]$ MCreco-true	+0.58 ± 0.05	0.54 ± 0.05	0.43 ± 0.05
$\sigma(CB), [GeV]$	1.47 ± 0.07	1.41 ± 0.07	1.31 ± 0.06
$\sigma(GAUSS)$	3.55 ± 0.14	3.54 ± 0.14	3.01 ± 0.14
$Gauss\%$	45.8	39.4	36.2
$FWHM$	4.05	3.72	3.42
Summer11 MC, m=120, cat3			
$\Delta(m), [GeV]$ MCreco-true	-0.65 ± 0.13	-0.45 ± 0.10	0.66 ± 0.07
$\sigma(CB), [GeV]$	1.59 ± 0.16	1.54 ± 0.13	1.78 ± 0.06
$\sigma(GAUSS)$	3.58 ± 0.17	3.40 ± 0.29	4.41 ± 0.46
$Gauss\%$	55.5	36.4	12.4
$FWHM$	4.79	3.99	4.23
Summer11 MC, m=120, cat4			
$\Delta(m), [GeV]$ MCreco-true	0.52 ± 0.16	0.44 ± 0.11	0.42 ± 0.09
$\sigma(CB), [GeV]$	2.36 ± 0.23	2.22 ± 0.11	2.10 ± 0.09
$\sigma(GAUSS)$	5.02 ± 0.47	6.47 ± 0.71	7.00 ± 0.65
$Gauss\%$	31.0	14.0	10.4
$FWHM$	5.99	5.29	4.87

Table B.3: Fit results for mass resolution from $H \to \gamma\gamma$ MC decays in four categories. The samples have been split into three p_T bins. The simulated Higgs mass is 120 GeV.

B.1.4.5 Dependency on Number of Vertices

Another way to estimate the impact of pile-up on the signal shape is to measure the dependency of the fit parameters on the number of vertices in the event. The dependency of the resolution on the number of vertices is very mild, and largely overshadowed by the dependency on the gaussian fraction in any given fit.

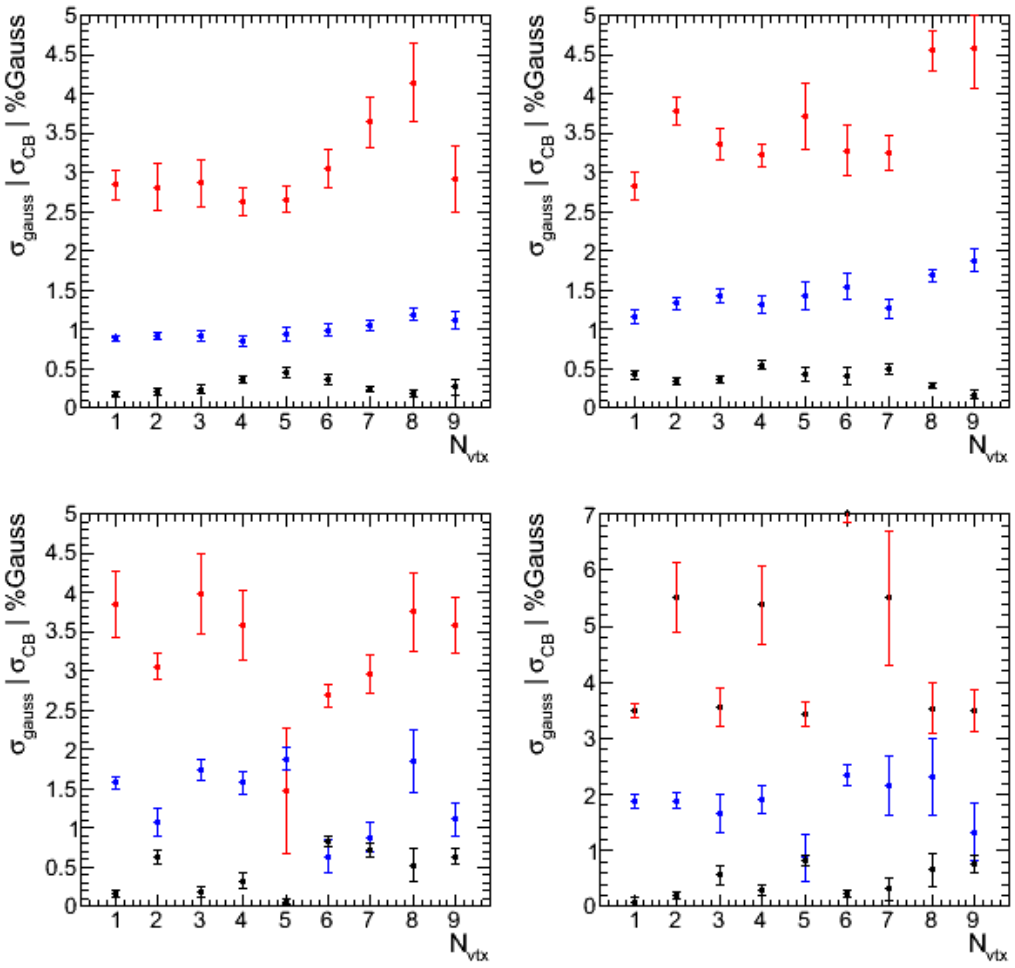

Figure B.15: Dependency of σ_{Gauss} (blue), σ_{CB} (red), and %gauss on the number of vertices

B.2 Extrapolating the mass resolution from $Z \to ee$ to $H \to \gamma\gamma$ signal MC.

B.2.1 Shape differences between the crystal ball portion of the fit in $H \to \gamma\gamma$ and $Z \to ee$.

To investigate the differences in the line shape of the $H \to \gamma\gamma$ signal compared to the $Z \to ee$ signal in detail we fit a $H \to \gamma\gamma$ signal sample with a mass near M_Z of 90 GeV. The aim is to cross check potential small differences which could bias the result when the additional resolution smearing is extracted from the Z but applied to a Higgs signal at higher mass.

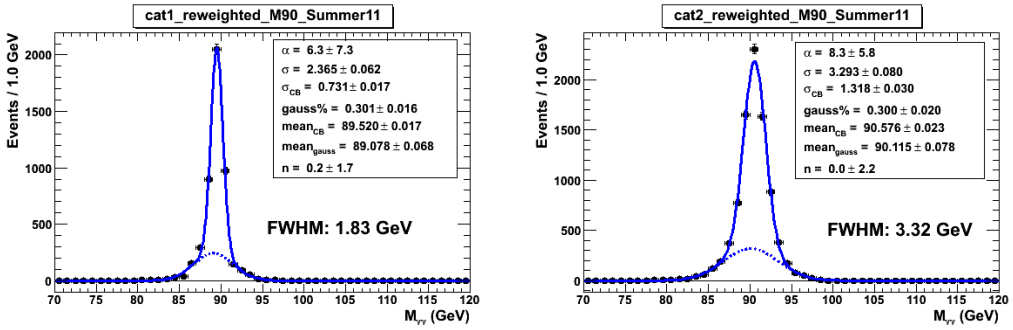

Figure B.16: Fit of the $H \to \gamma\gamma$ signal shape in categories 1 and 2 for a simulated mass of 90 GeV.

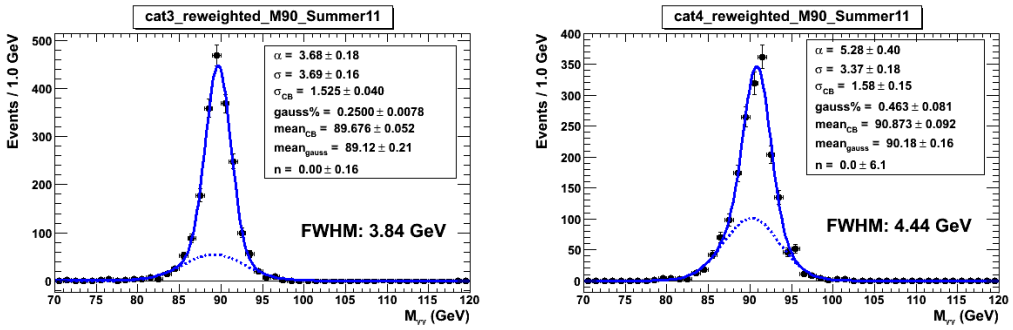

Figure B.17: Fit of the $H \to \gamma\gamma$ signal shape in categories 3 and 4 for a simulated mass of 90 GeV.

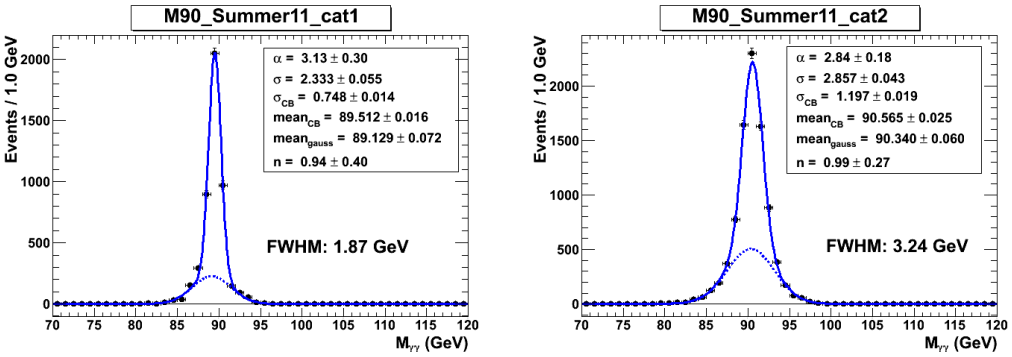

Figure B.18: Fit of the $H \to \gamma\gamma$ signal shape in categories 1 and 2 for a simulated mass of 90 GeV. Here, the fraction of gauss portion of the fit to the signal has been fixed to the values obtained from the 120 GeV signal sample.

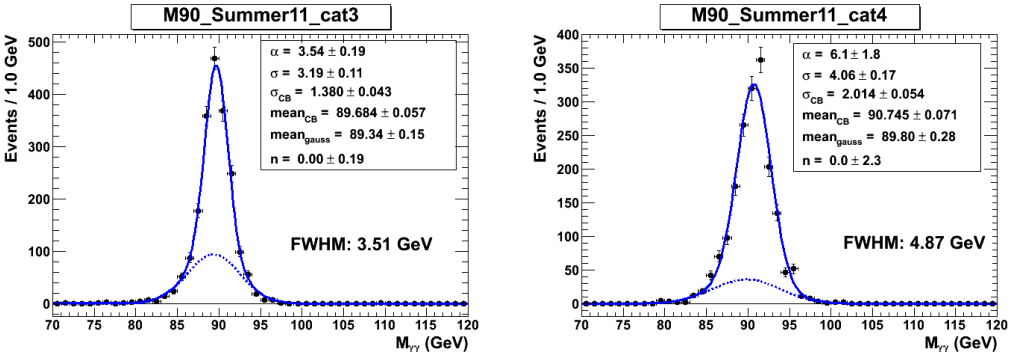

Figure B.19: Fit of the $H \to \gamma\gamma$ signal shape in categories 3 and 4 for a simulated mass of 90 GeV. Here, the fraction of gauss portion of the fit to the signal has been fixed to the values obtained from the 120 GeV signal sample.

	EBEB, R9>0.94	EBEB, R9<0.94	EEEE, R9>0.94	EEEE, R9<0.94
Summer11 MC, m=90				
$\Delta(m), [GeV]$ reco-true	-0.48 ± 0.01	0.58 ± 0.02	-0.32 ± 0.05	0.87 ± 0.09
$\sigma(CB), [GeV]$	0.73 ± 0.02	1.32 ± 0.04	1.53 ± 0.04	1.58 ± 0.15
$\sigma(CB), \%$	0.81 ± 0.02	1.46 ± 0.04	1.70 ± 0.04	1.75 ± 0.15
$\sigma(GAUSS)$	2.37 ± 0.06	3.29 ± 0.08	3.69 ± 0.16	3.37 ± 0.18
$Gauss\%$	30.1	30.0	25.0	46.3
$FWHM$	1.83	3.32	3.86	4.44
$Z \to ee$				
Summer11 MC, m=90, gauss% fixed				
$\Delta(m), [GeV]$ reco-true	0.01 ± 0.02	0.51 ± 0.02	1.61 ± 0.05	0.59 ± 0.04
$\sigma(CB), [GeV]$	1.00 ± 0.04	1.86 ± 0.02	1.74 ± 0.05	2.69 ± 0.04
$\sigma(CB), \%$	1.10 ± 0.04	2.03 ± 0.02	1.91 ± 0.05	2.99 ± 0.04
Summer11 MC, m=120				
pile-up reweighted				
$\Delta(m), [GeV]$ reco-true	-0.70 ± 0.01	0.52 ± 0.02	-0.57 ± 0.06	0.45 ± 0.06
$\sigma(CB), [GeV]$	0.95 ± 0.02	1.42 ± 0.04	1.66 ± 0.08	2.25 ± 0.05
$\sigma(CB), \%$	0.79 ± 0.02	1.18 ± 0.03	1.38 ± 0.07	1.88 ± 0.04
$\sigma(GAUSS)$	3.05 ± 0.09	3.49 ± 0.08	3.62 ± 0.16	5.93 ± 0.22
$Gauss\%$	27.4	39.1	38.1	20.0 (fixed)
$FWHM$	2.39	3.75	4.36	5.31

Table B.4: Fit results for the mass resolution from $H \to \gamma\gamma$ MC at $M = 90GeV$ in four categories, floating gauss fraction and fixing to 120GeV fit values. The numbers from the pile-up reweighted sample and the $Z \to ee$ numbers from Table B.1 are given for comparison.

B.2.2 Energy dependence of the $H \to \gamma\gamma$ mass resolution in MC.

In order to extrapolate the performance measured with $Z \to ee$ to $H \to \gamma\gamma$ we study the mass dependence of the mass resolution. The mass resolution is energy dependent as described in B.2. If the energy resolution is the dominating contribution to the mass resolution we expect to see a mass dependent mass resolution.

	90 GeV	110 GeV	115 GeV	120 GeV	130 GeV	140 GeV
$\sigma(CB), [GeV]$	0.73 ± 0.02	0.89 ± 0.01	0.91 ± 0.02	0.98 ± 0.02	1.04 ± 0.01	1.12 ± 0.02
$\sigma(CB), \%$	0.79 ± 0.02	0.80 ± 0.01	0.79 ± 0.02	0.81 ± 0.02	0.80 ± 0.01	0.80 ± 0.02

Table B.5: Fit results for mass resolution from $H \to \gamma\gamma$ MC as a function of the Higgs mass. The mass resolution seems not to depend on the mass in the mass range from 90 GeV to 140 GeV. The 90 GeV sample is with the Summer11 MC, all other samples are from Spring11 MC.

B.2.3 Conclusions and summary of the $H \rightarrow \gamma\gamma$ signal fits.

From the above plots we can conclude several things: We observe a shift in the energy scale between the R9 categories with the high R9 category being systematically lower. With the parametrisation using a gauss and a crystal ball, pile-up seems to impact mostly the underlying gauss distribution, while the crystal ball part is minimally affected. Vertex matching reduces this significantly. The relative scaling of the energy resolution among the categories does not match well between electrons and photons. The energy resolution in category 1 does not depend on the higgs mass.

B.3 Smearing the mass resolution of the $H \to \gamma\gamma$ signal MC.

To adjust possible differences between the measured resolution in data and MC one may have to inject additional smearing into the MC. Here we explore how reliably injecting additional smearing to the mass resolution can model the resolution found in data, by comparing the fitted width with injected smearing vs. the expected width from addition in quadrature. The measured smearing is found to be biased slightly higher than the input gaussian. Additonal bias effects are studied in Appendix C.2

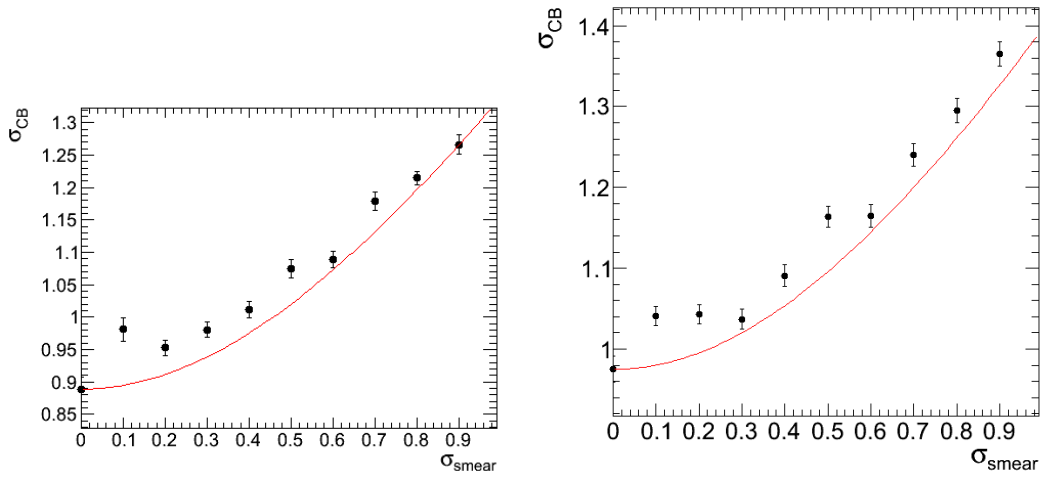

Figure B.20: Width of the signal peak for 110 GeV (left) and 120 GeV (right) $H \to \gamma\gamma$ MC sample extracted with the fit, plotted vs. the injected smearing of the invariant mass.

Appendix C

ECAL Resolution with $Z \to e^+e^-$

C.1 EM resolution from Zee

The measurement of the photon energy resolution in the kinematic range of Higgs decays is complicated by the lack of a reference process, such as $Z \to e^+e^-$for similar measurements for electrons. The similarity of electron and photon deposits, including identical clustering algorithms, suggests that one method is to bootstrap the photon performance, from photons to electrons, and then from individual electrons to the mass resolution of $Z \to e^+e^-$, which is convolved with the intrisinc Z width. We assume that the Z resonance is a convolution of a Breigt-Wigner (theory/intrinsic width) convolved with a Crystal-Ball function.

(C.1)

This leaves several areas in which biases can exist and need to be examined:

- The determination of individual particle resolution from mass resolution
- The determination of the resolution from the functional form of the resonance
- The relation between electron and photon clusters and their resolutions
- The stability of resolutions from M_Z to M_H

These issues are investigated in the following sections.

C.2 Bias and Smearing studies

C.2.1 Comparing fixed alpha to simultaneous

For the September runs, compare the performance in the mixed category using fixed alpha (to MC) fitting (Figure C.1), vs. simult fitting (Figure C.2) with shared alpha:

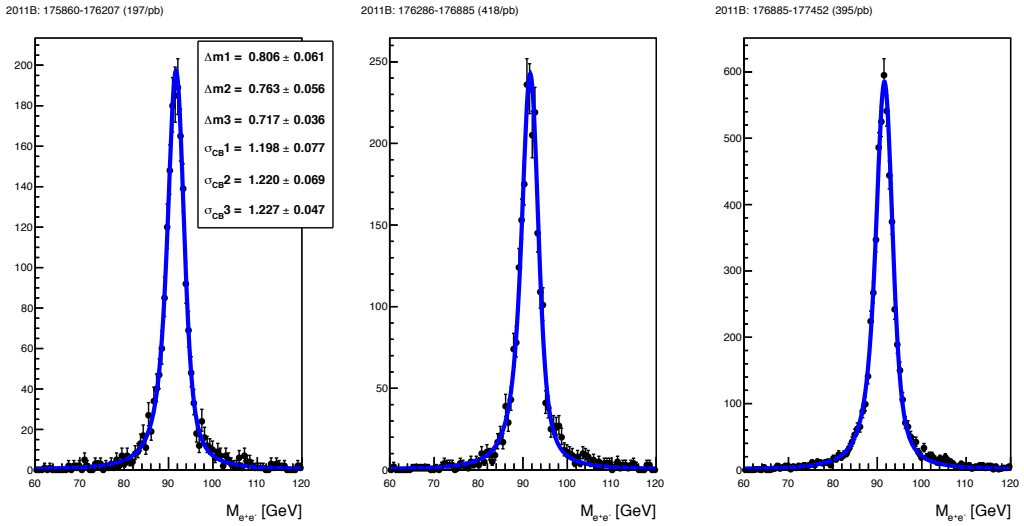

Figure C.1: alpha = 1.45, n = 3.01 (MC)

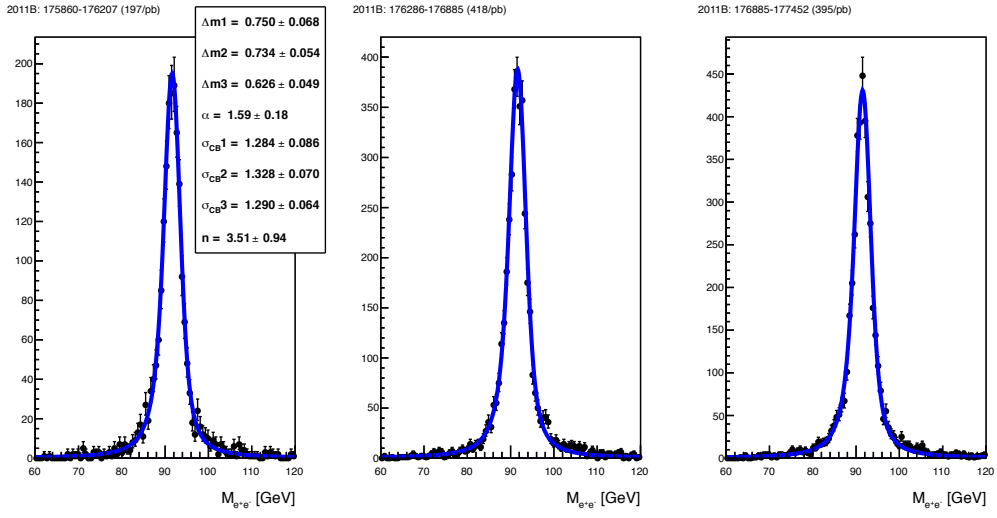

Figure C.2: alpha and n floated, but shared

	Period 1	Period 2	Period 3
Fixed	1.20(8)	1.22(7)	1.23(5)
Simult	1.28(9)	1.32(7)	1.29(6)

Fixing to MC leads to lower σ_{CB} in this case. The simult fitting preferred alpha = 1.6, n = 3.5. The data set tags were not optimal, thus the numbers are for qualitative reference only.

C.2.2 Bias/turn on plateau in alpha

As discussed earlier, there is strong bias for σ_{CB} as a function of alpha. Below some threshold, $\alpha < \alpha_0$, σ_{CB} depends on α and n. Above a certain threshold, $\alpha \sim 1.5$, the dependence weakens into a plateau. Next we find the turn on and plateau for such curves, and see if they are universal.

The bias curves are not universal, neither between data/MC nor multiple data periods. Therefore, care must be taken to maintain compatible shape parameters between datasets when extracting resolutions.

C.2.3 Interpretation to energy resolution

The original design, is that σ_{CB} is analytically related to the energy resolution for a given class of objects/events. Since we know that there is additional dependence on the shape parameter α, we try to quantify the effect of different α values by:

- checking for bias from fit parameters (toy MC only), in the turn on and plateau regions.
- testing a sum in quadrature relation using MC with added smearing to each electron (Closure).

The value of σ_{CB} depends strongly for alpha from 1.0-2.0. The plateau region doesn't correspond to true sigma, unless the alpha was already above this region. To cover this effect, 2D lookup maps are in Appendix C.3.

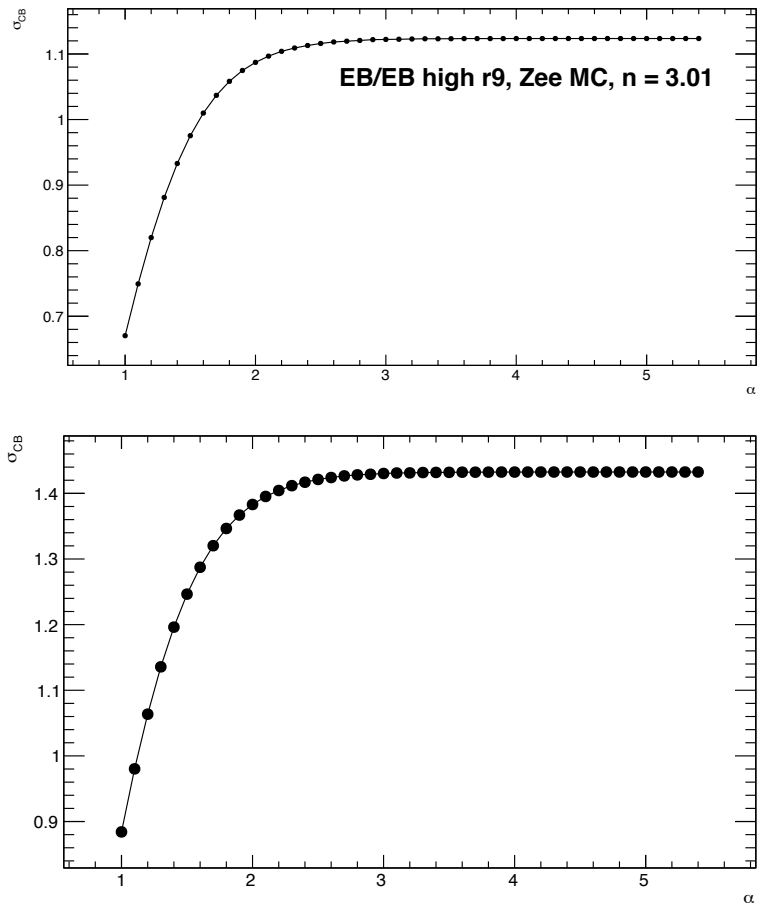

Figure C.3: fitting with various alpha values in MC (Top) and DATA (Bottom)

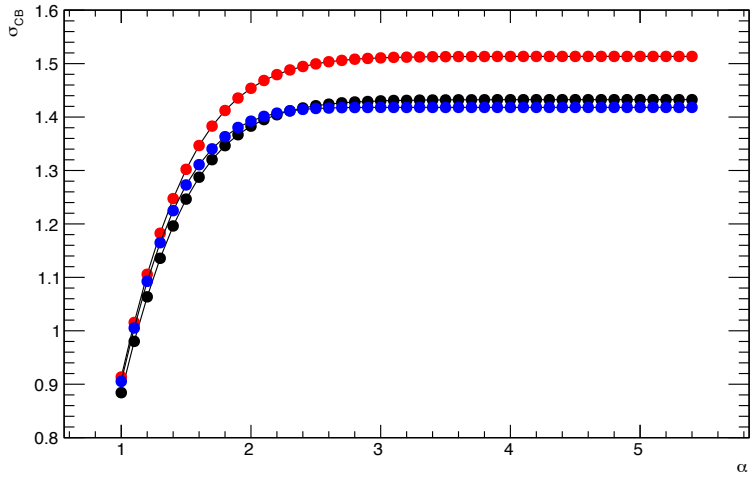

Figure C.4: fitting with various alpha values in 3 periods of september data

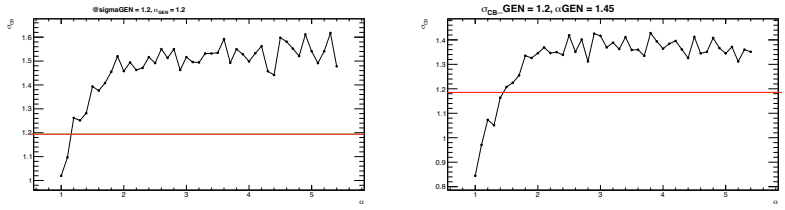

Figure C.5: for small true alpha (< 1.5), σ_{CB} depends on alpha, and doesn't plateau at true value

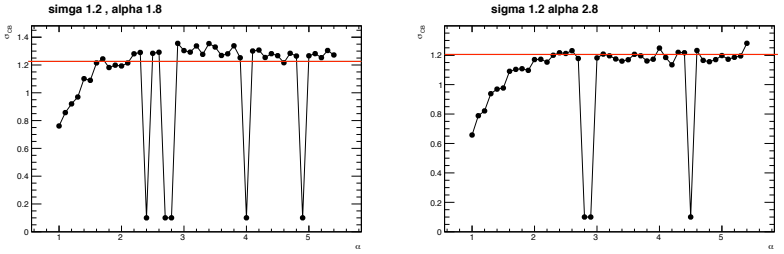

Figure C.6: for large true alpha, plateau at true value. Low points are from failed Toy MC fits.

For the smearing and fitting, we start with Summer11 MC, then smear electron energies with gaussian distribution (0, 0.5, 1, etc). The closure test is to try to deduce the smearing with the results from the fit method.

Fixing α to MC, gives linear scaling, but at only 90% of the input smearing (Figure C.7. Floating α gives a scaling much closer to $\sqrt{2}$ factor(Figure C.8. So that it is clear that the relative smearing at different levels is a reliable measure of the resolution, though there may be an overall bias which depends on the fixing of the α parameter.

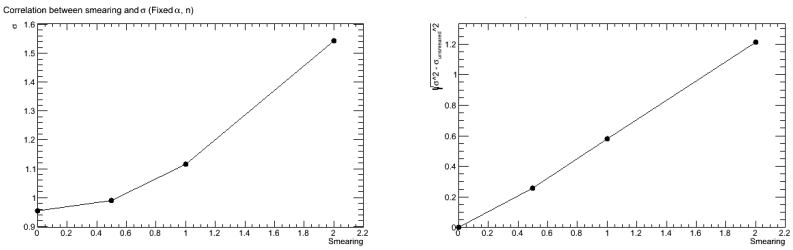

Figure C.7: fix alpha to MC, test quadrature relation of sigma to smearing

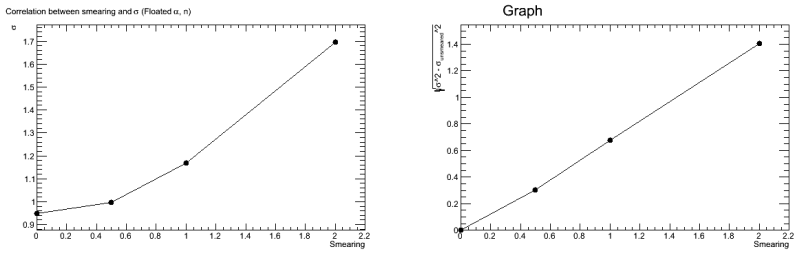

Figure C.8: floating parameters, test quadrature relation of sigma to smearing

C.3 Alpha Systematics

Fitting the wrong alpha leads to a systematic bias in measured σ. The Following are maps of σ_{FIT} in the plane of σ_{GEN} and α_{FIT} for values of α_{GEN} from 1.0 to 2.0. The values can be used as a lookup table to convert widths measured with one set of shape parameters to another.

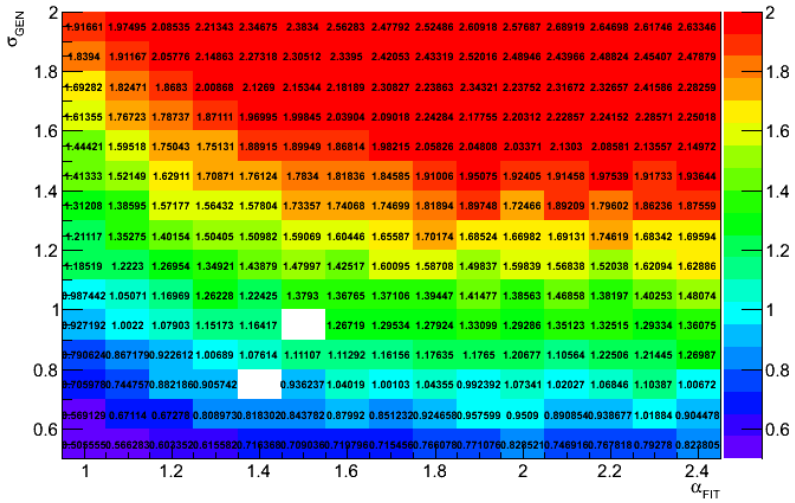

Figure C.9: Bias plot for $\alpha = 1.0$

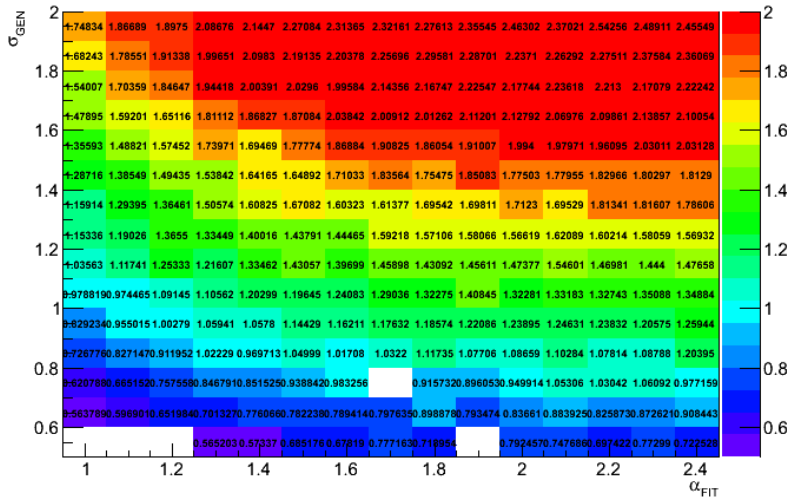

Figure C.10: Bias plot for $\alpha = 1.1$

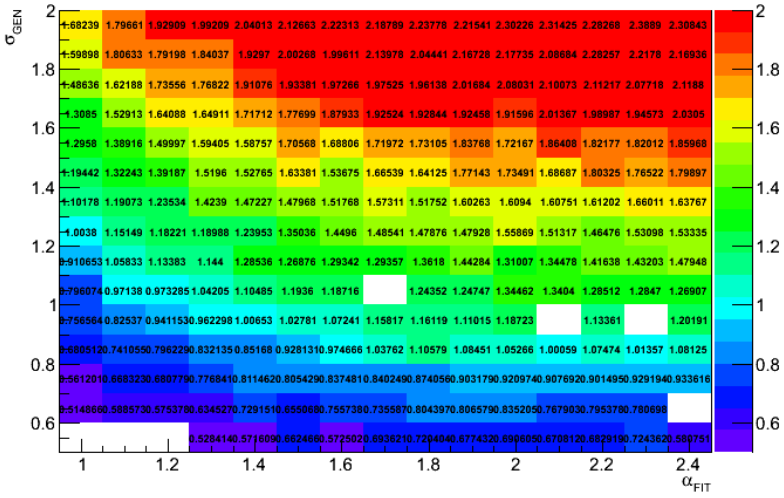

Figure C.11: Bias plot for $\alpha = 1.2$

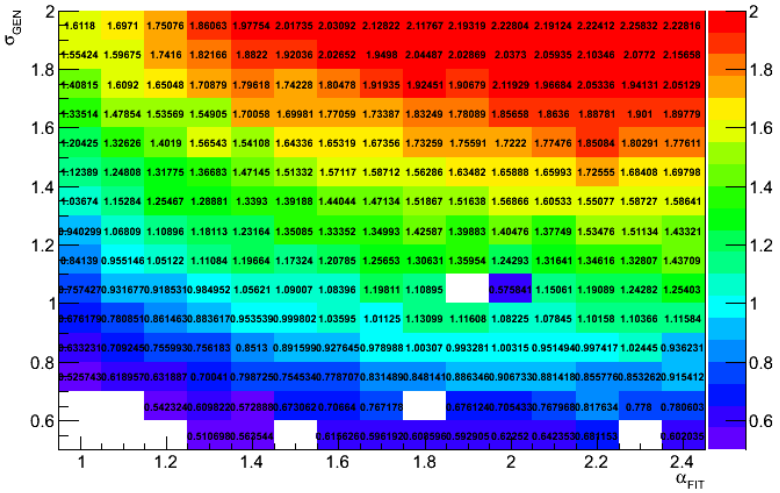

Figure C.12: Bias plot for $\alpha = 1.3$

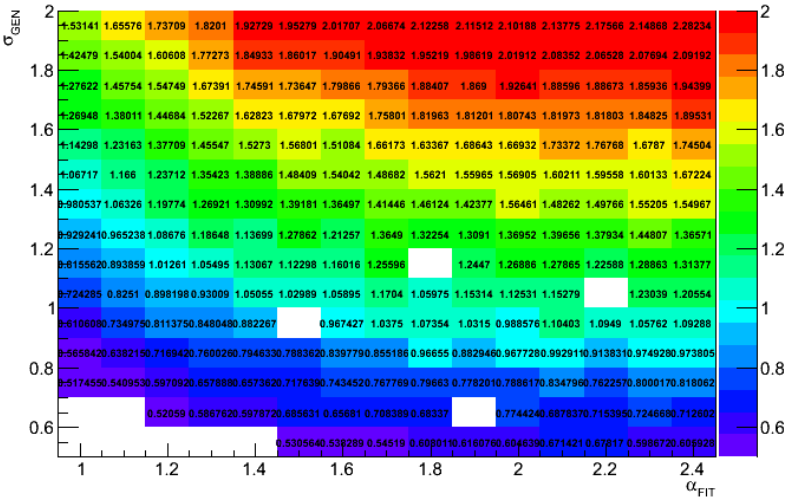

Figure C.13: Bias plot for $\alpha = 1.4$

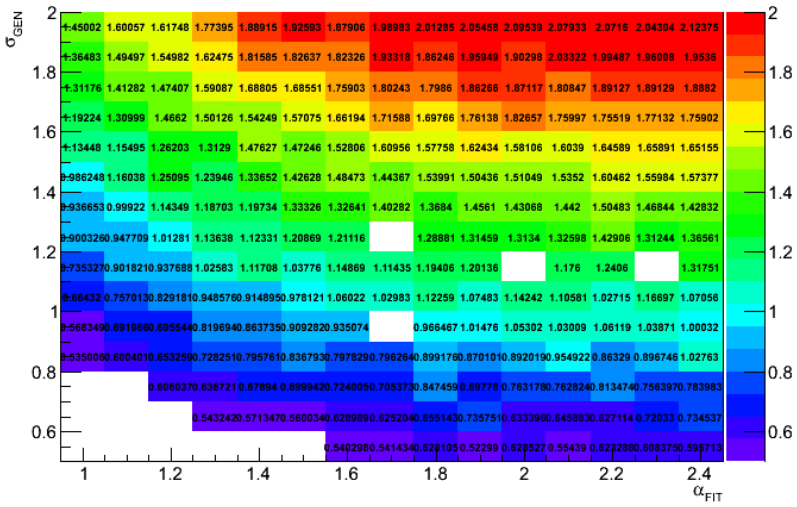

Figure C.14: Bias plot for $\alpha = 1.5$

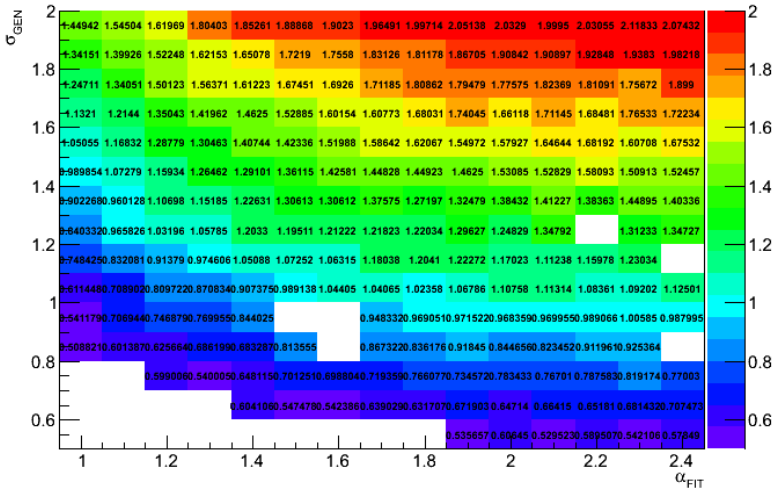

Figure C.15: Bias plot for $\alpha = 1.6$

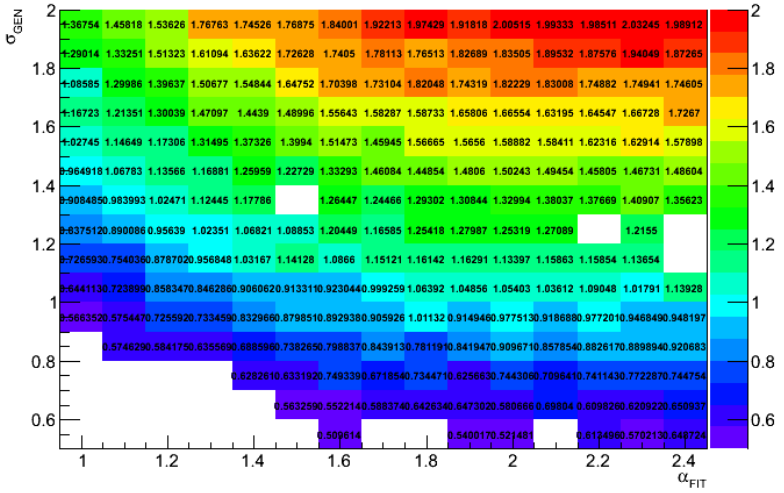

Figure C.16: Bias plot for $\alpha = 1.7$

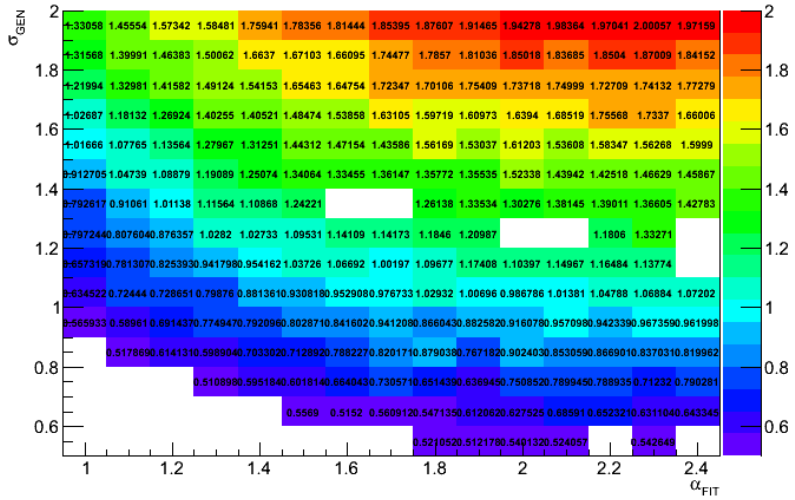

Figure C.17: Bias plot for $\alpha = 1.8$

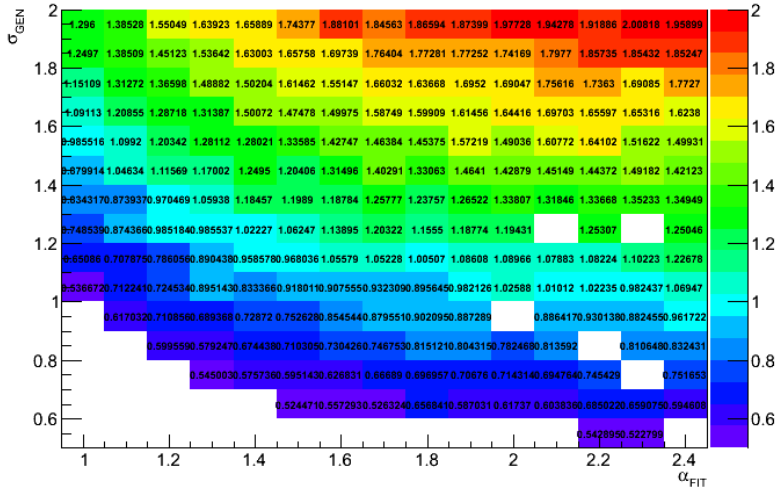

Figure C.18: Bias plot for $\alpha = 1.9$

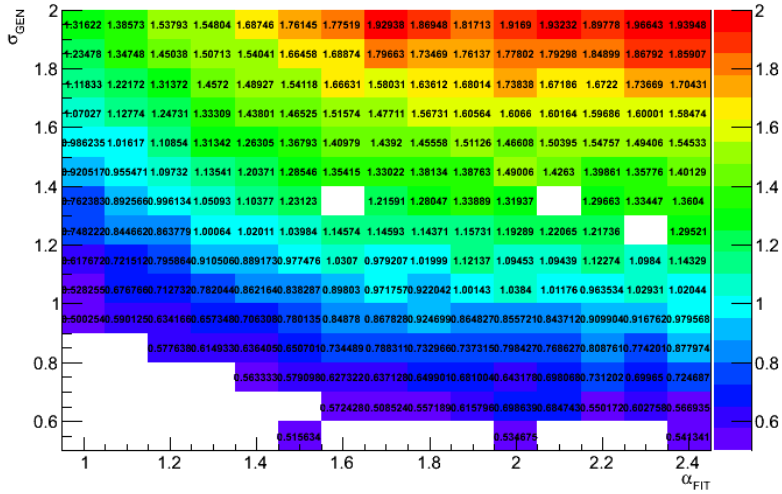

Figure C.19: Bias plot for $\alpha = 2.0$

C.4 Toy studies for non-CB tails

It may be the case that the resolutions are not well described by CB, or CBxBW convolution. One such sign is the presence of longer tails in the distributions, perhaps due to a second component. We can model this effect by generating toys, assuming an underlying pdf that is two gaussians, one wide and one narrow.

Here, both have means = 0, with $\sigma_{WIDE} = 0.8$ and $\sigma_{NARROW} = 0.4$, 80% is assigned to the narrow peak. This model is then put through the fit to CB, and toys are repeated 1000 times. The results on the bias of the 4 parameters is in Figure C.20.

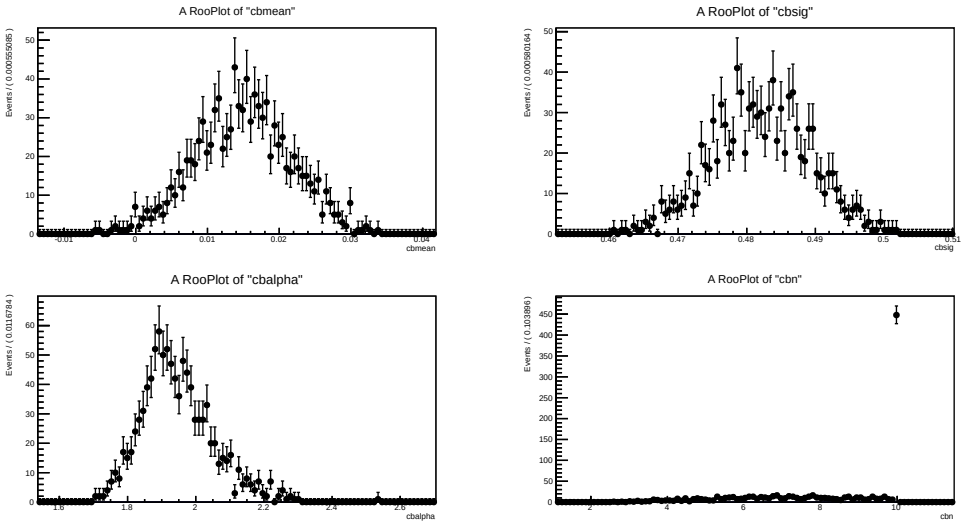

Figure C.20: Clockwise from upper left, mean, σ, α, and n for CB fits of 1000 toys

The n values vary over the entire allowed range, and thus have little effect. α is also safely > 1.5 in almost all toys. The σ is definitely biased above the 0.4 of the narrow peak, and so the small wide component can definitely have an effect.

Bibliography

[1] K. Nakamura et al. The review of particle physics. *J. Phys. G*, 37:075021, 2010.

[2] P. W. Higgs. Broken Symmetries and the Masses of Gauge Bosons. *Physical Review Letters*, 13:508–509, October 1964.

[3] S.L. Glashow. Partial Symmetries of Weak Interactions. *Nucl.Phys.*, 22:579–588, 1961.

[4] Steven Weinberg. A model of leptons. *Phys. Rev. Lett.*, 19:1264–1266, Nov 1967.

[5] Gerard 't Hooft. Renormalization of Massless Yang-Mills Fields. *Nucl.Phys.*, B33:173–199, 1971.

[6] D.J. Gross and Frank Wilczek. Ultraviolet Behavior of Nonabelian Gauge Theories. *Phys.Rev.Lett.*, 30:1343–1346, 1973.

[7] H. David Politzer. Reliable Perturbative Results for Strong Interactions? *Phys.Rev.Lett.*, 30:1346–1349, 1973.

[8] R.K. Ellis, W.J. Stirling, and B.R. Webber. *Qcd and Collider Physics*. Cambridge Monographs on Particle Physics, Nuclear Physics, and Cosmology. Cambridge University Press, 2003.

[9] Stephen P. Martin. A Supersymmetry primer. 1997.

[10] N. Arkani-Hamed, S. Dimopoulos, and G. Dvali. The hierarchy problem and new dimensions at a millimeter. *Phys. Lett. B*, 429:263, 1998.

[11] N. Arkani-Hamed, S. Dimopoulos, and G. Dvali. Phenomenology, astrophysics and cosmology of theories with submillimeter dimensions and tev scale quantum gravity. *Phys. Rev. D*, 59:086004, 1999.

[12] Lisa Randall and Raman Sundrum. A large mass hierarchy from a small extra dimension. *Phys. Rev. Lett.*, 83:3370, 1999.

[13] Walter D. Goldberger and Mark B. Wise. Modulus stabilization with bulk fields. *Phys. Rev. Lett.*, 83:4922–4925, Dec 1999.

[14] H. Davoudiasl, J. L. Hewett, and T. G. Rizzo. Experimental probes of localized gravity: On and off the wall. *Phys. Rev. D*, 63:075004, Mar 2001.

[15] T. Kaluza. On The Problem Of Unity In Physics. *Sitzungsber. Preuss. Akad. Wiss. Berlin (Math. Phys.)*, pages 966–972, 1921.

[16] O. Klein. Quantentheorie und fünfdimensionale Relativitätstheorie. *Zeitschrift fur Physik*, 37:895–906, December 1926.

[17] H. Davoudiasl, J. L. Hewett, and T. G. Rizzo. Phenomenology of the randall-sundrum gauge hierarchy model. *Phys. Rev. Lett.*, 84:2080–2083, Mar 2000.

[18] (ed.) Evans, Lyndon and (ed.) Bryant, Philip. LHC Machine. *JINST*, 3:S08001, 2008.

[19] G.L. Bayatian et al. CMS technical design report, volume II: Physics performance. *J.Phys.G*, G34:995–1579, 2007.

[20] S. Chatrchyan et al. The CMS experiment at the CERN LHC. *JINST*, 3:S08004, 2008.

[21] CMS Collaboration. Absolute calibration of the luminosity measurement at cms: Winter 2012 update. 2012.

[22] CMS ECAL Group. Studies of the CMS Electromagnetic Calorimeter performance in the electron test beam. *J. Phys. Conf. Ser.*, 160:012048, 2010.

[23] CMS Collaboration. Isolated photon reconstruction and identification at $\sqrt{s} = 7$ TeV. CMS Physics Analysis Summary CMS-PAS-EGM-10-006, 2010.

[24] Ren yuan Zhu. Radiation damage in scintillating crystals. 1998.

[25] ROBERT B. GORDON. Color centers in crystals. *American Scientist*, 47(3):pp. 361–375, 1959.

[26] T. Aaltonen et al. Search for high-mass diphoton states and limits on randall-sundrum gravitons at cdf. *Phys. Rev. Lett.*, 99:171801, 2007.

[27] T. Aaltonen et al. Search for New Dielectron Resonances and Randall-Sundrum Gravitons at the Collider Detector at Fermilab. *Phys. Rev. Lett.*, 107:051801, 2011.

[28] Victor Mukhamedovich Abazov et al. Search for Randall-Sundrum gravitons in the dielectron and diphoton final states with 5.4 fb^{-1} of data from ppbar collisions at $\sqrt{s} = 1.96$ TeV. *Phys. Rev. Lett.*, 104:241802, 2010.

[29] J. Veverka et al. Photon pixel match veto efficiency measurement with z to mumugamma events selected at 7 tev. *CMS Analysis Note*, 2011.

[30] A. Askew et al. Search for gauge mediated supersymmetry breaking using two photons and missing transverse energy. *CMS Analysis Note*, 2012.

[31] Torbjorn Sjostrand, Stephen Mrenna, and Peter Skands. PYTHIA 6.4 physics and manual. May 2006.

[32] M.C. Kumar, P. Mathews, V. Ravindran, and A. Tripathi. Diphoton signals in theories with large extra dimensions to nlo qcd at hadron colliders. *Phys. Lett. B*, 672:45, 2009.

[33] T. Binoth, J. Ph. Guillet, E. Pilon, and M. Werlen. A full next-to-leading-order study of direct photon pair production in hadronic collisions. *Eur. Phys. J. C*, 16:311, 2000.

[34] Z. Bern, L. Dixon, and C. Schmidt. Isolating a light higgs boson from the diphoton background at the lhc. *Phys. Rev. D*, 66:074018, 2002.

[35] CMS Collaboration. Measurement of the production cross section for pairs of isolated photons in pp collisions at $\sqrt{s} = 7$ TeV. Submitted to *JHEP*, 2010.

[36] T. Binoth, J. P. Guillet, E. Pilon, and M. Werlen. A Full next-to-leading order study of direct photon pair production in hadronic collisions. *Eur. Phys. J.*, C16:311–330, 2000.

[37] J. Pumplin et al. New generation of parton distributions with uncertainties from global QCD analysis. *JHEP*, 07:012, 2002.

[38] A.D. Martin, W.J. Stirling, R.S. Thorne, and G. Watt. Parton distributions for the LHC. *Eur.Phys.J.*, C63:189–285, 2009.

[39] P. Musella et al. Measurement of isolated photon production cross section in pp collisions at sqrts = 7 tev. *CMS Analysis Note*, 2010.

[40] Thomas Junk. Confidence Level Computation for Combining Searches with Small Statistics. *Nucl. Instrum. Meth.*, A434:435–443, 1999.

[41] John C. Collins and Davison E. Soper. Angular distribution of dileptons in high-energy hadron collisions. *Phys. Rev. D*, 16:2219–2225, Oct 1977.

[42] K. Nakamura et al. The review of particle physics, review of statistics. *J. Phys. G*, 37:075021, 2010.

[43] Bayes and Price. An essay towards solving a problem in the doctrine of chances. by the late rev. mr. bayes, f. r. s. communicated by mr. price, in a letter to john canton, a. m. f. r. s. *Philosophical Transactions*, 53:370–418, January 1763.

[44] G. Aad et al. Search for dilepton resonances in pp collisions at $\sqrt{s} = 7$ TeV with the ATLAS detector. 2011. Submitted to Physical Review Letters.

[45] CMS Collaboration. Search for resonances in the dilepton mass distribution in pp collisions at $\sqrt{s} = 7$ tev. (EXO-11-019-PAS), 2011.

[46] G. Giudice, R. Rattazzi, and J. Wells. Quantum gravity and extra dimensions at high-energy colliders. *Nucl. Phys. B*, 544:3, 1999.

[47] T. Han, J.D. Lykken, and R.-J. Zhang. Kaluza–klein states from large extra dimensions. *Phys. Rev. D*, 59:105006, 1999.

[48] J.L. Hewett. Indirect collider signals for extra dimensions. *Phys. Rev. Lett.*, 82:4765, 1999.

[49] T. Gleisberg et al. Sherpa 1.α, a proof-of-concept version. *JHEP*, 02:056, 2004.

[50] M.C. Kumar, P. Mathews, V. Ravindran, and A. Tripathi. Direct photon pair production at the LHC to $\mathcal{O}(\alpha_s)$ in TeV scale gravity models. *Nucl. Phys. B*, 818:28, 2009.

[51] CMS Collaboration. Measurement of CMS luminosity. CMS Physics Analysis Summary CMS-PAS-EWK-10-004, 2010.

[52] S. Chatrchyan et al. Search for Large Extra Dimensions in the Diphoton Final State at the Large Hadron Collider. *JHEP*, 5:85, 2011.

[53] Marcela Carena, Sandro Casagrande, Florian Goertz, Ulrich Haisch, and Matthias Neubert. Higgs Production in a Warped Extra Dimension. 2012.

[54] Walter D. Goldberger and Mark B. Wise. Bulk fields in the Randall-Sundrum compactification scenario. *Phys.Rev.*, D60:107505, 1999.

[55] Sanghyeon Chang, Junji Hisano, Hiroaki Nakano, Nobuchika Okada, and Masahiro Yamaguchi. Bulk standard model in the randall-sundrum background. *Phys. Rev. D*, 62:084025, Sep 2000.

[56] I. Narsky. Statpatternrecognition: A c++ package for statistical analysis of high energy physics data. 2005.

[57] The CMS Collaboration. Search for a higgs boson decaying into two photons in the cms detector. *CMS Physics Analysis Summary*, 2011.

[58] ECAL DPG. Cms ecal performance. *CMS Analysis Note*, 2010-363, 2010.